New advancements in highly sensitive time-resolved fluorescence two-photon microscopy

- theoretical approaches and bioscientific applications

Von der Gemeinsamen Naturwissenschaftlichen Fakultät

der Technischen Universität Carolo-Wilhelmina

zu Braunschweig

zur Erlangung des Grades einer

Doktorin der Naturwissenschaften

(Dr. rer. nat.)

genehmigte

D i s s e r t a t i o n

von

Raluca Aura Niesner

aus Bukarest / Rumänien

1 . Referent: Prof. Dr. Karl-Heinz Gericke

2 . Referent: Prof. Dr. Peter Jomo Walla

eingereicht am: 8. November 2004

mündliche Prüfung (Disputation) am: 10. Januar 2005

Druckjahr: 2005

Vorveröffentlichungen der Dissertation

Teilergebnisse aus dieser Arbeit wurden mit Genehmigung der Gemeinsamen Naturwissenschaftlichen Fakultät, vertreten durch den Mentor der Arbeit, Prof. Dr. Karl-Heinz Gericke, in folgenden Beiträgen vorab veröffentlicht:

Publikationen:

R. Niesner, W. Roth, K.-H. Gericke

Photophysical aspects of single-molecule detection by two-photon excitation with consideration of sequential pulsed illumination

ChemPhysChem 5: 678-687 (2004)

R. Niesner, B. Peker, P. Schlüsche, K.-H. Gericke

Non-iterative biexponential fluorescence lifetime imaging in the investigation of cellular metabolism by means of NAD(P)H autofluorescence

ChemPhysChem 5: 1141-1149 (2004)

R. Niesner, B. Peker, K.-H. Gericke, C.C. Müller-Goymann

3D-resolved pH-measurement in artificial skin constructs by means of fluorescence lifetime imaging

Proceedings of the International Meeting on Pharmaceutics, Biopharmaceutics and Pharmaceutical Technology, Nürnberg 115-116 (2004)

R. Niesner, K.-H. Gericke

Quantitative determination of the single-molecule detection regime in fluorescence fluctuation microscopy by means of photon counting histogram analysis

J. Chem. Phys. (2004) submitted

R. Niesner, B. Peker, K.-H. Gericke, C.C. Müller-Goymann

3D-resolved investigation of the pH-gradient in artificial skin constructs by means of fluorescence lifetime imaging

Eur. J. Pharm. Biopharm. (2004) in preparation

Tagungsbeiträge:

R. Niesner, W. Roth, K.-H. Gericke

Tatsächlich nur ein einziges Molekül? Eine statistische Analyse. (Poster)
DPG-Frühjahrstagung, Osnabrück (2002)

R. Niesner, W. Roth, K.-H. Gericke

Only one molecule, really? A statistical approach is the answer.(Poster)
Spring school on Single Molecules, Hofgeismar (2002)

R. Niesner, W. Roth, K.-H. Gericke

Tatsächlich nur ein einziges Molekül? Eine statistische Analyse. (Vortrag)
DPG-Frühjahrstagung, Regensburg (2002)

R. Niesner, B. Peker, K.-H. Gericke, C.C. Müller-Goymann

3D-resolved pH-measurement in artificial skin constructs by means of fluorescence lifetime imaging (Vortrag)
International Meeting on Pharmaceutics, Biopharmaceutics and Pharmaceutical Technology, Nürnberg (2004)

R. Niesner, B. Peker, K.-H. Gericke

Subzelluläre 3D-Analyse von künstlichen Hautkonstrukte durch Visualisierung von Fluoreszenzlebensdauern (Vortrag)
103. Tagung der Bunsengesellschaft für Physikalische Chemie, Dresden (2004)

Contents

List of Abbreviations

ADP	adenosine diphosphate
ASC	artificial skin constructs
ATP	adenosine triphosphate
FAD	flavin adenine dinucleotide
FCS	fluorescence correlation spectroscopy
FFM	fluorescence fluctuation microscopy
FIDA	fluorescence intensity distribution analysis
FLIM	fluorescence lifetime imaging
FMN	flavin adenine mononucleotide
FRAP	fluorescence recovery after photobleaching
FRET	fluorescence resonant energy transfer
GSD	ground state depeletion
HDF	human dermal fibroblasts
MPE	multi-photon excitation
MAFID	moment analysis of fluorescence intensity distribution
NADH	reduced nicotinamide adenine dinucleotide
NADPH	reduced nicotinamide adenine dinucleotide phosphate
NIR	near-infrared
OPE	one-photon excitation
PCH	photon counting histogram
PSF	point spread function
RHRI	resonant Hyper-Raman imaging
RIMAF	rotational correlation time imaging by anisotropic fluorescence
SNOM	scanning near-field optical microscopy
STED	stimulated emission depletion
TF	transfer function
TPE	two-photon excitation

Chapter 1

Introduction

1.1 Fluorescence microscopy in biosciences

A central methodological aim of the biosciences is to experimentally simulate, as good as possible, the real environmental conditions of biological systems in order to gain a true image of the effects and processes of interest. Thus, the bioscientific research is moving from test-tube observations towards *in vivo* investigations in intact cells and tissues. In this frame, the development of biophysical techniques, which allow an accurate and highly sensitive registration of changes in the studied system without disturbing the natural processes therein, is particularly significant.

Since the fluorescence of molecules accurately indicates even tiny modifications of the microenvironment, this phenomenon is ideal for investigations of biological systems. A relatively simple experimental set-up and the non-invasive nature of the process constitute further advantages, which favoured the development of a large variety of fluorescence techniques as versatile tools for the biosciences. Both time-independent quantities, e.g. emission wavelength and steady-state intensity, as well as time-dependent quantities, e.g. fluorescence lifetime and fluorescence anisotropy decay, belong to the properties monitored in fluorescence experiments. Since these properties are differently influenced by the environmental factors, they provide a large diversity of information about the investigated sample.[1,2] Hence, already at the beginning of the 20^{th} century, novel insight in the functionality of biological systems was obtained employing rudimentary fluorescence techniques, for instance, the molecular volume of proteins was determined by fluorescent conjugation with known dyes, the viscosity of a medium was obtained from the emission polarisation and the fluorescence of re-

duced nicotinamide adenine dinucleotide (NADH) and flavin adenine dinucleotide (FAD) was observed.[3]

In the last decades, the technological progress allowed the design of novel more efficient fluorescence techniques. In particular, by combining microscopical techniques with high-performance excitation sources, i.e. the lasers, a powerful tool for the biosciences has been developed, namely the fluorescence laser microscopy.[1,2] Due to its high spatial and spectral resolution and the facility of high temporal resolution, the fluorescence laser microscopy allows a wide spectrum of *in vitro* and *in vivo* experiments in intact cells and tissues. These experiments reach from monitoring the morphology of biological systems to elucidating complex cellular processes with a high sensitivity down to the single molecule level. To the most noteworthy applications of fluorescence laser microscopy belong contributions to the complete decoding of the DNA structure and the investigation of prone proteins responsible for diseases like the Alzheimer disease.

Moreover, the use of lasers in microscopical non-fluorescent techniques enabled the design of revolutionary tools like the optical tweezers used to hold and manipulate single cells or the optical scalpel used to slice chromosomes on the nanometer scale for the purpose of targeted transfection.[4]

1.1.1 Resolution and excitation

The fluorescence laser microscopy evolved in two major directions, the near-field microscopy, e.g. scanning near-field microscopy (SNOM), and the far- and wide-field microscopy. While in the near-field microscopy, the excitation laser beam is directed to the sample by a metal tip, in the far-field microscopy, it is focused into the sample by microscope objectives. In the near-field microscopy, the lateral resolution, i.e. the resolution in the focal plane perpendicular to the optical axis, can be as good as a tenth of the excitation wavelength. The factors, which limit the lateral resolution in this case, are the geometry of the metal tip and the fact that at high resolutions the photon flux at the top of the metal tip increases exponentially causing damages of the tip. In the far-field microscopy, the lateral resolution is at best limited by diffraction and it is worse than in the near-field microscopy. However, while in the near-field microscopy only investigations at the surface of the sample can be performed, in the far-field microscopy also the interior of thick samples, e.g. tissue or cells, can be monitored with a high axial resolution, i.e. the resolution on the optical axis.[5,6] Thus, the far-field microscopy is more adequate than the near-field microscopy for bioscientific studies in intact

systems.

Typically, in the fluorescence laser microscopy, each molecule absorbs one photon to reach the first excited singlet state, from which it fluoresces back to the ground state, i.e. one-photon excitation (OPE). Both the lateral and the axial resolution in OPE experiments are rather poor and the use of UV/visible excitation light dramatically limits the penetration depth in biological samples. In order to improve the spatial resolution, particularly the axial resolution, in OPE fluorescence experiments, a 3D spatial filter is introduced in front of the detector, i.e. confocal set-up. However, the confocal OPE microscopy is associated with a high loss of fluorescence signal, a reduced penetration depth and a slightly more complicated set-up. A more simple technique, which counteracts the disadvantages of the confocal OPE microscopy, is the multi-photon excitation (MPE) microscopy. The advantages of the MPE microscopy are a high spatial 3D resolution, a simple set-up and a large penetration depth due to the use of NIR excitation light, for which the tissue is mostly transparent. The main disadvantage in MPE experiments is represented by low multi-photon absorption cross-sections, which imply high excitation intensities and, thus, a possible photodamage of the sample. In the two-photon excitation (TPE) microscopy a compromise between the advantages and the disadvantages of the MPE is met.[5,6]

The spatial resolution in the far-field microscopy is determined by the transfer function (TF), i.e. the fluorescence intensity distribution at the detector and, thus, by the point spread function (PSF), i.e. the unitless distribution of the photon flux in the microscope. Consequently, efforts to rigorously describe complicated PSF and TF, like those generated by focusing the laser beam with high aperture objectives, serve to the accurate determination of the spatial resolution.[5] Moreover, different PSF-engineering procedures have been employed to improve both the lateral and the axial resolution in the far-field microscopy. To the most noteworthy belong the fluorescence inhibition by stimulated emission depletion (STED) of the first excited singlet state in the outer regions of the PSF, the ground state depletion (GSD) by triplet state saturation, the 4π-microscopy combined with constructive interference, the theta-4π-microscopy and the offset-beam overlap microscopy. By combining these procedures, lateral resolutions as good as 100 nm and axial resolutions down to 70 nm were attained.[6] However, it should be mentioned that under realistic conditions an *in vivo* experiment based on PSF engineering seems to be questionable.

1.1.2 Non-labelling versus labelling experiments

As already mentioned, since the accurate simulation of the real environmental conditions is aimed in the investigations of biological systems, most of the biosciences are moving towards observations in intact cells and tissues. The development of a large diversity of fluorescent labels has essentially contributed to this trend. To the most important fluorescent labels belong the protein labels, e.g. fluoresceins, rhodamines, Dansyl or BODIPY, and labels for the typically non-fluorescent nucleic acids, e.g. Hoechst 33342 or DAPI.[7] Moreover, chromophores like BCECF, BAPTA, MQAE, SNAFL, SNARF have been used to probe the cellular environmental parameters, e.g. pH, ion concentration (Na^+, Cl^-, Ca^{2+}) or viscosity. In order to minimise the influence of autofluorescence, NIR and IR chromophores have been designed, e.g. Cy3, Cy5, Cy7. Fluorogenic probes, e.g. 7-umbelliferyl phosphate or 7-hydroxicoumarin, are able to digitally signalise modifications in biological systems, since they can fluoresce only under well defined conditions initiated *in situ* by the substance of interest.[7] A particularly important class of chromophores for the fluorescence laser microscopy are the fluorescent proteins; the most noteworthy is the green fluorescent protein (GFP) and its mutants. Furthermore, long-lifetime probes, e.g. lanthanides- and transition-metal-ligand complexes with a lifetime up to few microseconds, have been used in time-resolved fluorescence measurements.[7]

However, the fluorescence labelling by itself may affect the processes under investigation and can falsify the conclusions of the experiments. Since in non-labelling techniques the equilibrium of the biological systems is not disturbed by external signal mediators, such experiments are favoured in biosciences. Non-labelling techniques use the fluorescence signal of endogenous chromophores like NADH, NADPH (nicotinamide adanine dinucleotide phosphate), FAD, FMN (flavin adenine mononucleotide), chlorophyll a and b, keratin, elastin, collagen, melanin or porphyrin.[7] The excitation of these chromophores must be performed within the optical window of the tissue (700 to 1100 nm) so that no interferences with the fluorescence of water and haemoglobin occur.[7] In fluorescence non-labelling experiments, vital processes like the cellular metabolism or the photosynthesis were investigated under natural conditions.[7] Nevertheless, if the fluorescence signal of the intrinsic chromophores is poor or the substance of interest is non-fluorescent, the use of exogenous chromophores is necessary.

1.1.3 Fluorescence microscopy techniques

One of the most widespread fluorescence microscopy tools for the bioscientific research is the fluorescence fluctuation microscopy (FFM), in which the fluctuating fluorescence signal of molecules present in a small observation volume is registered. The FFM techniques are based either on the analysis of fluctuation dynamics, i.e. fluorescence correlation spectroscopy (FCS), or on the analysis of fluctuation amplitudes at equilibrium, e.g. moment analysis of fluorescence intensity distribution (MAFID), photon counting histogram (PCH) analysis or fluorescence intensity distribution analysis (FIDA). The autocorrelation function of the fluctuating fluorescence signal generated in FCS experiments represents the distribution of molecular transport and photodynamic parameters, which characterise processes responsible for the fluctuations in the fluorescence signal. Thus, FCS experiments are particularly suitable to investigate dynamics down to the microsecond timescale.[8–17] In MAFID, PCH and FIDA experiments, the same photon counting distribution of the fluctuating fluorescence signal is generated. However, MAFID[18] is a rather unreliable method, since the photon counting distribution is obtained by aleatory selection of fluorescence fluctuation moments.[20] PCH analysis[19–20] and FIDA[21] are two similar methods based on the theory of photon detection, which counteract the deficits of MAFID. The only difference between PCH analysis and FIDA is of mathematical nature. Since the PCH evaluation is based on convolution of functions, it is slower than the FIDA evaluation, which avoids this time-consuming operation. Both PCH analysis and FIDA found large application especially in the analytic of complex mixtures of similar fluorophores, e.g. in the cellular environment.

Typically, the FFM techniques investigate processes, which occur within one observation volume, thus, single-point experiments. In order to obtain at once more information about the sample with a high spatial resolution, fluorescence imaging techniques have been designed. In imaging experiments, the property of interest, e.g. the steady-state fluorescence intensity, the fluorescence lifetime or the rotational correlation time, is registered in many adjacent observation volumes and, thus, a highly-resolved image of the sample is generated.[22–30] A remarkable imaging method, which combines the spatial resolution of the fluorescence microscopy with high temporal resolution and provides accurate information about the environment of the sample is the fluorescence lifetime imaging (FLIM).[24,26,28–30]

Fluorescence fluctuation techniques

In FCS experiments, the fluctuating fluorescence signal of single molecules or of ensembles of few molecules, which dwell within the observation volume at a time, is registered and compared to itself, i.e. it is autocorrelated. The resulting fluorescence autocorrelation function represents the statistical distribution of the parameters, which describe the transport processes, chemical reactions or photophyiscal processes responsible for the fluctuations of the fluorescence signal (Fig. 1-1).[8]

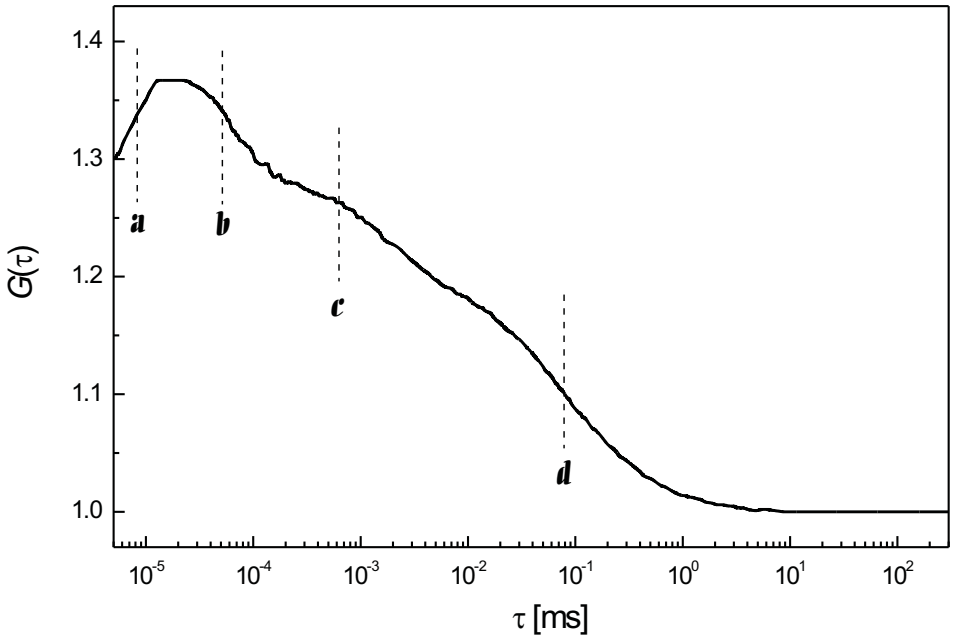

Fig. 1-1: Autocorrelation function $G(\tau)$ of a fluctuating fluorescence signal (modified diagram from reference [8]). The main time-segments of the autocorrelation function are: a) photon antibunching (ns timescale); b) rotational diffusion (ns timescale); c) fast photochemical and photophysical processes on the μs timescale, e.g. triplet-state kinetics, quenching, isomerisation; d) slow processes on the ms and s timescale, e.g. translational diffusion, photobleaching, chemical reactions.

First FCS experiments enabled the measurement of transport parameters, e.g. translational diffusion coefficient, and of chemical reactions rates on the second and millisecond timescale.[31] Later, slow photophysical processes, e.g. photobleaching, could be observed on the same timescale.[32] Furthermore, the use of fast single-photon counters allowed the investigation of processes on the

μs timescale, e.g. triplet-state kinetics, fast isomerisation or quenching.[8] Even processes on the nanoseconds timescale could be observed and studied, e.g. photon antibunching or rotational diffusion. However, FCS experiments on the ns timescale did not find such a large application like the FCS experiments on the μs, ms and s timescale.[8]

The development of confocal and multi-photon microscopes characterised by a high spatial resolution determined an increased utilisation of FCS in the biosciences. Hence, sequencing of DNA, folding and unfolding of proteins, hybridisation and cleavage of DNA and of proteins as well as enzymatic kinetics have been investigated.[9–12] Moreover, FCS experiments on membranes and surfaces contribute to the elucidation of the function of proteins and lipids in the cellular membrane.[33]

An important aspect in FCS is the development of adequate models which accurately simulate the fluorescence autocorrelation function. Models, which include translational 3D and 2D diffusion, photobleaching, triplet-states kinetics, antibunching, rotational diffusion, flow, chemical reactions etc., have been designed.[8,31,32] Most of these models consider a single molecule, which fluoresces after excitation with a continuous wave (cw) laser beam. Thus, the fluorescence signal of the single molecule and its theoretical autocorrelation function are calculated. The cw-models are very suitable for the evaluation of data registered in OPE experiments, in which the excitation is performed with cw laser beams. However, in TPE experiments, in which pulsed-illumination is typically employed, the autocorrelation functions cannot be accurately simulated using these models. Furthermore, the very few models, which take into account pulsed-illumination, consider its influence only on the excitation process, but not on other illumination-dependent processes like stimulated emission or photobleaching.[34]

As mentioned above, the FCS simulation models consider the kinetics of an individual molecule and, thus, the resulting theoretical autocorrelation function describes the statistics of single molecules. In many FCS experiments performed in homogenous medium, the statistics of single molecules are similar to the statistics of ensembles of molecules and, thus, the simulated autocorrelation functions can be assigned without concern to data measured in FCS experiments on ensembles of molecules. However, in the biosciences there are many situations, e.g. if the conformational fluctuations of the DNA fragments are investigated,[13] in which the statistics of ensembles of few molecules is not identical to the statistics of single molecules, i.e. non-ergodic systems. In this case, only if the molecules are

monitored one at a time, certain molecular phenomena can be observed. Hence, it is essential to perform such FCS experiments in single-molecule detection regime in order to obtain a deeper insight in the heterogeneity of biological systems and to correctly evaluate the experimental data using the adequate theoretical approaches.

To the latest advancements in FCS belong techniques like the temporal higher-order FCS, the spatial higher-order FCS (scanning FCS), the dual-colour FCS, i.e. cross-correlation FCS in one-beam or two-foci regime, the RAPID FCS or the coincidence counting microscopy.[14–17] These techniques allowed a quicker evaluation of large amounts of data in high-throughput bioassays or a better separation between similar fluorophores in complex mixtures.[14–17] Furthermore, by combining the FCS with other methods, e.g. fluorescence recovery after photobleaching (FRAP),[35] fluorescence resonant energy transfer (FRET),[15] time-resolved and spectrally-resolved measurements,[36] new insight in the vital cellular phenomena can be achieved.

While the analysis of the fluorescence fluctuation dynamics is largely employed in biochemistry and biosciences, the analysis of the fluorescence fluctuation amplitudes at equilibrium, best described by the photon counting distribution of the fluorescence signal, is a rather new bioscientific tool.

A first method employed in the investigation of the fluorescence fluctuation amplitudes analyses the central and ordinary moments of the fluorescence fluctuations, i.e. the moment analysis of fluorescence intensity distribution (MAFID).[18] The photon counting histogram (PCH) analysis, a method based on the theory of photon detection, avoids the main deficit of MAFID, i.e. the aleatory selection of fluorescence fluctuation moments. In the PCH analysis, the shape of the point-spread function (PSF) is explicitly taken into consideration, while allowing Poissonian number fluctuations of the molecules within the observation volume.[19,20] The fluorescence fluctuations caused by a small number of molecules in the observation volume yield a super-Poissonian distribution, i.e. a bistochastic distribution, of photon counts. Furthermore, the PCH analysis offers another way to distinguish between different species, which is based on different values of the molecular brightness and not on different dynamic parameters like in FCS. The molecular brightness represents the mean number of photons emitted by a molecule within a sampling period. In the last years, the advantages of the PCH technique have also been demonstrated in investigations of biological systems.[19,20] The fluorescence intensity distribution analysis (FIDA), a similar

method to the PCH analysis, was applied in the investigation of DNA hybridisation and cleavage.[21] The main advantage of FIDA over PCH analysis is the shorter evaluation time caused by the elimination of convolution from the calculus of photon counting distributions. A fast evaluation is particularly important for high-throughput bioassays.

Fluorescence imaging techniques

As shown in a recent review,[37] imaging techniques are versatile, indispensable tools for the visualisation and quantification of biological processes *in vitro*, *ex vivo* and even *in vivo* with a sensitivity down to the molecular level. Optical imaging techniques, particularly fluorescence imaging techniques, are of great interest for the biosciences, e.g. in genomic and molecular imaging, since they are non-invasive procedures, which allow insight in the intact sample with a high spatial resolution.[37]

Fluorescence imaging techniques, in which the steady-state intensity is monitored, enabled the 3D visualisation of the morphology of intact tissue, e.g. human skin, pancreatic islets and human cornea.[22–25] The most important features of the steady-state fluorescence imaging are the 3D spatial resolution and the penetration depth, which determine the quality of the images and, thus, the amount of attained information. As previously discussed, these features strongly depend on the employed microscopy technique, i.e. OPE, confocal OPE or MPE microscopy. The advantages of the TPE microscopy over the confocal OPE microscopy could be demonstrated both in labelling as well as in non-labelling experiments on human and mouse skin, pancreatic islets, brain tissue, etc.[22–25] Moreover, in order to improve the quality of the intensity images, deblurring software tools have been designed.[26]

The steady-state intensity is not the only time-independent fluorescence property monitored in imaging experiments. Also the emission wavelength and the fluorescence polarisation found application in these experiments. Differences between the absorption and emission spectra of biomolecules could be exploited in fluorimetry and ratiometric fluorimetry imaging experiments to analyse the content of cells and to distinguish between fluorescing cellular components.[27]

Since different fluorescence properties are differently influenced by modifications of the cellular environment, it appears straightforward that new methods, which employ other fluorescence properties, e.g. time-dependent properties, enable new insight in the functionality of biological systems. Particularly,

the fluorescence lifetime imaging (FLIM), in which the time-resolved fluorescence of molecules is detected, was applied in many branches of the bioscientific research.[29,30] In FLIM experiments, the fluorescence decay curve of molecules is registered and evaluated in each pixel of the intensity image and, consequently, a map of fluorescence lifetimes is generated.[28] FLIM is a very robust technique, which is not affected by small perturbations of the experimental factors, e.g. fluctuations of the chromophore concentration or of the laser power, but it is very sensitive to modifications of the microenvironment. In the biosciences, FLIM was employed to monitor cellular parameters like pH value, ion concentrations, pO_2 or pCO_2, to elucidate vital processes like photosynthesis or cellular metabolism and even for the diagnosis of dermatological diseases.[28–30] Moreover, a very detailed image of the folding mechanism of proteins was obtained by means of FRET combined with FLIM.[30] Using this method a diffraction-unlimited spatial resolution as good as 50 nm can be easily achieved.

An important aspect in non-labelling FLIM experiments on biological systems is the fact that the fluorescence decay curve usually deviates from the monoexponential behaviour, i.e. more than one endogenous species fluoresces within a pixel.[29–30] In order to correctly approximate the experimental data, either a multiexponential or a stretched-exponential FLIM evaluation is necessary. However, only the multiexponential evaluation techniques distinguish between the individual components of the fluorescing mixture. While most of the multiexponential techniques are based on slow iterative approximation methods, the very few fast techniques yield not sufficiently accurate results.

1.2 Structure of this work

As previously discussed, the fluorescence laser microscopy provide a large diversity of versatile tools for bioscientific studies. However, similarly to other fields of research, there are many theoretical and experimental aspects of the fluorescence laser microscopy, which are either unclear or not yet investigated. Some of these aspects that have a particular relevance for the biosciences are discussed and clarified in this work. Two new theoretical approaches are developed, which allow an extended comprehension of the single-molecule fluorescence fluctuation microscopy based on two-photon excitation, one of the most sensitive techniques for biological investigations. Moreover, novel non-invasive fluorescence lifetime imaging experiments are performed, which enable a detailed and accurate insight

in the cellular metabolism and in the functionality of artificial skin as an organ.

Technical details about the microscopy procedure used in the experiments, i.e. fluorescence far-field microscopy based on two-photon excitation, are discussed in chapter 2, *Experiment*.

The development of appropriate simulation models for the fluorescence correlation spectroscopy (FCS) is essential to accurately extract the dynamic parameters of interest from the experimental data. Most of the current theoretical FCS approaches are based on cw illumination and, consequently, on cw excitation. Thus, these models are not appropriate for the simulation of fluorescence autocorrelation functions generated in two-photon excitation experiments, in which pulsed illumination is usually employed. Since the TPE microscopy gains in importance as a powerful bioscientific tool, it is essential to develop adequate simulation models for FCS based on two-photon excitation. In chapter 3, *Photophysical aspects of single-molecule detection by two-photon excitation considering sequential pulsed illumination*, a novel theoretical model for the simulation of the fluorescence signal of single molecules and of its autocorrelation function is described. The main new feature of the model presented inhere is that the time dependence of the excitation flux and, thus, of all illumination-dependent photoprocesses, i.e. excitation, photobleaching and induced emission, is taken into account. This model is validated in FCS experiments on single coumarin 153 and coumarin 314 molecules simultaneously excited by two NIR photons.

Fluorescence fluctuation experiments in single-molecule detection regime are particularly significant for the biosciences, since they provide a comprehensive image of the heterogeneity in non-ergodic biological systems. However, the accurate determination of the single-molecule detection regime received rather little attention until now. In chapter 4, *Quantitative determination of the single-molecule detection regime in fluorescence fluctuation microscopy by means of photon counting histogram analysis*, a method based on the PCH analysis is presented, which allows the calculation of the single-molecule detection limit and, thus, the accurate design of single-molecule fluorescence fluctuation experiments. The results of this approach are verified in FFM experiments on diluted solutions of coumarin 153.

The design of reliable skin models, e.g. artificial skin constructs (ASC), is of special relevance for the dermatological and pharmaceutical research, since they represent economical test-samples in the validation of new medicines. In this regard, it is essential for the artificial skin to have a similar structure and

functionality like the genuine human skin. Particularly important is the barrier function, i.e. selective permeability of the skin, which is strongly related to the epidermal acidic mantle, i.e. epidermal pH-gradient. As discussed in chapter 5, *3D-resolved investigation of the pH-gradient in artificial skin constructs by means of fluorescence lifetime imaging*, fluorescence intensity imaging serves to investigate the morphology of ASC. Moreover, monoexponential FLIM experiments enable the measurement of the 3D pH-gradient in ASC stained with BCECF and the 3D visualisation of the epidermal refractive index in ASC stained with coumarin 314. Thus, for the first time the structure and the acidic mantle of the artificial skin constructs is exhaustively characterised. The relevance of the experiments described in this chapter is twofold: ASC are validated as reliable skin models and the position of FLIM as a versatile biophysical tool is consolidated.

As mentioned in the previous sections, the principal goal of the biophysical research is to develop techniques, which allow a maximum amount on information but minimally disturb the system under investigation. In this frame, the design of non-labelling techniques is of major interest. Chapter 6, *Non-iterative biexponential fluorescence lifetime imaging in the investigation of cellular metabolism by means of NAD(P)H autofluorescence* describes biexponential FLIM experiments on intact ASC, in which the redox metabolism of dermal fibroblasts is imaged basing on NADH and NADPH endogenous fluorescence. The biexponential FLIM approximation is performed using a fast non-iterative method, namely the Prony method, which assures a reduction of the evaluation time of up to 98%. This novel FLIM procedure is of particular interest, since it allows a fast non-invasive monitoring of the cellular metabolism in thick biological systems with submicron resolution. An immediate application of this method will be the investigation of the effect of antidiabetic agents on the insulin secretion in intact pancreatic islets.

References

[1] B. Valeur, *New Trends in Fluorescence Spectroscopy, Applications to chemical and life sciences*, B. Valeur, J.C. Brochon, Springer, Berlin, **2001**, 3-6

[2] J.R. Lakowicz, *Principles of Fluorescence Spectroscopy*, Kluwer Academic/Plenum Publishers, New York, **1999**, 1-21

[3] D.M. Jameson, *New Trends in Fluorescence Spectroscopy, Applications to*

chemical and life sciences, B. Valeur, J.C. Brochon, Springer, Berlin, **2001**, 35-58

[4] U.K. Tirlapur, K. König, *Nature*, 418, **2002**, 290-291

[5] M. Gu, *Advanced optical imaging theory*, Springer, Berlin, **2000**, 143-176

[6] S.W. Hell, *Nonlinear and two-photon induced fluorescence*, J.R. Lakowicz, Plenum Press, New York, **1997**, 361-426

[7] J.R. Lakowicz, *Principles of Fluorescence Spectroscopy*, Kluwer Academic /Plenum Publishers, New York, **1999**, 63-93

[8] J. Widengren, *Fluorescence Correlation Spectroscopy - Theory and Applications*, R. Rigler, E.S. Elson, Springer, Berlin, **2000**, 276-300

[9] Z. Földes-Papp, M. Kinjo, *Fluorescence Correlation Spectroscopy - Theory and Applications*, R. Rigler, E.S. Elson, Springer, Berlin, **2000**, 25-60

[10] A. Paramanik, R. Rigler, *Fluorescence Correlation Spectroscopy - Theory and Applications*, R. Rigler, E.S. Elson, Springer, Berlin, **2000**, 101-129

[11] N.O. Petersen, *Fluorescence Correlation Spectroscopy - Theory and Applications*, R. Rigler, E.S. Elson, Springer, Berlin, **2000**, 162-183

[12] D. Riesner, *Fluorescence Correlation Spectroscopy - Theory and Applications*, R. Rigler, E.S. Elson, Springer, Berlin, **2000**, 225-245

[13] R. Rigler, L. Edman, Z. Földes-Papp, S. Wennmalm, *Single molecule spectroscopy, Nobel Conference lectures*, R. Rigler, M. Orrit, T. Basche, Springer, Berlin, **2001**, 177-193

[14] A. Koltermann, U. Kettling, J. Stephan, T. Winkler, M. Eigen, *Fluorescence Correlation Spectroscopy - Theory and Applications*, R. Rigler, E.S. Elson, Springer, Berlin, **2000**, 187-202

[15] P. Schwille, *Fluorescence Correlation Spectroscopy - Theory and Applications*, R. Rigler, E.S. Elson, Springer, Berlin, **2000**, 360-377

[16] M. Brinkmeier, *Fluorescence Correlation Spectroscopy - Theory and Applications*, R. Rigler, E.S. Elson, Springer, Berlin, **2000**, 379-395

[17] N.L. Thompson, J.L. Mitchell, *Fluorescence Correlation Spectroscopy - Theory and Applications*, R. Rigler, E.S. Elson, Springer, Berlin, **2000**, 438-456

[18] H. Qian, E.L. Elson, *Proc. Natl. Acad. Sci. USA*, 87, **1990**, 5479-5483

[19] J.D. Müller, Y. Chen, E. Gratton, *Fluorescence Correlation Spectroscopy - Theory and Applications*, R. Rigler, E.S. Elson, Springer, Berlin, **2000**, 410-435

[20] Y. Chen, J.D. Müller, J.S. Eid, E. Gratton, *New trends in fluorescence spectroscopy, Applications to chemical and life sciences*, B. Valeur, J.-C. Brochon, Springer, Berlin, **2001**, 292-295

[21] P. Kask, C. Eggeling, K. Palo, Ü. Mets, M. Cole, K. Gall, *Fluorescence spectroscopy, imaging and probes - New tools in chemical, physical and life sciences*, R. Kraayenshof, A.J.W.G. Visser, H.C. Gerritsen, Springer, Berlin, **2002**, 153-178

[22] D.W. Piston, B.R. Master, W.W. Webb, *J. Microscopy*, 178, **1994**, 20-27

[23] N. Takahashi, T. Nemoto, R. Kimura, A. Tachikawa, A. Miwa, H. Okado, Y. Miyashita, M. Iino, T. Kadowaki, H. Kasai, *Diabetes*, 51, **2002**, 25-28

[24] K. König, U. Wollina, I. Riemann, C. Peuckert, K.-J. Halbhuber, H. Konrad, P. Fischer, V. Fünfstück, T.W. Fischer, P. Elsner, *SPIE*, 4620, **2002**, 191-201

[25] B.R. Master, P.T.C. So, E. Gratton, *Biophys. J.*, 72, **1997**, 2405-2412

[26] A. Squire, P.I.H. Bastiens, *J. Microscopy*, 193, **1998**, 36-49

[27] S. Huang, A.A. Heikal, W.W. Webb, *Biophys. J.*, 82, **2002**, 2811-2825

[28] J.R. Lakowicz, K. Berndt, *Rev. Sci. Instrum.*, 62, **1991**, 1727-1734

[29] A. Draaijer, R. Sanders, H.C. Gerritsen, *Handbook of biological confocal microscopy*, J. Pawley, Plenum Press, New York, **1995**, 491-505

[30] W. Becker, A. Bergmann, www.becker-hickl.de/pdf/tcvgbh1.pdf, **2003**

[31] S.R. Aragon, R. Pecora, *J. Chem. Phys.*, 64, **1976**, 1791-1803

[32] J. Widengren, R. Rigler, *Bioimaging*, 4, **1996**, 149-157

[33] T. Schmidt, G.J. Schütz, W. Baumgartner, H.J. Gruber, H. Schindler, *J. Phys. Chem.*, 99, **1995**, 17662-17668

[34] J. Mertz, *Eur. Phys. J. D*, 3, **1998**, 53-66

[35] R. Brock, T.M. Jovin, *Fluorescence Correlation Spectroscopy - Theory and Applications*, R. Rigler, E.S. Elson, Springer, Berlin, **2000**, 132-161

[36] P. Tinnefeld, D.P. Herten, M. Sauer, *J. Phys. Chem.*, 105, **2001**, 7989-8003

[37] S.R. Cherry, *Phys.Med.Biol.*, 49, **2004**, 13-48

Chapter 2

Experiment

2.1 Experimental set-up

In this work, two novel theoretical models of particular significance for the fluorescence fluctuation microscopy (FFM) are experimentally validated, i.e. a model for the simulation of fluorescence autocorrelation functions registered after two-photon pulsed excitation and a theoretical method based on the photon counting histogram (PCH) analysis, which allows an accurate determination of the single-molecule detection regime. Moreover, fluorescence imaging experiments were performed in order to investigate the morphology and functionality of artificial skin constructs (ASC). Employing 3D fluorescence lifetime imaging (FLIM), the cellular metabolism in human dermal fibroblasts and environmental parameters of the artificial epidermis, i.e. pH and refractive index, were monitored with submicron resolution.

The experimental set-up (Fig. 2-1) both in the fluorescence fluctuation experiments as well as in the fluorescence imaging experiments is based on a two-photon laser microscope. The functional principle of the two-photon laser microscopy relies on the registration of the fluorescence signal of exogenous or endogenous chromophores after simultaneous excitation of the molecules with two near infrared (NIR) photons. Since the two-photon absorption cross-section δ of most chromophores is generally low ($\approx 10^{-50}$ cm^4 s), in order to achieve a high excitation rate, $k = \delta \cdot \phi^2$, and, thus, to observe a sufficiently high fluorescence signal, the photon flux ϕ must be very large ($\approx 10^{30}$ photon cm^{-2} s^{-1}). An elegant method to accomplish large values of the photon flux avoiding high energies, which possibly imply the photodamage of the sample, is the use of femtosecond laser pulses. The photon flux of such a laser beam is very high during the pulse

and obviously zero between two consecutive pulses.

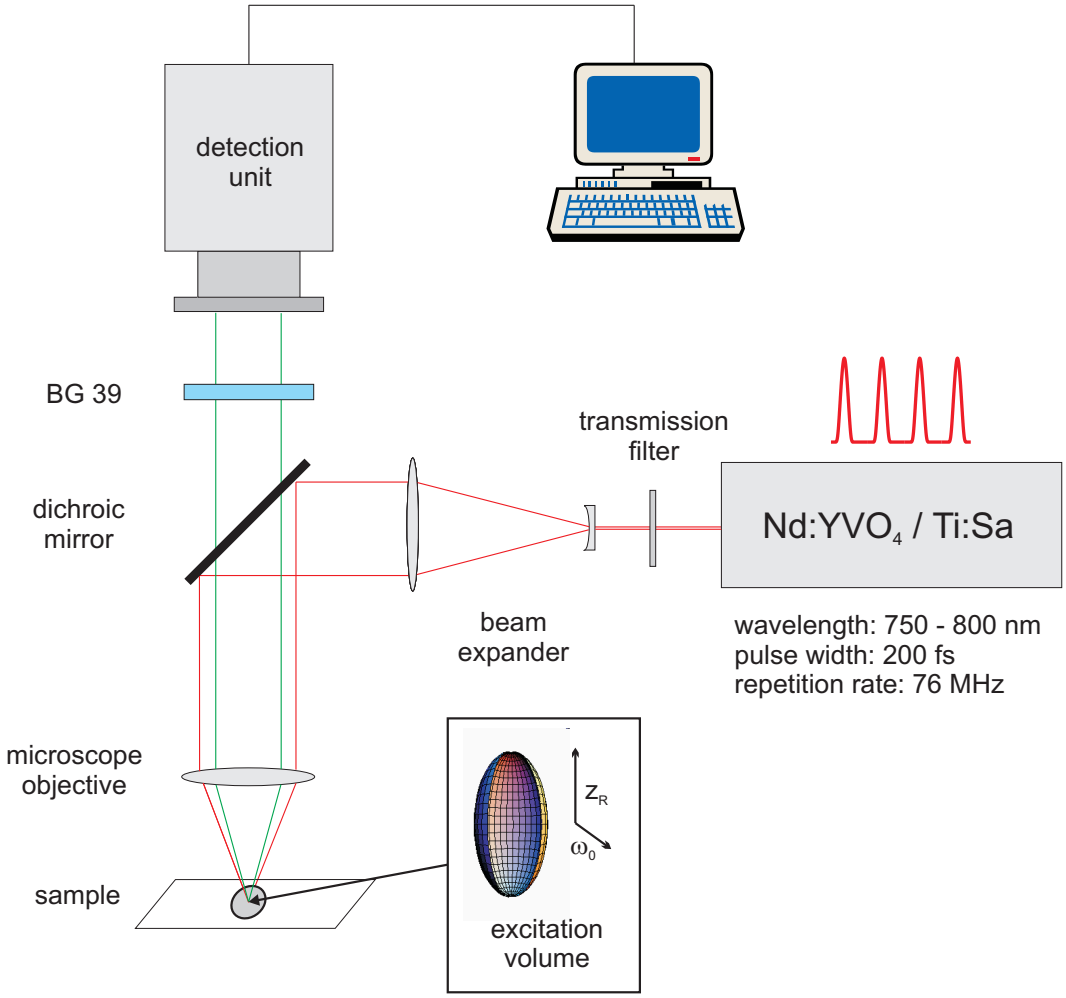

Fig. 2-1: Scheme of the basic experimental set-up used after slight modifications both in the fluorescence fluctuation experiments as well as in the fluorescence imaging experiments. The red beam represents the laser beam (NIR) used for the two-photon excitation, while the green beam represents the fluorescence (visible).

The laser system used in the experiments consists of a Ti:Sa (titanium - sapphire) laser (Mira 900B, Coherent) pumped by a Nd:YVO_4 (neodymium - yttrium vanadate) laser (Verdi10, Coherent). The frequency-doubled cw (continuous wave) beam of the Nd:YVO_4 laser of 532 nm wavelength and 10 W output is used as excitation source for the Ti:Sa crystal. The laser pulses in the tunable Ti:Sa laser are generated by means of passive mode-locking and are characterised by 200 fs pulse width and 76 MHz repetition rate. The wavelength λ of the Ti:Sa laser beam was varied between 750 nm and 850 nm (spectral width $\approx$ 5 nm), while the mean output power amounted to $\approx$ 1.5 W. The Ti:Sa laser beam is

attenuated using transmission filters (between 20% and 1%), in order to achieve the desired excitation photon flux at the sample. The characteristics of the laser beam, i.e. wavelength and mean output, were measured in front of the transmission filter.

In order to achieve a better lateral resolution at the sample, the attenuated laser beam is ten-fold expanded by a beam expander made of a convex and a concave lens. The expanded laser beam is reflected into the microscope by a dichroic mirror, which is highly transmitting for $\lambda \in [430; 700]$ nm and highly reflecting for $\lambda > 700\,\text{nm}$. A microscope objective focuses the beam into the sample and, thus, the photon flux of the pulsed beam is additionally increased by reducing the cross-section of the beam. In the fluorescence fluctuation experiments a $40\times$ oil-immersion objective (Neofluar, numerical aperture $NA = 1.3$, Zeiss), while in the fluorescence imaging experiments a $63\times$ water-immersion objective (Achroplan, $NA = 0.95$, Zeiss) were used. It was proven that the mean excitation power at the sample scales linearly with the mean laser power. The average power at the sample is three times lower than that behind the transmission filter. As mentioned before, the high photon flux of the focused laser beam allows at the sample two-photon excitation followed by fluorescence. The fluorescence of the sample is collected by the same microscope objective and put through the dichroic mirror and the band-pass filter (BG39, Schott). In this way a good separation of the fluorescence (visible, ≈ 500 nm) from the laser light (NIR, ≈ 800 nm) is possible. Further, the fluorescence light is focused on the detection unit, which is different in the fluorescence fluctuation experiments and in the fluorescence imaging experiments, respectively.

At the sample, only the chromophore molecules, which dwell within a small region around the focus, i.e. excitation volume (Fig. 2-1), can be simultaneously excited with two photons and, thus, can fluoresce. The excitation volume is defined as the region, in which the excitation rate k is larger than k_0/e, where k_0 is the maximal excitation rate at the focal point. Thus, the probability that the fluorescence of a certain molecule is detected, strongly depends on the position of the molecule with respect to the focused laser beam and on the spatial distribution of the excitation rate. Rigorously, the probability that a fluorescing molecule is detected is given by the transfer function, which contains the spatial distribution both of the excitation rate and of the fluorescence rate. If considering that the fluorescence of molecules is isotropically distributed and no perturbations arise on the detection path, the transfer function is identical to the spatial distribution of

the excitation rate. Since the spatial distribution of the excitation rate indicates whether a certain molecule is detected or not, it also defines the spatial resolution of the microscope. The spatial distribution of the two-photon excitation rate, i.e. $k = \delta \cdot \phi^2$, can be calculated from the unitless distribution of the photon flux ϕ of the focused laser beam, i.e. the point spread function $PSF(r, z)$. Here is r the cylindrical coordinate perpendicular to the optical axis and z is the cylindrical coordinate along the optical axis.

The Ti:Sa laser beam is a TEM_{00} beam, which is characterised by a symmetrical 2D-Gaussian cross-section distribution of the electrical field $\overrightarrow{E}$ and of the photon flux ($\phi \propto |E_0|^2$). At the sample, a 3D distribution of the photon flux, i.e. the point spread function $PSF(r, z)$, is generated by focusing the laser beam. The PSF is a complicated function, which cannot be analytically calculated for high aperture objectives. Models, which rigorously describe the PSF, are, for example, the paraxial approximation or the scalar and vectorial Debye approximations. However, a simple but sufficiently reliable assumption is to consider that the PSF and, thus, the distribution of the excitation rate is given by a 2D-Gaussian Lorentzian function:

$$PSF(r,z) = \frac{4\,\omega_0^2}{\pi^2\,\omega^2(z)} \cdot e^{-\left[4\,r^2/\omega^2(z)\right]} \qquad \text{with} \qquad \omega^2(z) = \omega_0^2 \left[1 + \left(\frac{z}{z_R}\right)^2\right]. \tag{2.1}$$

Thus, the shape of the excitation volume is well approximated by a rotational ellipsoid with ω_0 the secondary axis and z_R the principal axis:

$$\omega_0 = \frac{\lambda \cdot f}{\pi \cdot \omega_1} \qquad \text{and} \qquad z_R = \frac{\pi \cdot \omega_0^2}{\lambda}\sqrt{e^2 - 1}\,. \tag{2.2}$$

Here, f is the focal distance of the microscope objective, ω_1 the half width of the expanded laser beam and λ the excitation wavelength. In preliminary experiments the validity of this assumption was verified for our set-up and the spatial resolution both in the x-y plane perpendicular on the optical axis, i.e. $2 \cdot \omega_0$, and in z direction on the optical axis, i.e. $2 \cdot z_R$, was determined for both microscope objectives.

The distribution of the excitation rate, i.e. the distribution of the fluorescence signal, in the x-y plane was imaged using a CCD camera. As shown in Fig. 2-2, this distribution is accurately approximated by a Gaussian function. The $FWHM$ (full width at half maximum) of the Gaussian function indicates the lateral resolution of the microscope objective. Since the spatial resolution strongly

depends on the excitation wavelength λ, experiments at different λ between 750 and 850 nm were performed. At $\lambda = 800$ nm the lateral resolution amounts to 700 nm for the 40× oil-immersion objective and to 640 nm (Fig. 2-2) for the 63× water-immersion objective. These results were obtained in experiments on a 10 μmol L^{-1} solution of coumarin 153 in ethanol and also verified in experiments with fluorescent microbeads of 500 nm diameter.

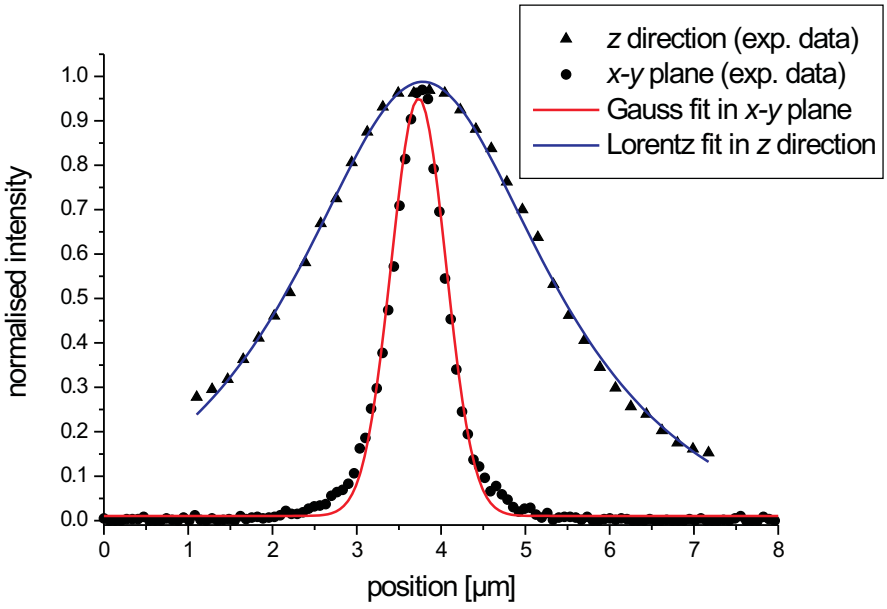

Fig. 2-2: Spatial distribution of the two-photon excitation rate in x respectively y direction as well as in z direction. In the x-y plane the experimental data could be well approximated by a Gaussian distribution, while on the optical axis (z direction) a Lorentzian distribution was the appropriate fit. The experiments were performed with the 63× water-immersion objective ($NA = 0.95$) at 800 nm excitation wavelength.

On the optical axis, in z direction, the distribution of the excitation rate was determined by monitoring the fluorescence of a monomolecular layer of FITC (fluorescein isothiocyanate) at different z positions with respect to the focal point of the microscope objective. Since in z direction the fluorescence distribution of a monomolecular layer can be approximated with a δ-function, the display of the fluorescence signal as a function of z position represents the distribution of the excitation rate on the optical axis. As shown in Fig. 2-2, this distribution is accurately approximated by a Lorentzian function. The axial resolution at $\lambda = 800$ nm, i.e. the $FWHM$ of the Lorentzian function, amounts to 3.2 μm for the 40× oil-immersion objective and to 2.7 μm for the 63× water-immersion

objective.

Slight modifications of the described two-photon laser microscope allowed, on one hand, the detection on the single-molecule level in fluorescence fluctuation experiments and, on the other hand, a high temporal resolution necessary in fluorescence lifetime imaging (FLIM) experiments. In the following sections, these modifications are explicitly discussed.

2.2 Fluorescence fluctuation experiments

The detection unit in the fluorescence fluctuation microscopy (FFM) experiments consists of an avalanche photodiode (APD, SPCM-AQ-131, EG&G Optoelectronics), i.e. a single-photon counter, characterised by a dead time of 31 ns and a maximum detection efficiency of 70% at 550 nm. The amplified signal of the APD is directed to a multichannel scaler (MCD-2E, 7882, FAST ComTec) with 131072 channels and variable channel width. In our experiments, the channel width was adjusted to 10 and 100 μs corresponding to frequencies of 100 and 10 kHz, respectively. The signal of the multichannel scaler is stored as ASCII file.

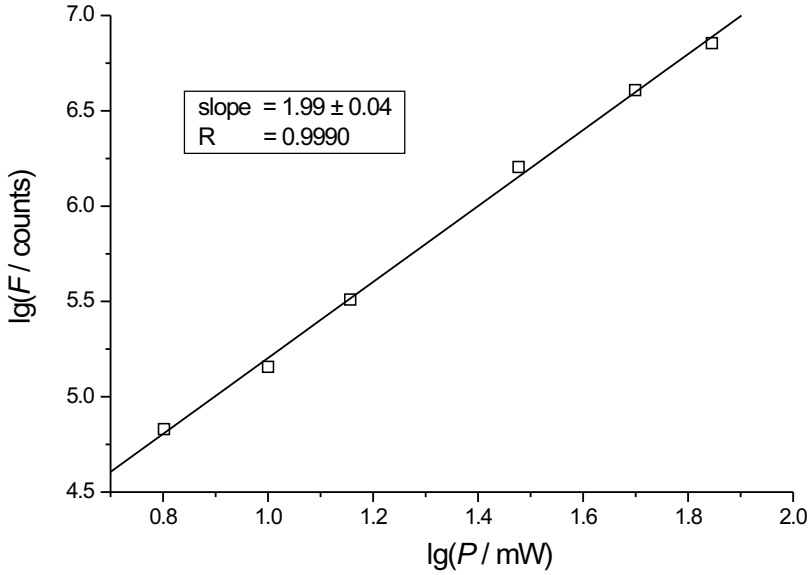

Fig. 2-3: Fluorescence signal F of a 50 μmol L^{-1} solution of rhodamin B in ethanol registered at different values of the mean laser power P and at $\lambda = 830$ nm.

In preliminary experiments performed with the FFM set-up, it has been verified that the studied chromophores are simultaneously excited by two identical

NIR photons. It is known that in the case of two-photon excitation, if no saturation of the first excited singlet state occurs, the fluorescence signal F is given by the product $\varphi \cdot \delta \cdot K \cdot c \cdot \eta \cdot P^2$, with φ the fluorescence quantum yield, η the total detection efficiency, K the instrumental constant and c the concentration of the chromophore solution. Thus, the fluorescence signal F scales quadratically with the mean excitation power P and the slope of the double-logarithmic plot lg(F)-lg(P) amounts to 2. In experiments on all the employed chromophores the slope of the lg(F)-lg(P) plot varied between 1.95 and 2.03, as exemplified in Fig. 2-3. These results indicate that only two-photon excitation occurs in our experiments. Since the laser pulse lasts only few hundred femtoseconds and the dark period between two consecutive laser pulses is usually longer than the fluorescence lifetime, a molecule can absorb only simultaneously, i.e. during one laser pulse, the two NIR photons.

Furthermore, the active two-photon absorption cross-sections $\varphi \cdot \delta$ of the investigated chromophores have been determined. Under similar experimental conditions (K, P and λ constant), the unknown two-photon cross-section of the substance of interest can be calculated using as reference a chromophore with known two-photon absorption cross-section:

$$\varphi \cdot \delta = \frac{\eta \cdot c}{\eta_R \cdot c_R} \cdot \frac{F_R}{F} \cdot \frac{1}{\varphi_R \cdot \delta_R} \,. \tag{2.3}$$

The index R indicates the reference dye, in our case, coumarin 1 (*7-diethylamino-4-methylcoumarin*). In order to calculate the active two-photon absorption cross-section $\varphi \cdot \delta$ from the fluorescence signal F, the total detection efficiency η of both the substance of interest and the reference must first be determined. Considering the transmittance of the microscope objective, of the dichroic mirror and of the band-pass filter and the detection efficiency of the APD, total detection efficiencies η in the range of 1% to 3% have been obtained for all the used chromophores. The active two-photon cross-sections determined by means of this method are given in following sections, for which they are relevant.

Using the set-up described above, fluorescence fluctuation experiments on the single-molecule detection level were performed on 50, 100, 200, 400 and 1000 pmol L^{-1} solutions of coumarin 153 and 314 in glycol. Thereby, the corresponding mean number of molecules present within the excitation volume amounted to 0.024, 0.047, 0.095, 0.196 and 0.48, respectively. Thus, only the fluorescence of one or very few molecules is detected at a time. Most of the time, no molecules are present in the excitation volume and only a low background is registered.

If a molecule diffuses into the observation volume, it is excited and fluoresces. The detected signal increases dramatically. After a period, the molecule diffuses out of the excitation volume or it is photobleached and the detected signal decreases to the background level. Consequently, if the channel width of the MCS is short enough to trace diffusion and photobleaching, the detected signal shows a *fluorescence burst* during the presence of a molecule within the excitation volume. Typical single-molecule *fluorescence bursts* of a 100 pmol L^{-1} solution of coumarin 153 in glycol are displayed in Fig. 2-4.

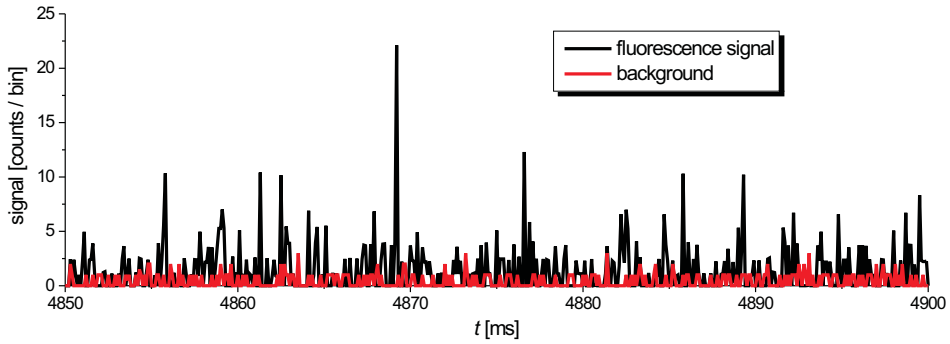

Fig. 2-4: Fluctuating fluorescence signal of a 100 pmol L^{-1} solution of coumarin 153 in glycol and background signal of pure glycol. The bursts indicate with high probability the fluorescence of individual molecules.

The obtained experimental data, i.e. the fluctuating fluorescence signal, are further evaluated to generate either fluorescence autocorrelation functions or photon counting histograms. In this way, two new developed theoretical models for the fluorescence fluctuation microscopy were validated.

2.3 Fluorescence imaging experiments

In fluorescence imaging experiments the sample is scanned with the excitation laser beam and, thus, not only the fluorescence stemming from one excitation volume but from a larger area is detected without loss of spatial resolution. Thereby, the laser beam is synchronously driven by two galvanometric mirrors (GSI Lumonics) as shown in Fig. 2-5.

The scanning unit, characterised by 0.95 μs dwell time per pixel, is integrated into the basic set-up (Fig. 2-1) between the beam expander and the microscope. The resulting ray bundle is collimated by two convex lenses.

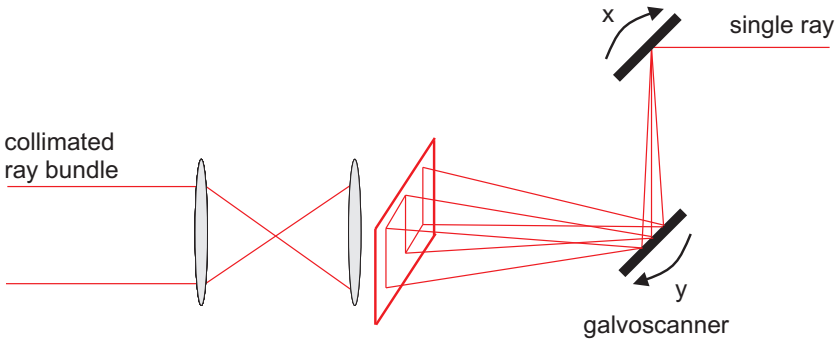

Fig. 2-5: Scanning unit used in fluorescence imaging experiments.

The detection unit in the fluorescence imaging experiments is an intensified CCD camera (PicoStar, LaVision), which is able to image the scanned region at the sample. The fluorescence photons emitted by the sample hit the photocatode of the ICCD camera and generate photoelectrons only if a voltage of -200 V is applied. In *comb mode*, the photocatode is loaded only within a time-gate of variable width (between 200 ps and 1000 ps) and, thus, the requirements for time-resolved measurements, i.e. FLIM experiments, are fulfilled. The resulting photoelectrons are accelerated and reach the multichannel plate (MCP), where the signal is up to 1000$\times$ amplified. On the anode, a phosphorous screen, the photoelectrons generate photons, which are further imaged on the CCD chip. Consequently, only information about the fluorescence intensity but not about its wavelength can be registered.

The time-gate of the ICCD camera can be shifted with respect to the input trigger, i.e. the laser pulse, in steps of minimum 25 ps, in order to register the fluorescence decay curve. The fluorescence decay can be measured either in bulk experiments or in fluorescence lifetime imaging (FLIM) experiments. In the latter case, in each pixel of the intensity image a fluorescence decay curve is recorded and, thus, a fluorescence lifetime image is generated.

The temporal resolution of the detection unit is given by its jitter ($\approx$ 10 ps), i.e. the accuracy with which the position and the width of the time-gate can be measured. In order to verify the temporal resolution, FLIM experiments on DASPI solutions of different viscosities were performed (Fig. 2-6). The delocalised π-system in the DASPI molecule allows free rotation around the double bond between the pyridine and the aryl ring (Fig. 2-7). Due to the energy loss through internal rotation, the fluorescence lifetime of DASPI is rather short. If the viscosity of the environment increases, the internal rotation is inhibited and the fluorescence lifetime increases.

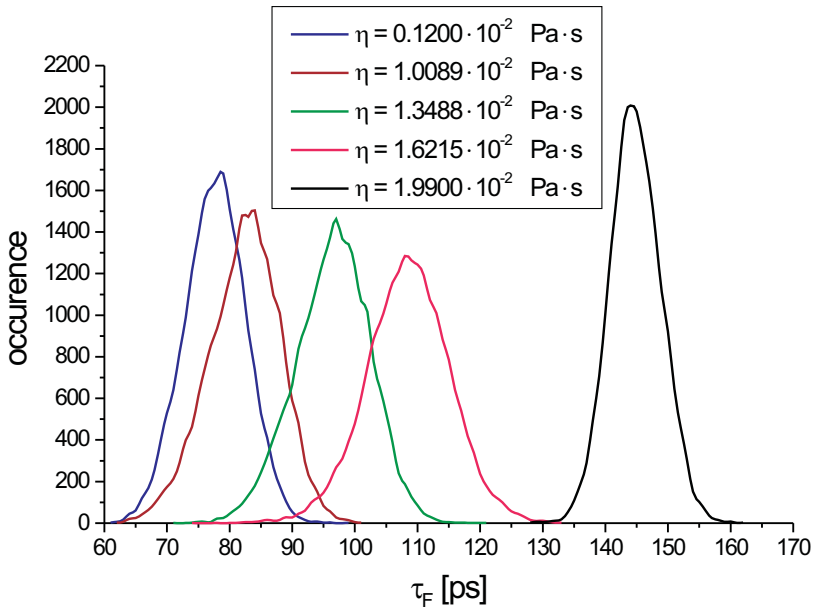

Fig. 2-6: Fluorescence lifetime distributions obtained in FLIM experiments with DASPI solutions of different viscosities. The correct succession of the fluorescence lifetimes indicates that the temporal resolution is better than 10 ps.

Since the viscosity of the DASPI solutions used in the experiments varied only slightly, the differences between the fluorescence lifetimes were expected to be in the same range as the jitter of the detection unit. The correct succession of the fluorescence lifetimes of DASPI corresponding to the viscosities of the solvents indicates that in solution the temporal resolution of the ICCD camera is better than 10 ps (Fig. 2-6). In biological samples a slight deterioration of the temporal resolution is expected due to an increase of scattered light.

2.4 Chromophores

The relevant exogenous chromophores employed in the fluorescence microscopy experiments are: rhodamin B (*o-(6-diethylamino-3-diethylamino-3H-xanthe-9-yl)benzoic acid*), coumarin 314 (*2,3,5,6-1H, 4H -tetrahydro-9-carboethoxyquinolizino-(9,9a,1)coumarin*), coumarin 153 (*2,3,5,6-1H, 4H -Tetrahydro-8-trifluormethylquinolizino-(9,9a,1)coumarin*), DBT22 (*3,7-bis (diarylamino)-dibenzothiophen-S,S-dioxide*), BCECF (*2,7-bis (2-carboxyethyl)-5(6)-carboxyfluorescein*) and DASPI (*4-[4-(dimethylamino)-styryl]-1-methylpyridinium iodide*). Their chemi-

cal structures are shown in Fig. 2-7.

Furthermore, studies on the coenzymes NADPH (*nicotinamid-adenine-dinucleotid-phosphate*) and NADH (*nicotinamid-adenine-dinucleotid*) have been performed to monitor the cellular metabolism of human dermal fibroblasts. The chemical structure of the coenzymes is also displayed in Fig. 2-7.

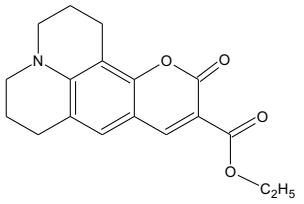

Coumarin 314

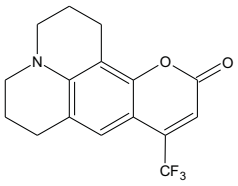

Coumarin 153

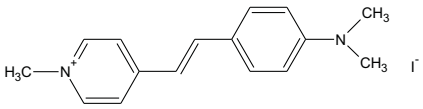

DASPI

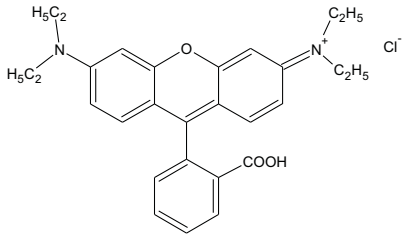

Rhodamin B

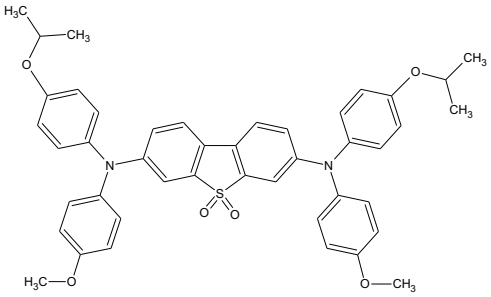

DBT22

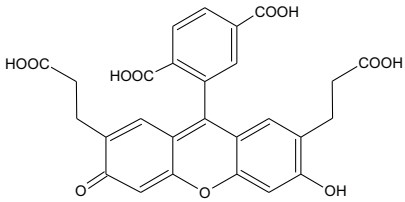

BCECF

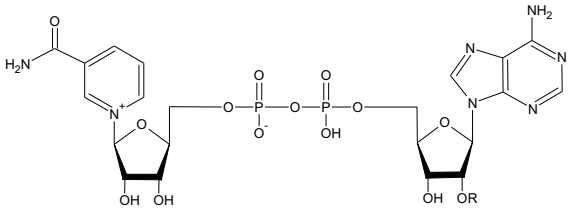

NADH / NADPH

Fig. 2-7: Molecular structures of the endogenous and exogenous chromophores used in the fluorescence experiments. The aryl radicals in the DBT22 molecule are *p-methoxyphenyl* and *p-isopropyloxyphenyl* radicals, respectively. The radical R in the NADH molecule is a hydrogen radical, while in the NADPH molecule it is a phosphate radical.

Chapter 3

Photophysical Aspects of Single Molecule Detection by Two-Photon Excitation Considering Sequential Pulsed Illumination

3.1 Abstract

An important goal in single molecule fluorescence correlation spectroscopy is the theoretical simulation of the fluorescence signal stemming from individual molecules and its autocorrelation function. The simulation approaches developed up to now are based exclusively on continuous-wave (cw) illumination and consequently on cw-excitation. However, this approximation is no longer valid in the case of two-photon excitation, for which pulsed illumination is usually employed. We present a novel theoretical model for the simulation of the fluorescence signal of single molecules and its autocorrelation function with consideration of the time dependence of the excitation flux and, thus, of all illumination-dependent photoprocesses: two-photon excitation, induced emission and photobleaching. Further important characteristics of our approach are the consideration of the dependence of photobleaching rate on illumination and the low intersystem-crossing rates of the studied coumarins. Moreover, using our approach, we can predict quantitatively the effect of the laser pulse width on the fluorescence signal of a molecule, i.e. the contributions of the photobleaching and saturation effects and, thus, we calculate the optimal laser pulse width.

The theoretical autocorrelation functions were fitted to the experimental data, and we could ascertain a good agreement between the resulting and the expected

parameters. The most important parameter is the photobleaching constant σ, the cross section of the transition $S_n \leftarrow S_1$, which characterises the photostability of the molecules independent of the experimental conditions. Its value is $1.7 \cdot 10^{-23}$ cm^2 for coumarin 153 and $5 \cdot 10^{-23}$ cm^2 for coumarin 314.

3.2 Introduction

The detection of individual fluorescent molecules by laser-induced fluorescence microscopy opened new horizons for the investigation of the dynamics in heterogeneous systems like those met in analytical chemistry, biology and medicine.[1−3] In this respect, the fluorescence correlation spectroscopy (FCS) has proven to be a powerful tool for the analysis of molecular dynamics and photodynamics at room temperature by one- and two-photon excitation.[1,2,4,5] An important step in the evolution of FCS represents the development of suitable theoretical models for the simulation of the fluorescence autocorrelation functions.

One of the first models (Aragon and Pecora), which takes into consideration translational and rotational diffusion and chemical reactions, is based on a modified first diffusion law and generally describes the autocorrelation functions obtained by FCS.[5−7] From the time profile of the autocorrelation functions obtained in this manner local diffusion coefficients and rates of different chemical reactions can be obtained.[5,8] Application of this model has also been extended to single-molecule FCS.

However, not only transport processes and chemical reactions but also photophysical processes affect the fluorescence signal and its autocorrelation function. Thus, new theoretical models had to be developed in order to attain the kinetic rates of these photophysical processes, e.g. intersystem-crossing (ISC).[9,10] The model, which includes triplet state dynamics, is derived from the approach of Aragon and Pecora and describes the behaviour of the molecule in the excitation volume using a closed three-level approach, i.e. considering that the molecule can reside only in the states S_0, S_1 or T_1.

An undesired process which limits the number of fluorescence photons emitted by an individual molecule and thus strongly affects the features of the autocorrelation function is the photobleaching, defined as the irreversible photophysical interruption of the excitation-emission cycles between S_0 and S_1. Thus, the determination of the photobleaching parameters is crucial for the selection of appropriate dyes for single molecule FCS experiments. The difficulties in rigor-

ously describing the process of photobleaching arise from the multitude of photobleaching mechanisms, which have to be taken into consideration in a theoretical approach. Some groups have developed models, which take into account different photobleaching mechanisms, e.g. illumination independent photobleaching through the singlet and triplet states or illumination dependent photobleaching via two-step photolysis.[11−14] The derived mathematical expression of the simulated autocorrelation function has largely been employed in the approximation of autocorrelation curves achieved by one photon excitation (OPE) and by two-photon excitation (TPE).[15,16] An important insight attained by these means is that a major contribution to the process of photobleaching results from the photobleaching via triplet states.[14] Here it is important to mention that all these models are designed for the case of either one or two-photon cw-excitation. However, in the two-photon excitation experiments pulsed illumination is usually employed and, as already pointed out by Mertz, this kind of illumination has severe consequences on the multi-photon excitation rate as compared to cw-illumination.[17] Mertz defines in his model a set of differential equations, which describes the occuring photophysical processes (excitation, induced emission, photobleaching, fluorescence, intersystem-crossing) considering pulsed multi-photon excitation. This set of equations combined with a modified second diffusion law leads to the autocorrelation function of the fluorescence signal of a pulsed-illuminated molecule. In this frame, the photobleaching parameter (quantum yield of photobleaching) is assumed to be a constant independent from the pulsed excitation flux.[17] However, in the following discussion the comparison of the simulation data with experimental data shows that the photobleaching yield depends strongly on the excitation flux and, thus, it is a time dependent parameter.[17] Nevertheless, the model was not corrected for a time-dependent photobleaching parameter.

We develop a kinetic rate model in order to simulate the fluorescence autocorrelation functions obtained by two-photon excitation. The main novel feature of our model is the consideration of the effect of pulsed illumination on all intensity dependent photoprocesses, i.e. not only two-photon excitation but also photobleaching and induced emission. Whereas all former cw-models consider steady-state conditions, we perform a time-dependent treatment, which is essential for all pulsed photoprocesses.

Experiments were performed with coumarin 153 (C153) and coumarin 314 (C314). Therefore, our model considers the special case of these dyes, which are characterised by low intersystem crossing rates[18−20] as compared to other

coumarins or to rhodamines.[14] Consequently, all photoprocesses implying triplet states proceed very slowly compared to fluorescence and can be neglected. Thus, the major photobleaching channel, i.e. through higher triplet states, does not occur. The only possible loss channel is photobleaching through singlet states. As far as the photobleaching rate (the rate of the transition $S_n \leftarrow S_1$) is concerned, we assume that it scales linearly with the excitation flux ϕ and, consequently, that the ground state depletion rate scales with the third power of the excitation flux. This assumption is in good agreement both with our experimental results and with the results of other authors obtained when ignoring intersystem crossing ISC.[16,17,21] In other words, the molecule undergoes photobleaching, if it reaches S_n, out of which it cannot return to the ground state S_0. The relevant transitions are presented in Fig.3-1.

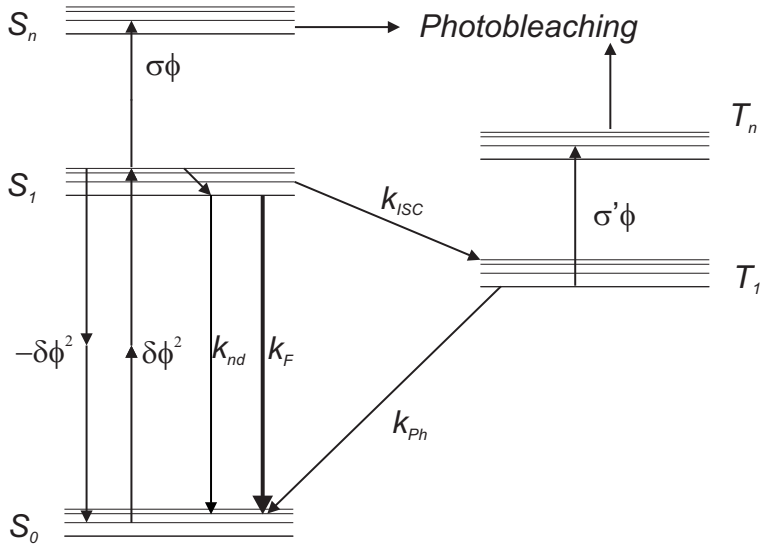

Fig. 3-1: Simplified Jablonski diagram. Molecular constants: δ two-photon excitation cross-section, σ cross-section of the transition $S_n \leftarrow S_1$ (photobleaching constant), σ' cross-section of the transition $T_n \leftarrow T_1$ (photobleaching constant). Transition rates: k_{nd} rate of the non-radiative decay $S_0 \leftarrow S_1$, k_F fluorescence rate, k_{Ph} phosphorescence rate, k_{ISC} intersystem crossing rate, $\delta\,\phi^2$ two-photon excitation rate, $-\delta\,\phi^2$ rate of the induced emission, $\sigma\,\phi$ rate of the transition $S_n \leftarrow S_1$, $\sigma'\,\phi$ rate of the transition $T_n \leftarrow T_1$. The relaxation rate k is defined as $k = k_{nd} + k_F$ and can be calculated as $k = 1/\tau_F$ with τ_F fluorescence lifetime. The fluorescence rate k_F can be determined as $k_F = \phi_F/\tau_F$ with ϕ_F fluorescence quantum yield.

Since the photobleaching rate depends on the excitation flux and this is described by a time function given by the characteristics of the laser, photobleaching will be switched on during the laser pulse and switched off after it. Thus, photo-

bleaching is a time dependent process like excitation and induced emission.

Evident proof that the consideration of time-dependent excitation flux is necessary provides the comparison of the photobleaching rates obtained when employing the well-known cw-model and our model, respectively. They are in the first case up to six orders of magnitude larger than in the second case.

We measured the molecular specific cross-section σ of the transition $S_n \leftarrow S_1$, which characterises the photobleaching process. Using this constant we can compare the photostability of substances with low ISC rates independently from the excitation flux at which it has been determined. Usually, the photostability of substances is compared in terms of ground state depletion rate or of photobleaching yield.[14] However, these indicators depend e.g. on the excitation flux (laser power) and, therefore, they are specific and different for each experiment.

3.3 Kinetic Rate Model

The fluorescence signal of a molecule is directly proportional to the population of the first excited state. Thus, to obtain the most probable time profile of the fluorescence signal *F(t)* of an individual molecule, the probability of occupancy of the first singlet state $S_1(t)$ must be determined. By employing a kinetik rate model, which includes photophysical processes and diffusion, the time dependence of the probability of occupancy of S_1 can be obtained.

Since we are interested in the photophysical behaviour of C153 and C314 molecules and these undergo practically no ISC, we will consider in our model only irreversible photobleaching through higher singlet states via $S_n \leftarrow S_1$ transitions. Phosphorescence and photobleaching through triplet states can be neglected in this case. Furthermore, we assume that the rate of non-radiative conversion in S_1 is sufficiently large so that, after the pulse, the molecule is with high probability in the vibrational ground state of S_1. Consequently, the photobleaching rate is considered to scale linearly with the excitation flux. An approximation of the photobleaching rate by a constant results in FCS functions, which are not validated by our experimental data: the resulting photobleaching rates are not constant for different laser powers but scale linearly with the excitation flux. This is an unequivocal evidence that the rate of ground-state depletion scales cubically with the excitation flux.

We consider an individual molecule which repeatedly undergoes excitation and emission as it freely diffuses through a defined volume V, the effective excitation

volume. The absorption-fluorescence cycles are interrupted by diffusion out of the volume V or by photobleaching.

The effective TPE volume V is defined as:[22]

$$V = \frac{\left(\int\int h^2(r,z)\,2\pi\,r\,z\,dr\,dz\right)^2}{\int\int h^4(r,z)\,2\pi\,r\,z\,dr\,dz} = \gamma^{-1}\int\int h^2(r,z)\,2\pi\,r\,z\,dr\,dz \qquad (3.1)$$

where r and z are cylindrical coordinates, γ is the volume contrast and $h(r,z)$ the point spread function, i.e. the unitless intensity profile.[22] For the evaluation of V we approximate the point spread function $h(r,z)$ by a 2D-Gaussian-Lorentzian distribution.[22] The expansions of the volume V are the principal $1/e^2$ limited axis z_e on the optical axis and the secondary $1/e^2$ limited axis ω_0 in the focal plane.

The diffusion of the molecule through the excitation volume is quantified by the mean diffusion time τ_D calculated for a 2D-Gaussian-Lorentzian intensity profile as:[17]

$$\tau_D = \frac{\omega_0^2}{1.8\,D}\,ln\left(\frac{6\,z_e}{\omega_0}\right) \qquad (3.2)$$

where D is the local diffusion coefficient. Since the excitation volume is much smaller than the sample volume, the photobleached molecules can be replaced by new molecules diffusing into the excitation volume so that competition between diffusion and photobleaching occurs. The renewal of the bleached molecules is taken into consideration by defining the diffusion time as the mean diffusion time according to Mertz, i.e. the period between the molecule's first entering the excitation volume and leaving it for the last time.[17]

As mentioned in the introduction, an important difference between one- and two-photon fluorescence microscopy is that in the former cw, while in the latter pulsed illumination, is usually employed. The effects of pulsed as opposed to cw illumination have significant consequences for the photobleaching rate, the excitation rate and the rate of induced emission. Thus, it is important to regard the excitation flux in our model as a time function $\phi(r,z,t')$ which restores the time profile of the laser pulses (t' represents the time axis during the period including the laser pulse and the dark period thereafter). The excitation flux is the time-dependent excitation intensity at the sample with units of $photon\,cm^{-2}\,s^{-1}$.

To simplify our approach, we introduce two approximations concerning the excitation flux $\phi(r,z,t')$:

- The excitation volume is uniformly illuminated, i.e. the point spread function $h(r, z)$ is constant within the limits ω_0 and z_e, and zero outside.

- The time profile of the laser pulse is rectangular.

The first simplification is justified as long as the excitation volume V is small (holds for TPE). The second approximation does not significantly influence the time profile of the fluorescence signal and its autocorrelation function.[17] Mathematically, the simplified excitation flux can be expressed as:

$$\phi(r, z, t') = \frac{I(t')}{\pi\,\omega_0^2} \tag{3.3}$$

$$I(t') = \begin{cases} I_0\,, & t' \in [0\,, \tau_P] \\ 0\,, & t' \in [\tau_P\,, \tau_0] \end{cases} \tag{3.4}$$

where τ_P is the pulse width, $1/\tau_0$ is the repetition rate of the laser and I_0 is the peak intensity at the geometric focal centre. In the following, we denote the function $\phi(r, z, t')$ as $\phi(t')$ and the peak flux $I_0\,(\pi\,\omega_0^2)^{-1}$ as ϕ_0.

Under these assumptions, the set of differential equations describing the behaviour of an individual C153 or C314 molecule inside the excitation volume V according to Fig. 3-1 is given by:

$$\frac{d}{dt'}\begin{pmatrix} S_0(t') \\ S_1(t') \end{pmatrix} = \begin{pmatrix} -\delta\,\phi^2(t') - \frac{1}{\tau_D} & \delta\,\phi^2(t') + k \\ \delta\,\phi^2(t') & -\delta\,\phi^2(t') - k - \sigma\,\phi(t') - \frac{1}{\tau_D} \end{pmatrix}\begin{pmatrix} S_0(t') \\ S_1(t') \end{pmatrix} \tag{3.5}$$

Thereby, we took into consideration that the populations of the S_0 and S_1 states can be reduced by both photophysical processes and diffusion.

To solve this set of equations, we employed an iterative method based on the following physical insights:

- During the laser pulse the molecule practically does not relax in S_0 by fluorescence or non radiative decay ($\tau_F \gg \tau_P$; τ_F is typically of the order of few nanoseconds, while τ_P is on the femtosecond timescale) and has insufficient time to diffuse out of the excitation volume ($\tau_D \gg \tau_P$; τ_D is on the order of micro- or milliseconds).

- After the laser pulse, the molecule relaxes in S_0 by fluorescence or non radiative decay and can diffuse out of the observation volume, but it can be neither excited nor photobleached ($\delta\,\phi^2(t') = 0$, $\sigma\,\phi(t') = 0$).

Hence, we can divide the former set of differential equations into one set considering the period during the pulse $[0\,,\tau_P]$ and another considering the "dark period" τ_0 after the pulse $[\tau_P\,,\tau_0]$.

During a laser pulse i, the molecule can absorb two photons, can undergo induced emission and can be photobleached. Thus, the set of differential equations describing the behaviour of the molecule during the pulse is:

$$\frac{d}{dt'}\begin{pmatrix} S^i_{0p}(t') \\ S^i_{1p}(t') \end{pmatrix} = \begin{pmatrix} -\delta\,\phi^2(t') & \delta\,\phi^2(t') \\ \delta\,\phi^2(t') & -\delta\,\phi^2(t') - \sigma\,\phi(t') \end{pmatrix} \begin{pmatrix} S^i_{0p}(t') \\ S^i_{1p}(t') \end{pmatrix} \tag{3.6}$$

with the initial conditions:

$$\begin{pmatrix} S^i_{0p}(0) \\ S^i_{1p}(0) \end{pmatrix} = \begin{pmatrix} a^i \\ b^i \end{pmatrix}. \tag{3.7}$$

The additional index p for $S_0(t')$ and $S_1(t')$ denotes that these functions are calculated for t' in $[0\,,\tau_P]$.

The solution of the set 3.6 of differential equations is given by:

$$\begin{pmatrix} S^i_{0p}(t') \\ S^i_{1p}(t') \end{pmatrix} = \begin{pmatrix} g_1(t') & g_2(t') \\ g_2(t') & g_3(t') \end{pmatrix} \begin{pmatrix} a^i \\ b^i \end{pmatrix}. \tag{3.8}$$

The functions $g_1(t')$, $g_2(t')$ and $g_3(t')$ depend on the TPE cross section δ, the excitation flux ϕ_0 and the cross section σ of the transition $S_n \leftarrow S_1$. (Appendix, Eq. 3.24 - 3.27)

The second set of equations describing the transport and photoprocesses during the period τ_0 between two consecutive laser pulses, i.e. the dark period, is given by:

$$\frac{d}{dt'}\begin{pmatrix} S^i_{0d}(t') \\ S^i_{1d}(t') \end{pmatrix} = \begin{pmatrix} -\frac{1}{\tau_D} & k \\ 0 & -k - \frac{1}{\tau_D} \end{pmatrix} \begin{pmatrix} S^i_{0d}(t') \\ S^i_{1d}(t') \end{pmatrix} \tag{3.9}$$

with the initial conditions:

$$\begin{pmatrix} S^i_{0d}(\tau_P) \\ S^i_{1d}(\tau_P) \end{pmatrix} = \begin{pmatrix} c^i \\ d^i \end{pmatrix}. \tag{3.10}$$

The additional index d for $S_0(t')$ and $S_1(t')$ denotes that these functions are calculated during the dark period between two consecutive laser pulses.

By solving the set 3.9 of differential equations, we obtain:

$$\begin{pmatrix} S^i_{0d}(t') \\ S^i_{1d}(t') \end{pmatrix} = \begin{pmatrix} g_4(t') & g_5(t') \\ 0 & g_6(t') \end{pmatrix} \begin{pmatrix} c^i \\ d^i \end{pmatrix} \tag{3.11}$$

where the functions $g_4(t')$, $g_5(t')$ and $g_6(t')$ depend on the mean diffusion time τ_D and on the relaxation rate k. (Appendix, Eq. 3.28 - 3.30)

Since the total excitation is characterised by a periodical *train* of laser pulses, the population of the ground state S_0 and of the first singlet state S_1 are also oscillations. However, the oscillations of $S_0(t')$ and $S_1(t')$ are not purely periodical, but are damped due to photobleaching and diffusion. These processes remove the molecule from the excitation-emission cycle between S_0 and S_1. Consequently, the initial conditions a^i and b^i at the laser pulse i are the results of the diffusion-fluorescence set 3.9 of differential equations of the foregoing dark period $i-1$ at time $t' = \tau_0$. The initial conditions c^i and d^i in the dark period i are the results of the excitation-photobleaching set 3.6 of differential equations of the same pulse i at time $t' = \tau_P$. Thus, the initial conditions $a^i\,, b^i\,, c^i$ and d^i are given by:

$$\begin{pmatrix} a^i \\ b^i \end{pmatrix} = \begin{pmatrix} S_{0p}^{i-1}(\tau_0) \\ S_{1p}^{i-1}(\tau_0) \end{pmatrix} \qquad \text{and} \qquad \begin{pmatrix} c^i \\ d^i \end{pmatrix} = \begin{pmatrix} S_{0p}^{i}(\tau_P) \\ S_{1p}^{i}(\tau_P) \end{pmatrix} . \tag{3.12}$$

Since we observe the fluorescence signal of an individual molecule integrated over the dark interval $[\tau_P\,, \tau_0]$:

$$F^i = S_{1p}^i \int_{\tau_P}^{\tau_0} k_F\, e^{-t'/\tau_F}\, dt' = S_{1p}^i(\tau_P)\, f_0 \tag{3.13}$$

we must determine only $S_{1p}^i(\tau_P) = d^i$ to obtain the dependence of the fluorescence signal on the pulse position, because f_0, the integral in Eq. 3.13, is independent of i.

Considering the expressions, which connect the results attained during two successive cycles containing a laser pulse and the dark period thereafter, we obtain:

$$\begin{pmatrix} c^i \\ d^i \end{pmatrix} = \begin{pmatrix} g_1(\tau_P) & g_2(\tau_P) \\ g_2(\tau_P) & g_3(\tau_P) \end{pmatrix} \begin{pmatrix} g_4(\tau_0) & g_5(\tau_0) \\ 0 & g_6(\tau_0) \end{pmatrix} \begin{pmatrix} c^{i-1} \\ d^{i-1} \end{pmatrix} . \tag{3.14}$$

The index $i = 1$ is assigned to the reference pulse which first interacts with the molecule as it enters the volume V. Moreover, we consider that the molecule is necessarily in the ground state as it diffuses into the volume V. Thus, the initial conditions of the excitation-photobleaching set 3.6 of differential equations are given by:

$$\begin{pmatrix} a^i \\ b^i \end{pmatrix} = \begin{pmatrix} 1 \\ 0 \end{pmatrix} . \tag{3.15}$$

Consequently, combining the equations 3.14 and 3.15 we obtain:

$$\begin{pmatrix} c^i \\ d^i \end{pmatrix} = \begin{pmatrix} g_1(\tau_P) & g_2(\tau_P) \\ g_2(\tau_P) & g_3(\tau_P) \end{pmatrix} \left[\begin{pmatrix} g_4(\tau_0) & g_5(\tau_0) \\ 0 & g_6(\tau_0) \end{pmatrix} \begin{pmatrix} g_1(\tau_P) & g_2(\tau_P) \\ g_2(\tau_P) & g_3(\tau_P) \end{pmatrix} \right]^{i-1} \begin{pmatrix} 1 \\ 0 \end{pmatrix}, \tag{3.16}$$

which gives the probability of occupancy of S_0 and S_1 for each pulse i at the beginning of the dark period.

Since we can consider that the period τ_0 signifies a time unit, the index i is a time dimension and can be expressed by:

$$i = \frac{t}{\tau_0}\,. \tag{3.17}$$

Thus, we can write $c^i = c(t)$ and $d^i = d(t)$, where t is the time variable with the unit τ_0. The probability of occupancy of the first singlet state at the end of the laser pulse is $S_{1p}(t;\tau_P) = d(t)$. Consequently, the most probable time profile of the fluorescence signal of an individual molecule is given by:

$$F(t) = S_{1p}(t;\tau_P)\, f_0\,. \tag{3.18}$$

Note that the fluorescence signal $F(t)$ of a single molecule is not equivalent to the fluctuating fluorescence signal registered in the experiment, since during data acquisition many molecules are monitored. Nevertheless, the molecules are detected one at a time. The signal $F(t)$ restores only the most probable time profile of the experimental fluorescence bursts emitted by single molecules when the background is neglected, i.e. $F(t)$ is an averaged fluorescence signal over a very large number of molecules and thus a statistical quantity.

Since the autocorrelation analysis used in the evaluation of the experimental signal is an integrative method, through which the properties of the individual burst are lost and only the average characteristics of the fluctuations are retained, the assumption that the experimental autocorrelation functions are equivalent is justified. The theoretical autocorrelation function is defined as:

$$G(\tau) = \frac{\langle \delta F(t)\, \delta F(t+\tau) \rangle}{\langle \delta F(t) \rangle^2} \tag{3.19}$$

where $\delta F(t) = F(t) - \langle F(t) \rangle$.

However, this function $G(\tau)$ is defined for the special case of an average number N of one molecule in the excitation volume ($N = 1$) without taking into account the background. When considering the background and an arbitrary N, the simulated autocorrelation function becomes:

$$G_{fit}(\tau) = G(0_+)\, G(\tau) \tag{3.20}$$

where $G(0_+)$ is the amplitude of the autocorrelation function without considering the photobleaching defined as:[22]

$$G(0_+) = \frac{\xi^2}{N} = \frac{[I_F/(I_F + I_B)]^2}{N} \tag{3.21}$$

with I_F the mean fluorescence signal and I_B the mean background signal.[22,23] The term, which restores the influence of photobleaching on the amplitude of the autocorrelation function, is included in the function $G(\tau)$.

By fitting $G_{fit}(\tau)$ to the experimental autocorrelation functions, the diffusion time τ_D, the photobleaching cross section σ and the average number of molecules in the excitation volume N can be determined.

3.4 Experiment

The basic setup used to register the fluorescence signal in single-molecule experiments is similar to that described by Mertz et al.,[22] with the following differences: the laser beam is tenfold extended, and the repetition rate of the Ti:Sa laser (Mira 900, Coherent) is not doubled. The pulse laser beam has 200 fs pulse width and 76 MHz repetition rate. The pulse width at the sample is approximately 300 fs,[24] broadened from 200 fs by group delay dispersion mainly in the objective (BK7).[25] A microscope objective Plan Neofluar (40X, NA = 1.3, oil-immersion, Carl Zeiss) is used to focus the expended laser beam into the sample. The dimensions of the effective two-photon excitation volume calculated as indicated in the former section are $\omega_0 = 334$ nm, $z_e = 1570$ nm and $V \approx 0.74$ fL for an excitation wavelength λ of 800 nm, and $\omega_0 = 351$ nm, $z_e = 1650$ nm and $V \approx 0.85$ fL for an excitation wavelength λ of 840 nm. These values were validated in experiments with fluorescent latex microbeads for the xy resolution and with fluorescein isothiocyanate (FITC) monolayers for the z resolution.[26] The detection unit is an avalanche photodiode (SPCM-AQ-131, EG&G Optoelectornics Canada) with a total detection efficiency of about 2% for C314 ($\lambda_F = 480$ nm) and about 3% for C153 ($\lambda_F = 532$ nm). The signal of the avalanche photodiode is directed to a multichannel scaler (MCD-2E, 7882, FAST ComTec) operated at 10 kHz (100 μs/channel) or 100 kHz (10 μs/channel) depending on the required resolution.

For the single-molecule experiments we used solutions (200 pmol/L) of C153 and C314 (Radiant Dyes) in glycol p.a. (dynamic viscosity $\eta = 16.1 \cdot 10^{-3}$ Pa$\cdot$s).

For measurements of TPE cross section and fluorescence lifetime 100 nmol/L solutions of C153 and C314 were used.

3.5 Results and Discussion

3.5.1 Fluorescence Signals of C153 and C314

The TPE cross sections δ and fluorescence lifetimes τ_F of C153 and C314 were determined to completely characterise their fluorescence. The TPE cross section δ of C153 in ethanol at $\lambda = 800\,\text{nm}$ is $47.4 \pm 0.8\,\text{GM}$ ($1\,\text{GM} = 10^{-50}\,\text{cm}^4\,\text{s}\,\text{photon}^{-2}$), and that of C314 in ethanol at $\lambda = 840\,\text{GM}$ is $16.4 \pm 0.5\,\text{GM}$. Coumarin 1 was used as reference for measuring the relative TPE cross section.[27] The main error sources in these measurements were fluctuations of the laser power ($\pm 0.1\,\text{mW}$) and imprecisions in the dilution of the solutions and in the determination of the total detection efficiency ($\pm 0.1\%$). The resulting values are similar to the deviations determined experimentally.

The fluorescence lifetime of C153 and C314 in glycol were determined with the same set-up described before, except that the avalanche photodiode was replaced by an ICCD camera (PicoStar, LaVision) with a gate width of 200 ps. The fluorescence lifetime τ_F is $3.1 \pm 0.1\,\text{ns}$ for C153 and $3.4 \pm 0.1\,\text{ns}$ for C314. These results agree with previously measured fluorescence lifetimes of C153 and C314.[19,28]

With our kinetic rate model the optimal laser parameters, e.g. pulse width, can be determined for any TPE set-up and for any molecule with low ISC rate. In the following, we show the applicability of this model by comparing the simulated data with our experimental data.

In the two-photon fluorescence microscopy we expect the fluorescence signal to scale quadratically with the excitation flux ϕ. However, it is known that at high laser fluxes in the excitation volume this relation is no longer valid due to the increased influence of the induced emission. The excitation flux at which the fluorescence signal reaches the maximum value is denoted as saturation flux. The excitation flux ϕ_0 during the pulse is directly proportional to the mean laser power at the sample over space and time.

$$\langle P \rangle = \phi_0 \frac{\tau_P}{\tau_0} \pi \omega_0^2 \tag{3.22}$$

Thus, under identical experimental conditions, i.e. the same laser characteristics τ_P and τ_0 and the same excitation volume, the dependence of the fluorescence

signal on the flux ϕ can be deduced from the dependence of the fluorescence signal on the mean power $\langle P \rangle$.

Experiments performed with 100 nmol L^{-1} solutions of C153 and C314 show that for mean excitation powers $\langle P \rangle$ of less than 80 mW, the quadratic dependence of the total fluorescence signal F on the laser power is validated (the slope recovered from the double-logarithmic plot $F(\langle P \rangle)$ is 1.95 ± 0.05 for C153 and 2.03 ± 0.03 for C314). Consequently, the saturation effect is negligible at powers of less than 80 mW (data not shown).

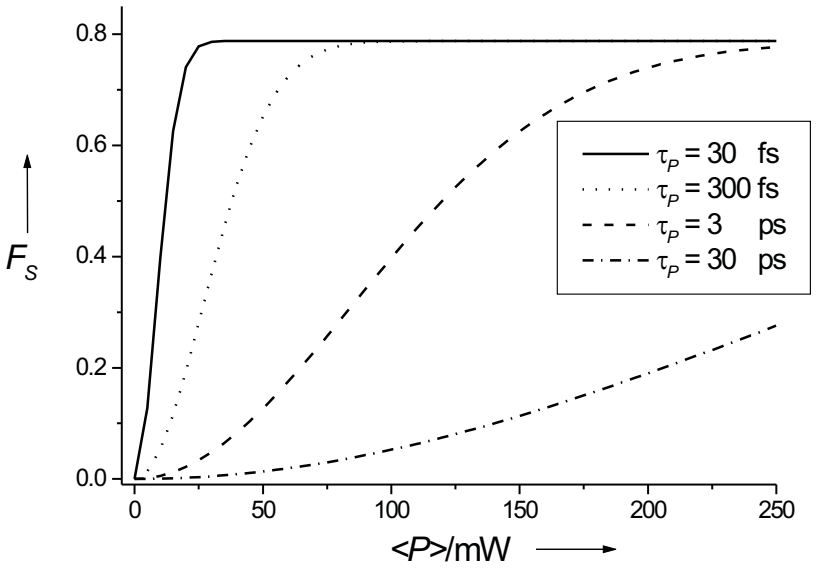

Fig. 3-2: The fluorescence signal F_S emitted by a single C153 molecule during the period $\tau_0 + \tau_P$ as a function of the mean laser power $\langle P \rangle$ at the sample. Parameter employed in the kinetic rate model: $\delta = 47.4$ GM, $\tau_F = 3.1$ ns, $\tau_0 = 13$ ns, $\omega_0 = 334$ nm, $\sigma = 1.7 \cdot 10^{-23}$ cm^{-23}. The considered pulse width τ_P: 30 fs, 300 fs, 3 ps, 30 ps. (simulated data)

Employing our kinetic rate model, we simulated the dependence of the fluorescence signal F_S emitted by a single molecule during the period τ_0 on the mean laser power $\langle P \rangle$ (Fig. 3-2).

The fluorescence signal F_S integrated over the period τ_0 was calculated from Eq. 3.13. The probability of occupancy $S_1(\tau_P)$ is the solution of the set 3.6 of differential equations, for which the initial conditions are those for $i = 1$. In this case the long-term effects of diffusion and photobleaching are neglected, as is appropriate for measurements at high concentrations.

The mathematical expression of F_S is given by:

$$F_S = g_2(t')\, f_0(\tau_P, \tau_0, k)\,. \tag{3.23}$$

In this way, maximum-saturation mean powers at $\partial F_S/\partial\langle P\rangle = 0$ of 134 mW for C153 and of 226 mW for C314 were obtained for a pulse width of 300 fs. A deviation from the linearity in the double-logarithmic plot $\lg(F_S)$ versus $\lg(\langle P\rangle)$ is already observed at about 50% of the maximum-saturation mean laser power. These results were verified by the experiment.

The dependence of the fluorescence signal F_S on $\langle P\rangle$ deduced from the kinetic rate model is equivalent to the experimentally determined dependence of the total fluorescence signal F on $\langle P\rangle$, because both the signal F_S of the individual molecule and the total signal F stemming from a large group of molecules are not influenced by long-term effects of diffusion and individual photobleaching.

An important parameter, which influences the dependence of the fluorescence signal F_S on the mean excitation power $\langle P\rangle$, is the pulse width τ_P. As shown in Fig. 3-2, the maximum saturation level is reached at a lower mean laser power for a shorter pulse. Thus, we can conclude that ultrashort pulsed excitation is favourable in single-molecule experiments in which low mean laser powers at the sample are required, since the fluorescence signal already reaches the maximum value at such low powers. On the other hand, at mean powers $\langle P\rangle$ above 50 mW a decrease in the pulse width from 300 to 30 fs or even less will not influence the fluorescence signal. Thus, any efforts to reduce the pulse width are unnecessary.

The count rate at the detector originating from the emission of the individual molecule at a mean laser power $\langle P\rangle$ of 40 mW is on average 32 kHz for C153 and 29 kHz for C314. The background count rate of glycol, including a dark count rate of 200 Hz, amounts to 600 Hz under the same conditions. Thus, an average burst is detected with a signal-to-background ratio (SBR)[22] of about 53 for C153 and about 48 for C314 at $\langle P\rangle = 40$ mW. The rather low mean SBR[23] is acceptable considering that neither C153 nor C314 was excited at its absorption maximum and the experiments are performed under non-saturation conditions.

3.5.2 Autocorrelation Analysis

In this section we verify the applicability of the developed kinetic rate model to single-molecule FCS by approximating experimental fluorescence autocorrelation functions with the simulated function $G_{fit}(\tau)$.

The processes, which in our case influence the time profile of the autocorrelation function $G(\tau)$ of the fluorescence signal $F(t)$, are photobleaching and diffusion. Photobleaching is quantified by the photobleaching rate q_{Pb}, which is $\sigma\,\phi_0$ during the laser pulse and zero during the dark period between consecutive pulses. Since the cross section σ of the transition $S_n \leftarrow S_1$ (photobleaching cross section) is a molecular constant, the only parameter, which can lead to variations in the photobleaching rate during the laser pulse, is the excitation flux ϕ_0. Indirectly, photobleaching is also influenced by the pulse width τ_P and by the laser repetition rate $1/\tau_0$. These aspects will not be discussed inhere.

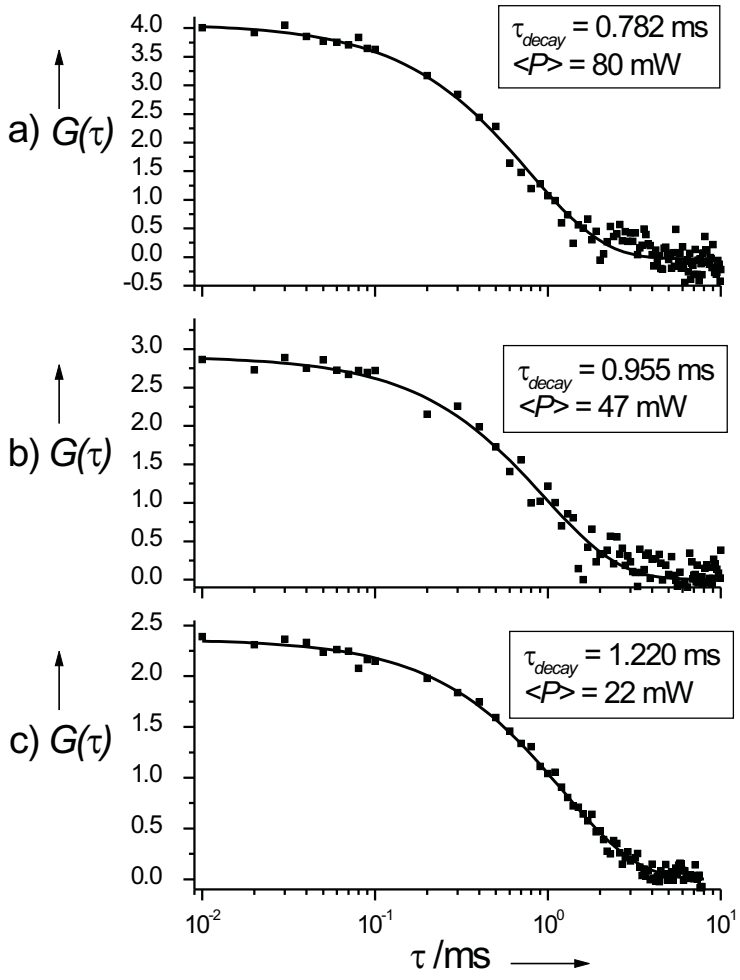

Fig. 3-3: Autocorrelation functions of the fluorescence signal of single C153 molecules measured at a) 80 mW, $\xi = 0.5$, b) 47 mW, $\xi = 0.48$ and c) 22 mW, $\xi = 0.52$. Parameters deployed in the kinetic rate model: $\delta = 47.4$ GM, $\tau_F = 3.1$ ns, $\tau_0 = 13$ ns, $\tau_P = 300$ ps, $\omega_0 = 334$ nm. Resulting parameters: $N = 0.115$, $\sigma = 1.7 \cdot 10^{-23}$ cm^2 and $\tau_D = 1.25$ ms. (experimental data fitted by the simulated function $G_{fit}(\tau)$)

Since for given pulse width τ_P and repetition rate $1/\tau_0$ the excitation flux is proportional to the mean laser power $\langle P \rangle$ at the sample, we can investigate the effect of photobleaching on the autocorrelation function by analysing the time profile of the autocorrelation function at different mean laser powers $\langle P \rangle$ (Fig. 3-3). The time profile of the autocorrelation function is characterised by the amplitude A and by the decay time τ_{decay}. The decay time τ_{decay} is defined as the time until the autocorrelation function decreases to $1/e$ of its initial value A. This period is roughly equivalent to the mean dwell time of the molecule in the volume V, which is affected by both photobleaching and diffusion.

The decay time of the experimental autocorrelation curves of a 200 pmol L^{-1} solution of C153 (Fig. 3-3) measured at 22, 32, 40, 47, 55 and 80 mW decreases with increasing mean laser power $\langle P \rangle$, while under the same conditions the amplitude tends to increase. This indicates that photobleaching plays an important role in the power range $20 - 80$ mW. However, neither the decay time nor the amplitude of the autocorelation functions offers the possibility of a quantitative distinction between the effects of diffusion and photoblaching. Nevertheless, if the theoretical function $G_{fit}(\tau)$ is fitted to the experimental autocorrelation curves, we can determine the photobleaching cross section ($\sigma = 1.7 \cdot 10^{-23}$ cm^2 for C153) and the mean diffusion time ($\tau_D = 1.25$ ms for C153). From the amplitude of the autocorrelation functions we also obtained the average number of molecules in the volume V ($N = 0.115$). This value agrees with the value of $N_C = 0.088$ calculated from the bulk concentration C of the solution as $N_C = C \cdot N_A \cdot V$. N_A is the Avogadro number.

For $N = 0.115$ it is implausible that more than one molecule resides at a time inside the excitation volume, since the probability $P_2 = 5.6 \cdot 10^{-3}$ of finding two molecules in V as compared to the probability $P_1 = 0.1$ of finding only one molecule in V is rather low. For calculating these probabilities, we assumed that random motion of the molecules through the excitation volume is governed by Poissonian statistics. In any case, we can be sure that basically only one molecule is detected at a time.

Using our kinetic rate model, we can determine the dependence of the decay time τ_{decay} and of the amplitude A on the mean laser power $\langle P \rangle$ (Fig. 3-4). Thus, we can delimit the power range, in which diffusion predominates, from the region, in which both diffusion and photobleaching contribute to the time profile of the autocorrelation function.

In the case of C153, the dependence of the decay time τ_{decay} on the mean

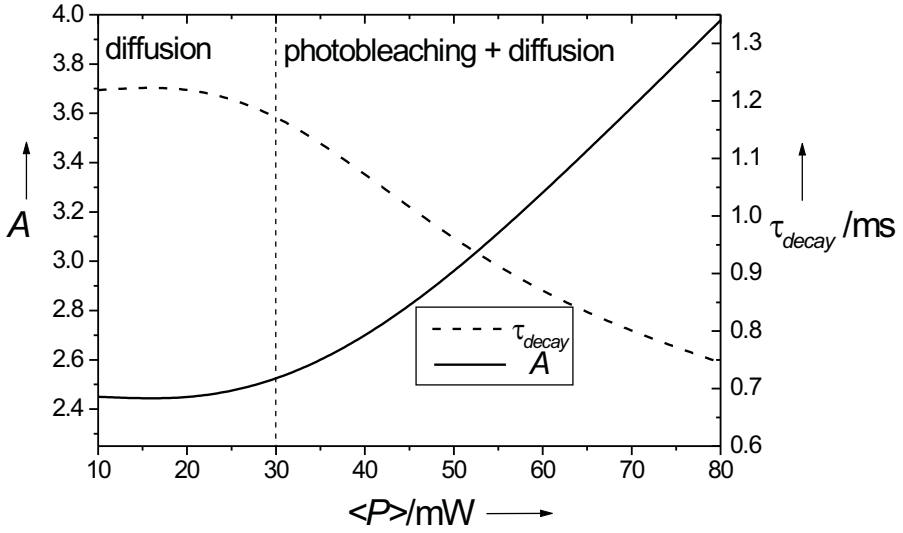

Fig. 3-4: Dependence of the decay time τ_{decay} and of the amplitude A of the autocorrelation function on the mean laser power $\langle P \rangle$. Employed parameters: $\delta = 47.4$ GM, $\tau_F = 3.1$ ns, $\tau_0 = 13$ ns, $\tau_P = 300$ ps, $\omega_0 = 334$ nm, $N = 0.115$, $\sigma = 1.7 \cdot 10^{-23}$ cm^2, $\tau_D = 1.25$ ms, $\xi = 0.5$. (results of the approximation of the experimental data with $G_{fit}(\tau)$)

excitation power $\langle P \rangle$ indicates that photobleaching plays an essential part in modelling the time profile of the autocorrelation function at laser powers $\langle P \rangle$ higher than about 30 mW, but this effect vanishes for $\langle P \rangle$ lower than 30 mW.

Experimentally it has been observed that photobleaching not only influences the time profile, but also the amplitude A of the autocorrelation function, i.e. the amplitude of the autocorrelation function increases with increasing excitation power.[16] In our theoretical model, the amplitude A of the autocorrelation function $G_{fit}(\tau)$ depends on N and ξ and additionally on the photobleaching parameters. Thus, N is the mean number of molecules *present* in the excitation volume and not just the mean number of *fluorescing* molecules and can be directly compared to N_C. The increase in the amplitude of the autocorrelation function with increasing mean excitation power $\langle P \rangle$ in the range $30 - 80$ mW (Fig. 3-4) indicates once more that photobleaching plays a significant role in our experiment for $\langle P \rangle$ higher than about 30 mW. For $\langle P \rangle$ lower than 30 mW the amplitude of the autocorrelation function remains essentially constant, as expected.

The dependence of the decay time τ_{decay} and the amplitude A of the fluorescence autocorrelation functions on the excitation power $\langle P \rangle$ that results from

our measurements is similar to well-known FCS results determined under the assumption of cw illumination.[9–17] In this way the correctness of our experiments and of the developed model is guaranteed. The main difference between our model and the well-known cw models, i.e. the consideration of pulsed excitation, pulsed photobleaching and pulsed induced emission, is mirrored quantitatively in different photobleaching cross sections. With our model a photobleaching cross section σ of $\approx 10^{-23}$ cm^2 was determined, while a cw model gave a value of $\approx 10^{-17}$ cm^2 for the same parameter. Moreover, the good agreement between the experimental data of C153 and the simulated autocorrelation function $G_{fit}(\tau)$ at different excitation powers indicates unequivocally that the photobleaching rate q_{Pb} corresponding to the photobleaching pathway through S_n scales linearly with the excitation flux, and thus that the ground-state depletion rate scales cubically with the excitation flux. An approximation of the same experimental data with the autocorrelation function obtained from a kinetic rate model, in which the photobleaching rate q_{Pb} is considered to be independent of the excitation flux, leads to discrepancies between the simulation and the experiment.

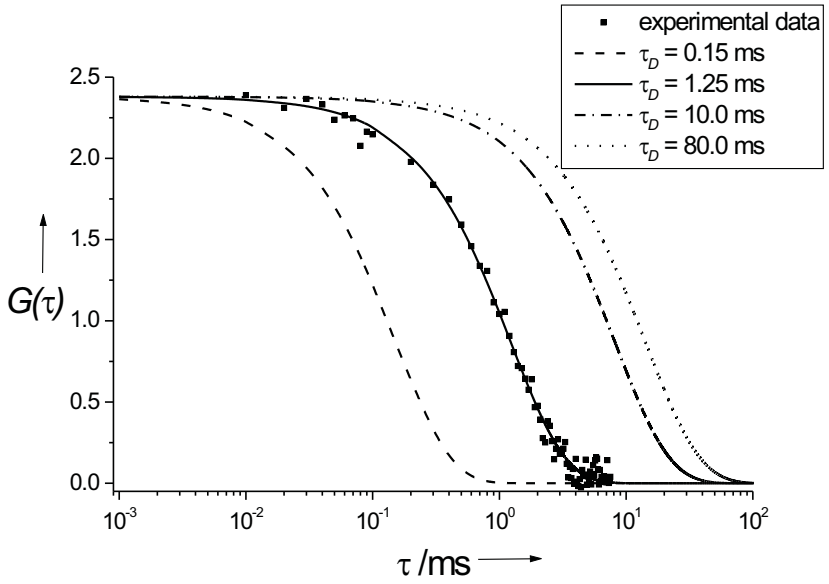

Fig. 3-5: Simulated autocorrelation functions of C153 at different diffusion times. Employed parameters: $\delta = 47.4$ GM, $\tau_F = 3.1$ ns, $\tau_0 = 13$ ns, $\tau_P = 300$ ps, $\langle P \rangle = 22$ mW, $\omega_0 = 334$ nm, $N = 0.115$, $\sigma = 1.7 \cdot 10^{-23}$ cm^2, $\xi = 0.52$.

Until now, we have primarily commented on the influence of photobleaching and only tangentially on the effect of diffusion on the autocorrelation function. The effect of diffusion on the fluorescence signal of individual molecules is anal-

ysed by studying the impact of the mean diffusion time τ_D of a single C153 molecule through the volume V on the time profile of the autocorrelation function (Fig. 3-5). As expected, the amplitude A of the autocorrelation function does not vary with the mean diffusion time τ_D, while the dwell time τ_{decay} of a molecule in the excitation volume does. This behaviour is shown in Fig. 3-6.

For short diffusion times, the dwell time τ_{decay} exhibits a linear dependence on τ_D, i.e. τ_{decay} basically represents the diffusion time. With increasing diffusion time this dependence deviates from linearity, and for large diffusion times (at $\langle P \rangle = 80$ mW, ca. 10 ms), the decay time barely varies with τ_D. The dwell time τ_{decay} in this range roughly corresponds to the photobleaching time. Thus, at each excitation power $\langle P \rangle$, we are able to delimit the τ_D-ranges in which only diffusion, only photobleaching or both processes influence the time profile of the autocorrelation function, as shown for $\langle P \rangle = 80$ mW in Fig. 3-6. Moreover, for diffusion times of about 1 ms and at excitation powers up to 80 mW, as in our experiment, photobleaching will not be predominant. This will only occur at higher laser powers or at longer diffusion times.

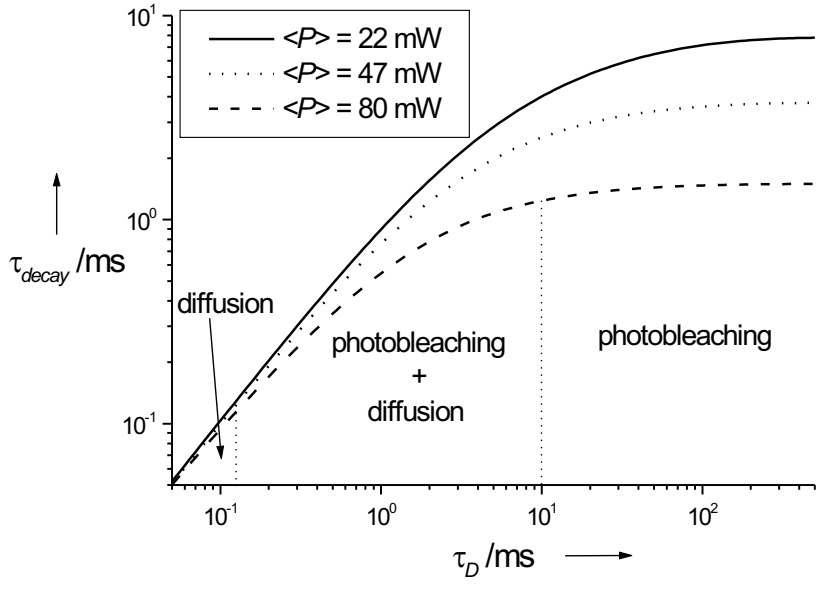

Fig. 3-6: Dependence of the decay time τ_{decay} (dwell time of a C153 molecule in the volume V) on the mean diffusion time τ_D at different mean excitation powers. The dwell time at large τ_D (the photobleaching time) depends on the excitation power and is 7.806 ms at $\langle P \rangle = 22$ mW, 3.733 ms at $\langle P \rangle = 47$ mW and 1.495 ms at $\langle P \rangle = 80$ mW. (simulated data)

Note that the diffusion time τ_D and the mean laser power $\langle P \rangle$ are two differ-

ent parameters and, thus, Fig. 3-4 and 3-6 display two different effects on the autocorrelation function.

The influence of diffusion, i.e. diffusion time τ_D, on the fluorescence autocorrelation functions, i.e. on the decay time τ_{decay} and on the amplitude A, as shown in Fig. 3-5 and Fig. 3-6, agrees with FCS experiments and FCS simulations performed by means of cw models.[9–17,22] This is a further verification of the correctness of our pulsed-illumination model.

By approximating the experimental autocorrelation curves of the fluorescence signal of a 200 pmol L^{-1} solution of C314 with the simulated function $G_{fit}(\tau)$, we determined $N = 0.119$, $\sigma = 5 \cdot 10^{-23}$ cm^2 and $\tau_D = 1.39$ ms ($\xi \approx 0.5$). Also in this case $N = 0.119$ agrees with $N_C = 0.102$.

	C153	**C314**
σ [cm^2]	$1.7 \cdot 10^{-23}$ (at 800 nm)	$5.0 \cdot 10^{-23}$ (at 840 nm)
δ [GM]	47.4 ± 0.8 (at 800 nm)	16.4 ± 0.5 (at 840 nm)
τ_F [ns]	3.1 ± 0.1	3.3 ± 0.1
τ_F^{lit} [ns]	3.4	3.316 ± 0.196
τ_D [ms]	1.25	1.39
D [cm^2 s^{-1}]	$1.66 \cdot 10^{-6}$	$1.64 \cdot 10^{-6}$
D^* [cm^2 s^{-1}]	$1.36 \cdot 10^{-6}$	$1.36 \cdot 10^{-6}$

Tab. 3-1: Summary of the determined molecular parameters of C153 and C314: σ - photobleaching constant, δ - two-photon absorption cross-section, τ_F - fluorescence lifetime, τ_D - mean diffusion time and D - diffusion coefficient. The fluorescence lifetime τ_F^{lit} of C153 was measured in ethanol.[19] For C153 in DMF an absorption cross section of $\delta = 47 \pm 2$ GM is given in ref. [24]. The deviation between the local diffusion coefficient D determined from the time profile of the autocorrelation function and the diffusion coefficient D^* calculated by using the Stokes-Einstein relation is acceptable, since the requirement of the Stokes-Einstein relation for molecules to be spherical is not sufficiently fulfilled by the studied coumarins. To our knowledge the photobleaching cross sections σ of C153 and C314 at 800 and 840 nm were not known up to now.

The photostability is an important factor in choosing appropriate dyes for

single-molecule detection and spectroscopy. The photobleaching yield φ_{Pb} and the ground-state depletion rate q_0 are usually employed as indicators for the photostability of substances investigated by single-molecule FCS. However, in the case of two-photon excitation the main disadvantage of these indicators is their dependence on the excitation intensity and on the type of illumination and, thus, they are usually specific for each experiment.

The photobleaching yield φ_{Pb} (Appendix, Eq. 3.31) is $2 \cdot 10^{-3}$ for C153 and $2.2 \cdot 10^{-3}$ for C314 at $\langle P \rangle = 22$ mW.

The ground-state depletion rate q_0 (Appendix, Eq, 3.32 - 3.33) is 0.213 ms^{-1} for C153 and 0.285 ms^{-1} for C314 at $\langle P \rangle = 80$ mW and is significantly lower than the ground-state depletion rate determined for tetramethyl rhodamine (TMR) $q_0 = 49$ ms^{-1} at saturation.[16] Note that the photobleaching rate of TMR was determined by using a theoretical approach assuming two-photon cw excitation for the simulation of the autocorrelation functions.

3.6 Conclusions

This work presents a theoretical approach for the simulation of the autocorrelation functions acquired in two-photon excitation single-molecule FCS experiments. The main novel feature of this model is the consideration of the pulsed illumination and of its effect on the photobleaching rate, on the excitation rate and on the rate of induced emission. Moreover, this theoretical approach opens the possibility to rigorously investigate the effect of the laser characteristics, like pulse width and repetition rate, on the fluorescence autocorrelation function. The main simplification is the assumption of rectangular profiles with respect to the laser flux, both spatially and temporally. It is easy to extend the model for any laser pulse profile and also for dyes with considerable ISC rates. However, in this case a simple analytical solution is not possible. Moreover, according to our results such an extension of the theoretical model is also not necessary.

In order to prove the accuracy of our model we have performed an approximation of experimental results with the simulated autocorrelation functions. The good agreement between the parameters determined from the autocorrelation function and those determined by other means validates the model. Furthermore, we have determined the molecular specific photobleaching cross-section σ for both C153 and C314, which indicate the photostability of these dyes independently of the experimental conditions. A comparison of the ground state

depletion rate of the studied dyes with that of TMR indicates that C153 and C314 are very suitable for single molecule FCS due to their increased photostability by two-photon excitation. The essential experimental results are summarised in Tab. 3-1.

Appendix

The expressions of the functions $g_1(t')$, $g_2(t')$ and $g_3(t')$ used for the calculation of the probability of occupancy of the first singlet state S_1 immediately after the laser pulse are given by:

$$\Sigma = \sqrt{4\,\delta^2\,\phi_0^2 + \sigma^2} \tag{3.24}$$

$$g_1(t') = \frac{e^{-\frac{1}{2}\,\phi_0\,t'\,(2\,\phi_0\,\delta+\sigma+\Sigma)}}{2\,\Sigma}\left[\left(-1+e^{\phi_0\,t'\,\Sigma}\right)\sigma+\left(1+e^{\phi_0\,t'\,\Sigma}\right)\Sigma\right] \tag{3.25}$$

$$g_2(t') = \frac{e^{-\frac{1}{2}\,\phi_0\,t'\,(2\,\phi_0\,\delta+\sigma+\Sigma)}\left(-1+e^{\phi_0\,t'\,\Sigma}\right)\sigma\,\phi_0}{2\,\Sigma} \tag{3.26}$$

$$g_3(t') = \frac{e^{-\frac{1}{2}\,\phi_0\,t'\,(2\,\phi_0\,\delta+\sigma+\Sigma)}}{2\,\Sigma}\left[\left(1-e^{\phi_0\,t'\,\Sigma}\right)\sigma+\left(1+e^{\phi_0\,t'\,\Sigma}\right)\Sigma\right] \tag{3.27}$$

The expressions of the functions $g_4(t')$, $g_5(t')$ and $g_6(t')$ used to calculate the probability of occupancy of the first singlet state S_1 after the dark period are given by:

$$g_4(t') = e^{-t'/\tau_D} \tag{3.28}$$

$$g_5(t') = \left(e^{-k\,t'}-1\right)g_6(t') \tag{3.29}$$

$$g_6(t') = e^{-(k+1/\tau_D)t'} \tag{3.30}$$

The photobleaching yield is defined as:

$$\varphi_{Pb} = \frac{\text{no. of photobleached molecules}}{\text{total no. of laser pulses}} = \frac{\sigma\,\phi_0\sum_{i=0}^{\tau_{decay}/\tau_0} S_{1p}^{i}(\tau_P,\phi_0)}{\tau_{decay}/\tau_0} \tag{3.31}$$

We considered that only one molecule dwells in the excitation volume at a time and, thus, only one molecule can be excited once during a laser pulse.

The ground-state depletion rate is defined as:

$$q_0 = \frac{1}{\tau_P}\int_0^{\tau_P}\frac{dS_n(t')}{dt'} = \frac{1}{\tau_P}\int_0^{\tau_P}\sigma\,\phi_0\,S_{1p}^1(t')dt' \tag{3.32}$$

where S_{1p}^1 is the probability of occupancy of the first singlet state during the first pulse $i = 1$ and was determined by solving the set 3.6 of differential equations.

$$S_{1p}^1(t') = g_2(t') \tag{3.33}$$

The initial conditions for the set 3.6 of equations in this case are $a^1 = 1$ and $b^1 = 0$.

References

[1] W.P. Ambrose, P.M. Goodwin, J.H. Jett, A. Van Orden, J.H. Werner, R.A. Keller, *Chem. Rev.* **1999**, 99, 2929-2956

[2] S. Nie, R.N. Zare, *Annu. Rev. Biophys. Biomol. Struct.* **1997**, 26, 567-596

[3] A.A. Deniz, T. Laurence, M. Dahan, D.S. Chelma, P.G. Schultz, S. Weiss, *Annu. Rev. Phys. Chem.* **2001**, 52, 233-253

[4] W.E. Moerner, M. Orrit, *Science* **1999**, 283, 1670-1676

[5] a) H. Qian, E.S. Elson in Fluorescence Correlation Spectroscopy - Theory and Applications (Eds: R. Rigler, E.S. Elson), Springer, Berlin, 2000, pp. 65-82; b) W.W. Webb in Fluorescence Correlation Spectroscopy - Theory and Applications (Eds: R. Rigler, E.S. Elson), Springer, Berlin, **2000**, pp. 305-328

[6] S.R. Aragon, R. Pecora, *J. Chem. Phys.* **1976**, 64, 1791-1803

[7] T. Wohland, R. Rigler, H. Vogel, *Biophys. J.* **2001**, 80, 2987-2999

[8] a) R. Rigler, L. Edman, Z. Foeldes-Papp, S. Wennmalm in Single molecule Spectroscopy, Nobel Conference Lectures, (Eds: R. Rigler, M. Orrit, T. Basch), Springer, Berlin, **2001**, pp. 177-195; b) T. Wohland, K. Friedrich-Benet, H. Pick, A. Preuss, R. Hovius, H. Vogel in Single molecule Spectroscopy, Nobel Conference Lectures, (Eds: R. Rigler, M. Orrit, T. Basche), Springer, Berlin, **2001**, pp. 195-211

[9] J. Widengren, U. Mets, R. Rigler, *J. Phys. Chem.* **1995**, 99, 13368-13379

[10] J. Widegren, J. Dapprich, R. Rigler, *Chem. Phys.* **1996**, 216, 417-426

[11] J. Widengren, R. Rigler, *Bioimaging* **1996**, 4, 149-157

[12] A. Molski, J. Hofkens, T. Gensch, N. Boens, F. De Schryver, *Chem. Phys. Lett.* **2000**, 318, 325-332

[13] A. Molski, *J. Chem. Phys.* **2001**, 114, 1142-1147

[14] C. Eggeling, J. Widengren, R. Rigler, C.A.M. Seidel, *Anal. Chem.* **1998**, 70, 2651-2659

[15] P. Schwille, U. Haupts, S. Maiti, W.W. Webb, *Biophys. J.* **1999**, 77, 2251-2265

[16] P.S. Dittrich, P. Schwille, *Appl. Phys. B* **2001**, 73, 829-837

[17] J. Mertz, *Eur. Phys. J. D* **1998**, 3, 53-66

[18] K.I. Priyadarsini, D.B. Naik, P.N. Moorthy, *J. Photochem. Photobiol. A* **1989**, 46, 239-246

[19] G. Jones II, W.R. Jackson, C. Choi, *J. Phys. Chem.* **1985**, 89, 295

[20] The intersystem crossing rate k_{ISC} increases with decreasing energy gap ΔE between S_1 and T_1. ΔE between S_1 and T_1 is for rhodamines 0.14 eV[14] and for C153 0.86 eV[18]. k_{ISC} is for rhodamines $\approx 10^6\,\mathrm{s}^{-1}$ and for the studied coumarins $\approx 10^2\,\mathrm{s}^{-1}$. To the low ISC rate of C153 and C314 contributes also the high rigidity of these molecules.[18], M.S.A. Abdel-Mottaleb, M.S. Antonious, M.M. Abo-Aly, L.F.M. Ismaiel, B.A. El-Sayed, A.M.K. Sherief, *J. Photochem. Photobiol. A* **1989**, 50, 259-273

[21] G.H. Patterson, D.W. Piston, *Biophys. J.* **2000**, 78, 2159-2162

[22] Mertz, J.; Xu, C.; Webb, W.W., *Opt. Lett.* **1995**, 20, 2532-2534

[23] L. Brand, C. Eggeling, C. Zander, K.H. Drexhage, C.A.M. Seidel, *J. Phys. Chem. A* **1997**, 101, 4313-4321

[24] G.D. Reid, K. Wynne in Encyclopedia of Analitical Chemistry (Ed: R.A. Meyers), John Wiley & Sons Ltd, Chichester, **2000**, pp. 13644-13670

[25] R. Wolleschensky, T. Feurer, R. Sauerbrey, U. Simon, *Appl. Phys. B* **1997**, 67, 87-94

[26] A. Schönle, M. Glatz, S.W. Hell, *Appl. Opt.* **2000**, 39, 6306-6311

[27] A. Fischer, C. Cremer, H.Z. Stelzer, *Appl. Opt.* **1995**, 34, 1989-2003

[28] D.S. Elson, J. Siegel, S.E.D. Webb, S. Leveque-Fort, M.J. Lever, P.M.W. French, K. Lauritsen, M. Wahl, R. Erdmann, *Opt. Lett.* **2002**, 27, 1409-1411

Chapter 4

Quantitative Determination of the Single Molecule Detection Regime in Fluorescence Fluctuation Microscopy by means of Photon Counting Histogram Analysis

4.1 Abstract

Fluorescence fluctuation experiments are performed in single-molecule detection regime if the fluorescence of at most one molecule is registered at a time. Although the significance of such experiments for investigations of complex non-ergodic systems like those met in the biosciences has been stressed out by many scientists, the quantitative and accurate determination of the single-molecule detection regime received rather little attention. In this work we present a method based on the photon counting histogram (PCH) analysis, which enables the determination of the average number $\overline{N}$ of molecules within the observation volume, for which only the fluorescence of individual molecules is detected at a time. Thus, the accurate design of fluorescence fluctuation experiments performed in single-molecule detection regime is possible.

Demonstrative fluorescence fluctuation experiments based on two-photon excitation are performed on diluted solutions of coumarin 153, in order to verify the potential of the PCH analysis in experiments on the single-molecule detection level. If the mean number $\overline{N}$ of molecules within the excitation volume is larger than 0.048, then the probability to simultaneously detect the fluorescence of two

or more molecules is no longer negligible, i.e. no single-molecule detection regime. If the mean number $\overline{N}$ of molecules is lower than 0.0057, the detection limit of the method is reached, i.e. the fluorescence signal cannot be distinguished from the background. Consequently, the concentration of coumarin 153 characteristic for single-molecule detection regime lies in the range 13 to 110 pmol L^{-1} for the given experimental conditions. We also investigate the influence of the molecular brightness, i.e. molecular and experimental parameters, on $\overline{N}$ characteristic for the single-molecule detection regime.

4.2 Introduction

The development of fluorescence fluctuation spectroscopy (FFS) techniques based on far-field microscopy is of major interest for the biosciences because they enable new insight in complex biological systems at ambient temperature.[1–7] In these techniques, the fluctuating fluorescence signal of single molecules or of ensembles of few molecules is registered and evaluated in order to obtain the molecular parameter of interest. Contrary to bulk experiments, in which only the statistical average of the property of interest is obtained, the FFS measurements yield a distribution of the investigated parameters, which contains more information than the average alone.[8] If the investigated system is ergodic, one obtains the same averaged parameter in bulk measurements, in FFS experiments on ensembles of few molecules as well as in FFS experiments on single molecules.[8] If the system under study is non-ergodic, the averaged parameters obtained in these experiments differ, because certain processes on the molecular level can be monitored only if single molecules are observed one at a time, i.e. FFS experiments in single-molecule detection regime.[8] In the biosciences such non-ergodic systems are rather often, due to the heterogeneous environment and to the complex structure of biomolecules.[9–12] For instance, in fluorescence correlation spectroscopy (FCS) experiments, in which the conformational fluctuations of the DNA fragments are monitored, the authors stress out that since the system under study is non-ergodic, the relaxation rates of the heterogeneous distributed subfractions of DNA fragments can be correctly determined only if single DNA fragments are observed at a time.[13] Thus, they express their concern about the possibility of monitoring the fluorescence of two molecules at the same time.[13]

The theoretical models employed in FFS techniques, e.g. simulation approaches of the autocorrelation function in FCS, are single-particle models, i.e.

models, in which the fluorescence signal of a single molecule is determined. Thus, the results of these approaches describe the statistics of individual molecules.[8,14] In experiments on ergodic systems, the hypothetical single-particle model well represents the dynamics of both the ensemble of molecules as well as of single molecules. In non-ergodic systems, this assumption is no longer true. Only the data registered in experiments, which are performed in the single-molecule detection regime, can be directly compared with the results of the theoretical single-particle approaches.[8]

Concluding, single-molecule FFS techniques are of particular significance for the biosciences. However, the quantitative determination of the single-molecule detection regime received little attention until now. Rigorously, FFS experiments are performed in single-molecule detection regime, if all the measurement time only the fluorescence of individual molecules is detected, i.e. if the maximal number N_{max} of molecules, the fluorescence of which simultaneously contributes to the detected signal, is one. Thus, the parameter, which directly determines the single-molecule detection regime, is N_{max}. Since N_{max} is hardly accessible experimentally, the average number $\overline{N}$ of molecules within the observation volume, for which $N_{max} = 1$, is used as an indicator of the single-molecule detection regime. To our knowledge no quantitative determination of $\overline{N}$ at the single-molecule detection regime has been performed in FFS yet. In the following, we are looking for the appropriate technique for such an investigation, i.e. a theoretical FFS approach in which both N_{max} and $\overline{N}$ explicitly appear as parameters.

The FFS techniques are based either on the analysis of the fluorescence fluctuation dynamics, e.g. the fluorescence correlation spectroscopy (FCS), or on the analysis of the fluorescence fluctuation amplitudes at the equilibrium, e.g. moment analysis of fluorescence intensity distribution (MAFID), photon counting histogram (PCH) analysis or fluorescence intensity distribution analysis (FIDA). These techniques employ both one-photon as well as two-photon excitation. However, the two-photon microscopy has major advantages over the confocal one-photon microscopy in biological investigations, namely the intrinsic $3D$-resolution, low photodamage of the sample outside the focal plane and large penetration depth.[15–17]

The fluorescence correlation spectroscopy is a technique based on the statistical time-dependent analysis of the fluctuating fluorescence signal originating from molecules, which move through the observation volume of the microscope. In first FCS experiments translational diffusion coefficients and rates of chem-

ical reactions have been obtained from the autocorrelation function of the fluorescence signal.[18] The further development of this technique made also possible the investigation of photobleaching, rotational diffusion, antibunching and triplet state kinetics.[1,2,9,19–21] Generally, FCS applications have been performed both at high fluorophore concentrations as well as in single-molecule detection regime.[2,12,19] FCS experiments in single-molecule detection regime are necessary to elucidate relevant biological processes, e.g. the conformational fluctuations of DNA molecules or modifications of the enzymatical activity in heterogeneous environment.[13]

The theoretical fluorescence autocorrelation function explicitly depends only on parameters, which describe the molecular dynamics or photodynamics, e.g. diffusion coefficient, photobleaching rate, intersystem crossing rate, and on the average number $\overline{N}$ of molecules, which dwell within the observation volume. The maximal number N_{max} of molecules, the fluorescence of which simultaneously contributes to the detected signal, does not explicitly influence the shape of the autocorrelation function.

While the analysis of the fluorescence fluctuation dynamics is largely employed in chemistry, biochemistry and in biosciences, the analysis of the fluorescence fluctuation amplitudes at equilibrium, best described by the photon counting distribution of the fluorescence signal, is a rather new bioscientific tool.[2,22–25]

A first method employed in the investigation of the fluorescence fluctuation amplitudes has been developed by Qian and Elson and analyses the central and ordinary moments of the fluorescence fluctuations, i.e. the moment analysis of fluorescence intensity distribution (MAFID).[22] The main disadvantage of this technique is that the number of moments, which are considered in the simulation of the photon counting histogram of the fluctuating fluorescence signal, is arbitrarily chosen.[23] A method which avoids the arbitrary selection of parameters and is based on the theory of photon detection (Saleh, 1978) is the photon counting histogram (PCH) analysis developed by Chen et al.[24] In the PCH analysis, the shape of the point-spread function (PSF) is explicitly taken into consideration, while allowing Poissonian number fluctuations of the molecules within the observation volume. The fluorescence fluctuations caused by a small number of molecules in the observation volume yield a super-Poissonian distribution, i.e. a bistochastic distribution, of photon counts.[24] The influence of the shape of the observation volume on the photon counting distribution in the confocal microscopy is discussed elsewhere.[26] Furthermore, the PCH analysis offers

another way to distinguish between different species, which is based on differences in the molecular brightness, i.e. the mean number of photons emitted by a molecule within a sampling period.[25,27] In the last years, the advantages of the PCH technique have also been demonstrated in investigations of biological systems.[4–6,23] A similar method to the PCH analysis, the fluorescence intensity distribution analysis (FIDA), was applied in the investigation of DNA hybridisation and cleavage.[28]

In the PCH analysis, the theoretical photon counting distribution is defined as a convergent series of terms, which describe the photon counting statistics of one, two, three etc. fluorescing molecules within the observation volume.[24,25] The parameters, which influence this distribution for a single fluorescing species are the molecular brightness ϵ and the average number $\overline{N}$ of molecules within the observation volume.[24] Numerically, this series cannot be calculated up to infinity but only up to the maximal number N_{max} of molecules, the fluorescence of which simultaneously contributes to the detected signal, i.e. up to N_{max} for which the series converges to its limit. Physically, the calculation of the series up to infinity describes the situation, in which the fluorescence signal emitted by the sample is registered over an infinite time with an infinite short time resolution so that there is a probability of simultaneously monitoring even an infinite number of molecules. However, under real circumstances, both the measurement time and the time resolution are finite and only the fluorescence of at most N_{max} molecules relevantly contribute to the detected signal. Thus, N_{max} is another physical parameter, which influences the simulated photon counting histogram in the PCH analysis.

While in FCS, N_{max} does not directly influences the shape of the autocorrelation function, in the PCH analysis this parameter appears explicitly in the theoretical photon counting distribution. Since N_{max} is the relevant parameter, which determines the single-molecule detection limit according to its definition, the PCH analysis is the appropriate FFS technique for a quantitative determination of $\overline{N}$ at the single-molecule detection limit.

We apply for the first time the photon counting histogram analysis to quantitatively determine the single-molecule detection limit and discuss the influence of instrumental factors and of molecular properties, i.e. of the molecular brightness e, on at this limit. Furthermore, by means of PCH analysis we determine $\overline{N}$ at the detection limit, for which the fluorescence signal can no longer be distinguished from the background, and analyse the influence of the molecular brightness ϵ

on it. The single-molecule detection limit and the detection limit (background) define the single-molecule detection regime, i.e. the range of $\overline{N}$ in which only the fluorescence of individual molecules is detected at a time.

In order to verify the reliability of the PCH analysis on the single-molecule detection level, we approximate experimental photon counting histograms of the fluorescence signal originating from low concentration solutions of coumarin 153 with theoretically calculated super-Poissonian distributions. Thereby, we obtain the average number $\overline{N}$ of molecules within the observation volume and the molecular brightness ϵ of coumarin 153 under the given experimental conditions. The parameter $\overline{N}$ obtained by means of PCH analysis is compared to that determined by means of FCS and from the concentration of the bulk solution, respectively. Moreover, the molecular brightness ϵ obtained in the PCH experiments is employed to determine $\overline{N}$ in the single-molecule detection regime for coumarin 153 under the given experimental conditions.

The method for the quantitative determination of the single-molecule detection regime described in this work is generally valid for all FFS techniques and allows the control of the experimental parameters, i.e. chromophore concentration, laser power and excitation wavelength, for an accurate design of single-molecule experiments.

4.3 Photon Counting Statistics

In typical fluorescence fluctuations experiments, one or few molecules, which dwell in a small region around the laser focus, i.e. in the observation volume, are excited into the first (S_1) or a higher (S_n) singlet state, relax into the energetically lowest vibrational state of S_1 and fluoresce back to the ground state S_0. The absorption-fluorescence cycles can be interrupted by transport processes, e.g. diffusion, or by photophysical processes, e.g. photobleaching or intersystem crossing.[19,20,30] The emitted fluorescence photons are detected by a photon counter, usually an avalanche photodiode (APD). The fluctuations of the detected fluorescence signal contain information about molecular parameters, which can be extracted by means of fluorescence correlation spectroscopy (FCS) or photon counting histogram (PCH) analysis. In the following we will focus our attention on the PCH analysis, i.e. on the analysis of the fluctuation amplitudes of the detected fluorescence signal originating from molecules present in the excitation volume.

The photon counting statistics of the detected fluorescence signal stemming from molecules within the observation (excitation) volume is described in a semiclassical manner by Mandel's formula:[24,25]

$$p(k,T) = \int_0^\infty Poi\left(k, \eta_E \cdot E\right) \cdot p(E) \cdot dE \tag{4.1}$$

Here, k is the number of photons detected in the sampling time T, E is the emitted energy in units of number of photons per sampling time T, and η_E is the total detection efficiency.

Two random processes determine the photon counting distribution of the detected fluorescence signal originating from the molecules present in the excitation volume. The first process reflects the statistical independence of the photoelectric detection process for coherent electromagnetic radiation (the noise of the detector) restored by the Poissonian distribution $Poi\left(k, \eta_E \cdot E\right)$:[24,25]

$$Poi\left(k, \eta_E \cdot E\right) = \frac{\left(\eta_E \cdot E\right)^k e^{-\eta_E \cdot E}}{k!}\,. \tag{4.2}$$

This distribution describes the photon counting statistics of the detected fluorescence signal originating from a light source with an absolutely constant intensity, i.e. the emitted energy E is constant in time. The second source of randomness is the fluorescence process itself. The photon counting statistics of the time-dependent fluctuations of the emitted energy E is described by $p(E)$. Consequently, the Poissonian distribution of a light source, which emits a constant signal in time and space, is broadened if the emitted signal fluctuates and, thus, the photon counting histogram $p(k,T)$ of the detected fluorescence signal is a super-Poissonian distribution, i.e. a bistochastic distribution.[24]

This semiclassical approach accurately describes the photon counting distributions measured in fluorescence fluctuation experiments so that no fully quantum-mechanical approach is necessary.[24]

The fluctuations of the emitted fluorescence signal are caused by two factors:

- the spatially non-uniform illumination of the excitation volume given by the point spread function $PSF(r,z)$ and
- the variation of the number of molecules within the excitation volume due to transport and photophysical processes.

The point spread function $PSF(r,z)$, i.e. the unitless intensity profile, describes the space-dependence of the emitted energy E. Since in our experiments

the molecules are simultaneously excited by two photons, in the following we will focus our attention on the case of the two-photon absorption. It has been demonstrated that the intensity profile of a two-photon excitation volume is well approximated by a $2D$-Gaussian-Lorentzian distribution:[16,26]

$$PSF(r,z) = \frac{4\,\omega_0^2}{\pi^2\,\omega^2(z)} \cdot e^{-\left[4\,r^2/\omega^2(z)\right]} \qquad \text{with} \qquad \omega^2(z) = \omega_0^2 \left[1 + \left(\frac{z}{z_R}\right)^2\right] \tag{4.3}$$

Thereby, ω_0 is the secondary axis and z_R the principal axis of the elliptical excitation volume V_0 defined by Mertz et al.[16] z and r are cylindrical coordinates.

Let us consider that one molecule freely diffuses within the observation volume V_0 during all the measurement time and that, in agreement with our experiments, no photobleaching or intersystem crossing occurs.[29] In this case the fluctuations of the emitted fluorescence signal are determined only by the spatially non-uniform illumination of the excitation volume.

Considering that the integration time T is short enough to accurately track the fluctuations of the emitted fluorescence signal and the emitted energy E is the product between the molecular brightness and the point spread function $\epsilon \cdot PSF(r,z)$, the photon counting distribution of the detected fluorescence signal $p(k,T)$ for one molecule is given by:[24]

$$p_1\left(k; V_0, \epsilon\right) = \frac{1}{V_0} \cdot \frac{\pi^2\,\omega_0^4}{4\,\lambda k!} \int_{-\infty}^{\infty} \left(1+x^2\right) \cdot \gamma\left(k, \frac{4\,\epsilon}{\pi^2\left(1+x^2\right)^2}\right) \qquad \text{for} \qquad k \neq 0\,. \tag{4.4}$$

The corresponding term for no emitted photons during a sampling period T, i.e. $k = 0$, is:

$$p_1\left(0; V_0, \epsilon\right) = 1 - \sum_{k=1}^{k_{max}} p_1\left(k; V_0, \epsilon\right) \tag{4.5}$$

Here, λ is the excitation wavelength, x is the ratio z/z_R, k_{max} is the maximum number of photons detected during an integration period T and ϵ is the molecular brightness $\epsilon = \phi_0^2\,\delta\,K\,\eta_E\,T$ defined as the average number of emitted photons per molecule and sampling time T. ϕ_0 is the excitation photon flux at the focus, K is the instrument-dependent constant and δ is the effective two-photon absorption cross-section. γ is the alternative incomplete gamma function, which was numerically evaluated using a corresponding recurrence pattern (see Appendix).

If N independent molecules of the same species freely diffuse within the observation volume V_0 during all the measurement time, the corresponding photon counting distribution of the detected fluorescence signal is given by the N-fold

convolution of the function $p_1\left(k;V_0,\epsilon\right)$:[24]

$$p_N\left(k;V_0,\epsilon\right)=\underbrace{p_1\left(k;V_0,\epsilon\right)\otimes\ldots\otimes p_1\left(k;V_0,\epsilon\right)}_{N-fold}\,. \tag{4.6}$$

Up to this point we considered that the number of molecules within the excitation volume remains constant during all the measurement time and the fluctuations of the emitted fluorescence signal are induced only by the spatially non-uniform illumination of the excitation volume. However, due to transport and photophysical processes, in our case diffusion, the number of molecules present in the observation volume varies. Since the observation volume is much smaller than the reservoir of molecules, the probability that N molecules simultaneously dwell in the excitation volume is governed by Poissonian statistics:[24]

$$Poi\left(\overline{N},N\right)=\frac{e^{-\overline{N}}\cdot\overline{N}^{N}}{N!}\,. \tag{4.7}$$

Here, N is the actual number and $\overline{N}$ the average number of molecules within the observation volume V_0. The average number of molecules present in V_0 is defined as $\overline{N}=N_A\cdot c\cdot V_0$ where c is the concentration of the bulk solution and N_A the Avogadro number.

Thus, considering both sources of fluctuations originating from the fluorescence process itself, the photon counting distribution of the detected fluorescence signal stemming from molecules present in the excitation volume V_0 is given by the sum over all photon counting distributions $p_N\left(k;V_0,\epsilon\right)$ weighted with the corresponding Poissonian term $Poi\left(\overline{N},N\right)$:[24]

$$\Pi\left(k;\overline{N},\epsilon\right)=\sum_{N=0}^{\infty}p_N\left(k;V_0,\epsilon\right)\cdot Poi\left(\overline{N},N\right)\,. \tag{4.8}$$

Here, the function $p_0\left(k;V_0,\epsilon\right)$ represents the Poissonian distribution $Poi\left(\overline{k},k\right)$ of the background photons with $\overline{k}$ the average number of background photons detected during a sampling period T.

Since the excitation volume V_0 is a parameter which influences only the amplitude of the photon counting histogram but not its shape, the normalised distribution $\Pi\left(k;\overline{N},\epsilon\right)$ for one fluorescing species depends only on two parameters: the molecular brightness ϵ and the average number $\overline{N}$ of molecules present in the excitation volume.[24,25]

Numerically the function $\Pi\left(k;\overline{N},\epsilon\right)$ cannot be calculated up to infinity. However, since $\Pi\left(k;\overline{N},\epsilon\right)$ is a convergent series, it can accurately be evaluated by

summing up to a maximum number N_{max} of molecules simultaneously present in the excitation volume, the fluorescence of which still has a significant contribution to the detected signal.

$$\Pi\left(k;\overline{N},\epsilon,N_{max}\right)=\sum_{N=0}^{N_{max}}p_N\left(k;V_0,\epsilon\right)\cdot Poi\left(\overline{N},N\right) \tag{4.9}$$

Thus, beside the molecular brightness ϵ and the average number of molecules $\overline{N}$ within the excitation volume, another parameter influences the distribution $\Pi(k)$, i.e. the maximum number N_{max} of fluorescing molecules simultaneously present in the observation volume. In order to reduce the number of parameters in the fitting procedure, N_{max} is usually fixed to be very large ($N_{max} \ll \overline{N}$). However, this parameter is the quantitative indicator of the single-molecule detection regime and, thus, of particular significance. The deviation between the distribution $\Pi\left(k;\overline{N},\epsilon\right)$ calculated up to $N_{max}=1$ and up to $N_{max}=2$, respectively, is in the case of single molecule detection equal to 0, i.e. the series $\Pi\left(k;\overline{N},\epsilon,N_{max}\right)$ already converges to its limit for $N_{max}=1$. A pragmatic approach, which is more relevant in experimental investigations, defines that the single-molecule detection regime is reached if the deviation between $\Pi\left(k;\overline{N},\epsilon,N_{max}=1\right)$ and $\Pi\left(k;\overline{N},\epsilon,N_{max}=2\right)$ does not exceed the experimental uncertainty.

4.4 Experiment

The basic set-up used to register the fluorescence signal in the fluorescence fluctuations experiments is similar to that described by Mertz et al.[16] The characteristics of the pulsed laser beam are 200 fs pulse width and 76 MHz repetition rate. A microscope objective Plan Neofluar (40×, $NA = 1.3$, oil-immersion) of the company Carl Zeiss is used to focus the tenfold extended laser beam into the sample. The dimensions of the effective two-photon excitation volume are for an excitation wavelength λ of 800 nm: secondary axis $\omega_0 = 334$ nm, principal axis $z_R = 1570$ nm and volume $V_0 \approx 0.74$ fL.[29] These values were validated in experiments with fluorescent latex microbeads for the x-y-resolution and with FITC-monolayers for the z-resolution.[30] As detection unit we use an avalanche photodiode (SPCM-AQ-131, EG&G Optoelectronics Canada), encompassing a total detection efficiency of 3% for coumarin 153 ($\lambda_F = 532$ nm). The signal of the avalanche photodiode is directed to a multi channel scaler (MCD-2E, 7882, FAST ComTec) operated at 10 kHz (sampling period $T = 100$ μs). The total

measurement duration is 13.2 s. Thus, the total number of data points M is $1.32 \cdot 10^5$.

For the fluorescence fluctuations experiments we used solutions (50, 100, 200, 400 pmol L^{-1} and 1 nmol L^{-1}) of coumarin 153 (Radiant Dyes) in glycol p.a.

4.5 Data Analysis

If the deviation between the distributions $\Pi\left(k; \overline{N}, \epsilon, N_{max} = 1\right)$ and $\Pi(k; \overline{N}, \epsilon, N_{max} = 2)$ is equal to or lower than the experimental uncertainty, it can be assumed that the single-molecule detection regime is reached, i.e. the probability to simultaneously detect the fluorescence of two molecules is negligible.

The experimental uncertainty represents the difference between the normalised experimental data $p_{exp}(k)$ and the calculated photon counting histogram $\Pi\left(k; \overline{N}, \epsilon\right)$ and is given by the χ^2-parameter. Assuming that the probability of observing k photons n times out of M trials is a binomial distribution $B\left(n, M, p_{exp}(k)\right)$, the χ^2-parameter is given by:[24,25]

$$\chi^2 = \frac{\sum_{k=0}^{k_{max}} \left(M \frac{p_{exp}(k) - \Pi\left(k; \overline{N}, \epsilon\right)}{\sigma} \right)^2}{k_{max} - d} . \tag{4.10}$$

Here, M is the total number of trials (data points), k_{max} is the maximum number of photons detected during a sampling period T, d is the number of fitting parameters (ϵ and $\overline{N}$), $p_{exp}(k)$ is the experimental probability of detecting k photons during a sampling period T and σ is the standard deviation defined as $\sigma = \sqrt{M \cdot p_{exp}(k) \cdot (1 - p_{exp}(k))}$. In addition to the reduced χ^2-parameter, the normalised residuals $r(k)$ of the fitting procedure indicate the quality of the theoretical model:[24,25]

$$r(k) = M \frac{p_{exp}(k) - \Pi\left(k; \overline{N}, \epsilon\right)}{\sigma} . \tag{4.11}$$

We define the $\chi^{2\#}$-parameter analogously to the χ^2-parameter, in order to quantify the deviation between the distributions $\Pi\left(k; \overline{N}, \epsilon, N_{max} = 1\right)$ and $\Pi(k; \overline{N}, \epsilon, N_{max} = 2)$:

$$\chi^{2\#} = \frac{\sum_{k=0}^{k_{max}} \left(M \frac{\Pi\left(k; \overline{N}, \epsilon, N_{max} = 1\right) - \Pi\left(k; \overline{N}, \epsilon, N_{max} = 2\right)}{\sigma'} \right)^2}{k_{max} - d} . \tag{4.12}$$

Here, σ' is defined as $\sqrt{M \cdot \Pi\left(k; \overline{N}, \epsilon, N_{max} = 1\right) \cdot \left(1 - \Pi\left(k; \overline{N}, \epsilon, N_{max} = 1\right)\right)}$.

Consequently, the single-molecule detection limit is mathematically described by the relation: $\chi^2 = \chi^{2\#}$. The factors which influence the $\chi^{2\#}$-parameter, i.e. the single-molecule detection limit, are the average number of molecules within the excitation volume and the molecular brightness ϵ.

The deviation between the Poissonian distribution $Poi\left(\overline{k}, k\right)$ of the background photons and the distribution $\Pi\left(k; \overline{N}, \epsilon, N_{max} = 1\right)$ given by the $\chi^{2\star}$-parameter and defined analogously to the χ^2-parameter indicates the detection limit of the experimental method:[20]

$$\chi^{2\star} = \frac{\sum_{k=0}^{k_{max}} \left(M \frac{\Pi\left(k; \overline{N}, \epsilon, N_{max} = 1\right) - Poi\left(\overline{k}, k\right)}{\sigma'} \right)^2}{k_{max} - d}. \tag{4.13}$$

If this parameter is lower than the experimental uncertainty, the emitted fluorescence signal cannot be distinguished from the background and, thus, cannot be detected.

Thus, the single-molecule detection regime is defined as the range between the upper single-molecule detection limit ($\chi^{2\#} = \chi^2$) and the lower detection limit ($\chi^{2\star} = \chi^2$).

4.6 Results and Discussion

4.6.1 PCH Analysis of Experimental Data

The fluorescence signal of very diluted solutions of coumarin 153 in glycol is analysed by means of photon counting histogram (PCH) analysis in order to verify the reliability of this method in evaluating fluorescence fluctuations around the single-molecule detection limit. Moreover, in this way the experimental uncertainty restored by the χ^2-parameter is obtained, which is necessary for the quantitative determination of the single-molecule detection regime by means of PCH analysis.

The fluorescence signal of four solutions of coumarin 153 in glycol (50, 100, 200 and 400 pmol L^{-1}) was registered at a mean laser power $\overline{P} = 22$ mW and at an excitation wavelength $\lambda = 800$ nm. Under these conditions, no photobleaching or intersystem crossing occurs and, thus, the number of fluorescing molecules present in the excitation volume varies only due to diffusion.[29] The sampling time $T = 100$ μs is short enough to track the fluctuations of the fluorescence signal induced by the diffusion of the fluorescing molecules through the excitation

volume. The mean background count rate of glycol, including a dark count rate of 200 Hz, amounts to 500 Hz. The experimental photon counting histograms of the detected fluorescence signals of the four solutions are approximated by calculated photon counting distributions $\Pi(k)$. N_{max} is fixed to 50 molecules, a few hundred times larger than the average number $\overline{N}$ of molecules present in the excitation volume in order to assure that all molecules, which might contribute to the detected fluorescence signal, are taken into account.

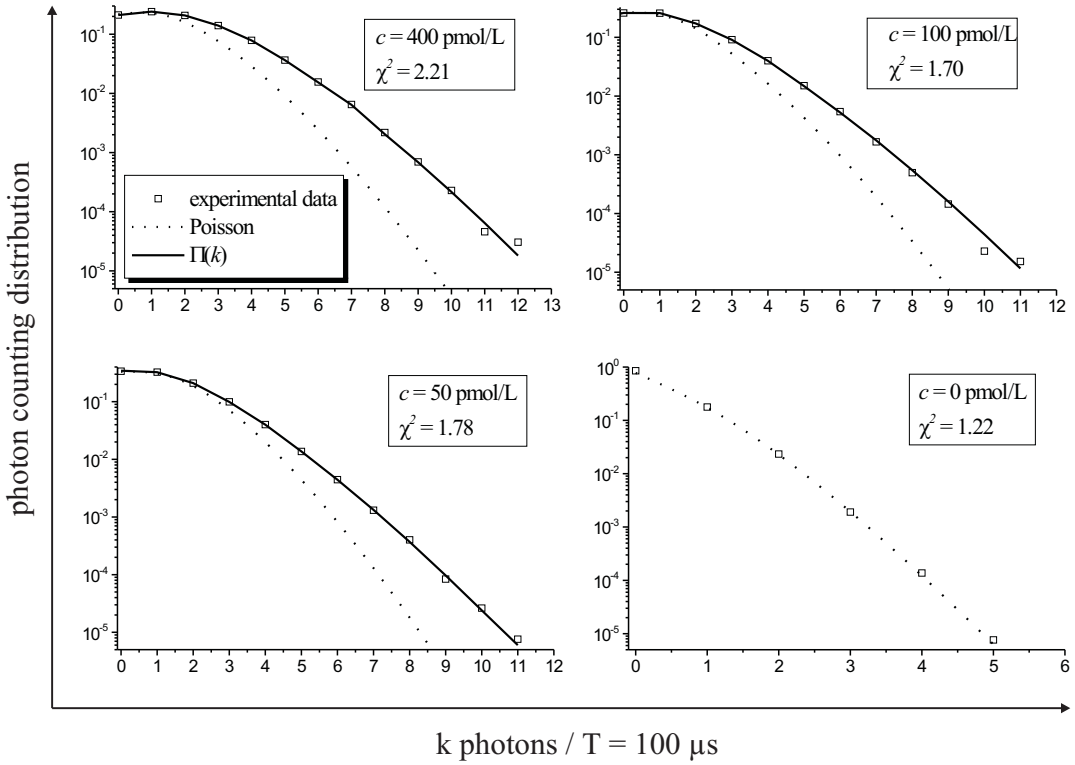

Fig. 4-1: Experimental photon counting distributions of the detected signal of three different solutions of coumarin 153 in glycol (400 pmol L^{-1}, 100 pmol L^{-1}, 50 pmol L^{-1}) and of the solvent (glycol), calculated super- Poisson distributions $\Pi(k)$ and corresponding Poisson distributions. Experimental parameters: $\overline{P}$ = 22 mW, λ = 800 nm. Parameters employed in the simulation of $\Pi(k)$: $T = 100s$, $N_{max} = 50$ molecules, $M = 1.32 \cdot 10^5$. Fitted parameters: $\epsilon = 1.21 \pm 0.02$ cpm; $\overline{N} = 0.024$ for $c = 50$ pmol L^{-1}, $\overline{N} = 0.047$ for $c = 100$ pmol L^{-1} and $\overline{N} = 0.196$ for $c = 400$ pmol L^{-1}.

Fig. 4-1 demonstrates that the experimental photon counting distributions are well approximated by the functions $\Pi(k)$ (χ^2 amounts to ≈ 2) and are significantly broader than the corresponding Poissonian distributions. The photon counting distribution of the background signal is accurately approximated by a Poissonian

distribution ($\chi^2 = 1.22$). In all experiments the residuals $r(k)$ oscillate around 0 with a maximal amplitude smaller than 10^{-5} (data not shown).

By fitting the experimental photon counting distributions with the simulated functions $\Pi(k)$ a molecular brightness ϵ of 1.21 ± 0.02 cpm (*counts per molecule*) was obtained. Since the molecular brightness depends only on the molecular and instrumental parameters but not on the average concentration of dye within the observation volume, this parameter is constant for all four concentrations. In order to obtain a more general molecular parameter independent from the integration time T, the molecular brightness per time is defined as $\epsilon_T = \epsilon/T$.[24] This parameter amounts to 12100±200 cpms (*counts per molecule and second*) for coumarin 153, detected at a mean laser power $\overline{P} = 22$ mW and at an excitation wavelength $\lambda = 800$ nm.

The average number $\overline{N}$ of molecules within the excitation volume also obtained by approximating the experimental photon counting distributions with the simulated functions $\Pi(k)$ is in good agreement with both the average number $\overline{N}$ of molecules within the excitation volume calculated from the bulk concentration of the solution $\overline{N} = c \cdot V_0 \cdot N_A$ and the results of fluorescence correlation spectroscopy (FCS) experiments. (Table 4-1)

c [pmol L^{-1}]	$\overline{N} = c\,V_0\,N_A$	$\overline{N}_{PCH}$	$\overline{N}_{FCS}$
50	0.022	0.024	-
100	0.045	0.047	0.063
200	0.088	0.095	0.115
400	0.177	0.196	0.251

Tab. 4-1: The mean number $\overline{N}$ of molecules within the excitation volume as it results from the bulk concentration of the solutions $\overline{N} = c \cdot V_0 \cdot N_A$, from the approximation of the experimental photon counting distributions with the function $\Pi(k)$ ($\overline{N}_{PCH}$) and from the analysis of the fluorescence autocorrelation functions ($\overline{N}_{FCS}$).

The average number $\overline{N}$ of molecules within the excitation volume can be acquired in FCS experiments from the amplitude of the fluorescence autocorrelation functions. If no photobleaching or intersystem crossing occurs, the amplitude of

the autocorrelation function is given by:[16]

$$G(0_+) = \frac{1}{\overline{N}} \cdot \left(\frac{I_F}{I_F + I_B} \right)^2 \tag{4.14}$$

where I_F is the mean fluorescence signal and I_B is the mean background signal.

As expected the parameter $\overline{N}$ determined by means of PCH analysis is more accurate than that determined by means of FCS as shown in Tab. 4-1 if the bulk concentration, $\overline{N} = c \cdot V_0 \cdot N_A$, serves as reference.

The results presented in this section demonstrate the reliability of the theoretical PCH model to simulate the photon counting distribution of the fluctuating fluorescence signal around the single-molecule detection limit. Moreover, we obtain a typical experimental uncertainty χ^2 around 2. (see inset of Fig. 4-1)

4.6.2 Single-Molecule Detection Level

Rigorously defined, the single-molecule detection level is reached if only the fluorescence of single molecules present in the excitation volume is detected at a time. In the following we will demonstrate how the single-molecule detection level in fluorescence fluctuations experiments can quantitatively be determined by means of PCH analysis.

The photon counting histogram of the detected fluorescence signal originating from one or few molecules is restored by the series $\Pi\left(k; \overline{N}, \epsilon, N_{max}\right)$. On the single-molecule detection level, only the fluorescence signal of individual molecules is detected and, thus, the series $\Pi\left(k; \overline{N}, \epsilon, N_{max}\right)$ already converges to its limit for $N_{max} = 1$. Consequently, the deviation between the distributions $\Pi\left(k; \overline{N}, \epsilon, N_{max} = 1\right)$ and $\Pi\left(k; \overline{N}, \epsilon, N_{max} = 2\right)$ quantified by the $\chi^{2\#}$-parameter is negligible in the case of single-molecule detection. The other two parameters of the series $\Pi\left(k; \overline{N}, \epsilon, N_{max}\right)$, i.e. the average number $\overline{N}$ of molecules within the excitation volume and the molecular brightness ϵ, implicitly influence the $\chi^{2\#}$-parameter and, thus, the upper limit of the single-molecule detection. We will first concentrate our attention on the influence of the average number $\overline{N}$ of molecules present in the excitation volume on the $\chi^{2\#}$-parameter and then on the influence of the molecular brightness ϵ on $\chi^{2\#}$.

Fig. 4-2 shows the photon counting distributions $\Pi\left(k; \overline{N}, \epsilon, N_{max}\right)$ calculated for three different parameters $\overline{N}$ and different N_{max}.

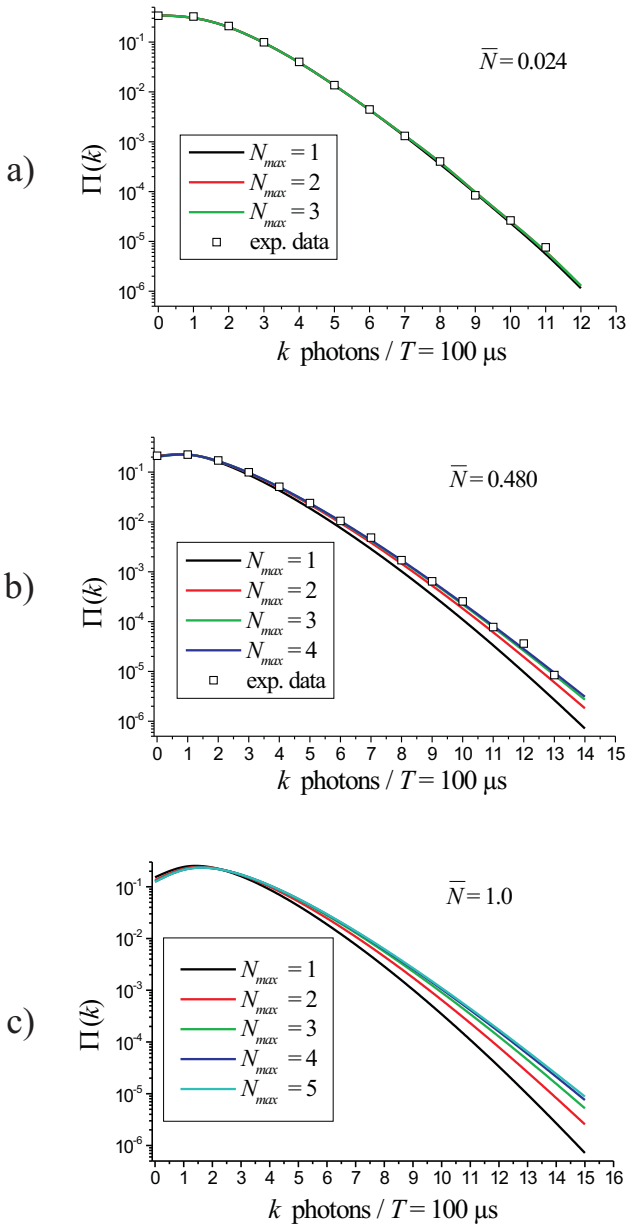

Fig. 4-2: a) Experimental data of a 50 pmol L^{-1} solution of coumarin 153 in glycol and corresponding photon counting distributions $\Pi\left(k; \overline{N} = 0.024, \epsilon, N_{max}\right)$ calculated for N_{max} between 1 and 3 molecules; b) experimental data of a 1 nmol L^{-1} solution of coumarin 153 in glycol and corresponding photon counting distributions $\Pi\left(k; \overline{N} = 0.48, \epsilon, N_{max}\right)$ calculated for N_{max} between 1 and 4 molecules; c) photon counting distributions $\Pi\left(k; \overline{N} = 1, \epsilon, N_{max}\right)$ calculated for N_{max} between 1 and 5 molecules. The contribution of the fluorescence of more than one molecule to the detected signal is significant for $\overline{N} = 0.48$ (up to 3 molecules) and $\overline{N} = 0.48$ (up to 4 molecules) but negligible for $\overline{N} = 0.024$. Parameters employed in the simulation: $T = 100$ μs, $\epsilon_T = 12100$ cpms.

If the average number of molecules $\overline{N}$ within the excitation volume is equal to 1, the maximum number N_{max} of molecules which simultaneously contribute to the detected signal is significantly larger than 1 (up to 4 molecules) (Fig. 4-2 c). Even for $\overline{N} = 0.48$, N_{max} is larger than one and the experimental photon counting distribution of the fluorescence signal of a 1 nmol L^{-1} coumarin 153 solution cannot be approximated by $\Pi\left(k; \overline{N} = 0.48, \epsilon, N_{max} = 1\right)$ (Fig. 4-2 b). Only for $\overline{N} \ll 1$, the contribution of two simultaneously fluorescing molecules to the detected signal vanishes (Fig. 4-2 a). In this case, the theoretical function $\Pi\left(k; \overline{N} = 0.024, \epsilon, N_{max} = 1\right)$ accurately approximates the experimental data (50 pmol L^{-1} coumarin 153 solution). The molecular brightness employed in the simulation is $\epsilon_T = 12100$ cpms ($T = 100$ μs).

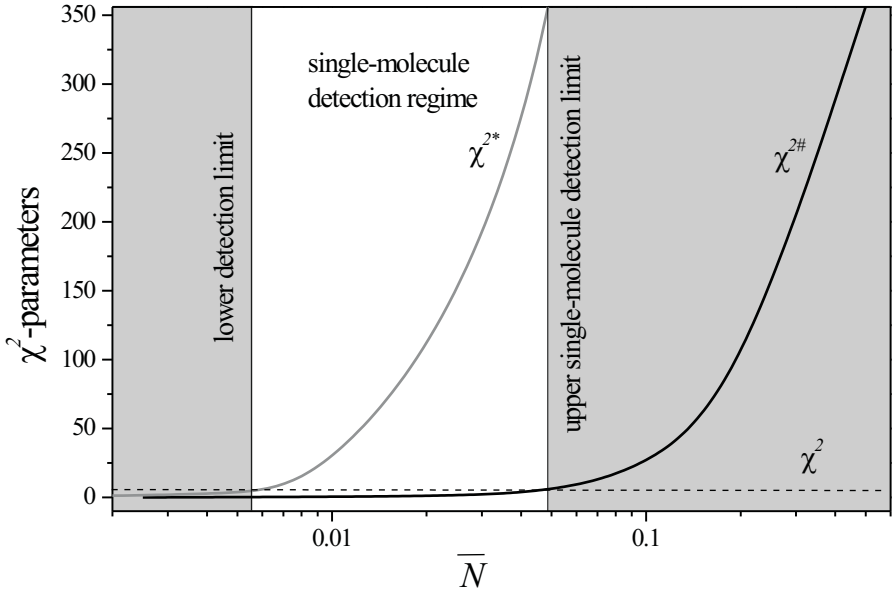

Fig. 4-3: The $\chi^{2\#}$-parameter and the $\chi^{2\star}$-parameter as functions of the mean number of molecules within the excitation volume. By comparing the functions $\chi^{2\#}(\overline{N})$ resp. $\chi^{2\star}(\overline{N})$ with the experimental uncertainty χ^2, the upper single-molecule detection limit is determined to be at $\overline{N} = 0.048$ molecules while the lower detection limit is reached at $\overline{N} = 0.0057$ molecules. Parameters employed in the simulation: $\epsilon_T = 12100$ cpms, $T = 100$ μs, $M = 10^6$.

Quantitatively, the upper single-molecule detection limit is mathematically defined by the relation $\chi^{2\#} = \chi^2$. Thus, the influence of the average number $\overline{N}$ of molecules present in the excitation volume on the upper single-molecule detection

limit is investigated by comparing the $\chi^{2\#}$-parameter dependence on $\overline{N}$ with the constant value of the experimental uncertainty χ^2 (in our experiments $\chi^2 \approx 2$). The function $\chi^{2\#}(\overline{N})$ is calculated for a fixed molecular brightness $\epsilon_T = 12100$ cpms, i.e. the molecular brightness of coumarin 153 at $\overline{P} = 22$ mW and $\lambda = 800$ nm.

As Fig. 4-3 shows, the $\chi^{2\#}$-parameter tends asymptotically to zero at low $\overline{N}$ and increases super-polynomial for $\overline{N}$ larger than 0.1 molecules. By comparing the function $\chi^{2\#}(\overline{N})$ with the χ^2-parameter, i.e. experimental uncertainty, we find that the upper single-molecule detection limit is already reached at $\overline{N} = 0.048$ (or $c \approx 110$ pmol L^{-1} for a $V_0 = 0.74$ fL) for $\epsilon_T = 12100$ cpms.

For $\overline{N}$ below 0.0057 molecules ($c \approx 13$ pmol L^{-1} for a $V_0 = 0.74$ fL) the deviation between the photon counting distribution $\Pi\left(k; \overline{N}, \epsilon, N_{max} = 1\right)$ and the Poisson distribution of the background signal given by the $\chi^{2\star}$-parameter is lower than our experimental uncertainty χ^2. Thus, below this level no detection is possible for $\epsilon_T = 12100$ cpms. (Fig. 4-3)

Up to this point, only the influence of the average number of molecules within the excitation volume on the $\chi^{2\#}$-parameter and on the $\chi^{2\star}$-parameter, respectively, for a fixed molecular brightness has been discussed. However, the molecular properties and the instrumental factors significantly influence the dependence of these parameters on and, thus, the regime of single-molecule detection. Consequently, we investigate the functions $\chi^{2\#}(\overline{N})$ and $\chi^{2\star}(\overline{N})$ for different values of the molecular brightness ϵ_T in the range 1625 to 30000 cpms ($T = 100$ μs). These values cover the typical range of molecular brightness met in biophysical investigations.[4–6]

The comparison of the functions $\chi^{2\#}(\overline{N})$ calculated for different values of ϵ_T with the experimental uncertainty χ^2 evidences that the mean number $\overline{N}$, at which the upper single-molecule detection limit is reached, increases with decreasing molecular brightness ϵ_T (Fig. 4-4). Consequently, $\overline{N}$, at which the upper single-molecule detection limit is reached, amounts to 0.007 molecules for a molecular brightness $\epsilon_T = 30000$ cpms while the same parameter for a ten times lower molecular brightness $\epsilon_T = 3250$ cpms amounts to 0.42 molecules.

The comparison of the functions $\chi^{2\star}(\overline{N})$ calculated for the same values of ϵ_T with the experimental uncertainty χ^2 reveals that $\overline{N}$, at which the fluorescence signal vanishes in the background (i.e. the detection limit), also increases with decreasing molecular brightness (data not shown).

Concluding, the fluorescence of individual molecules is only detected in the

range given by the lower detection limit ($\chi^{2\star} = \chi^2$) and the upper single-molecule detection limit ($\chi^{2\#} = \chi^2$). The values of $\overline{N}$ corresponding to these limits vary with the molecular brightness ϵ_T, however, $\overline{N}$ at the lower detection limit is always smaller than $\overline{N}$ at the upper single-molecule detection limit. Thus, experiments in single-molecule (SM) detection regime can generally be performed for all values of the molecular brightness, i.e. independent from the fluorescing species and under arbitrary instrumental conditions. The only experimental parameter, which must be controlled in SM experiments, is the average number $\overline{N}$ of molecules within the excitation volume, i.e. the chromophore concentration.

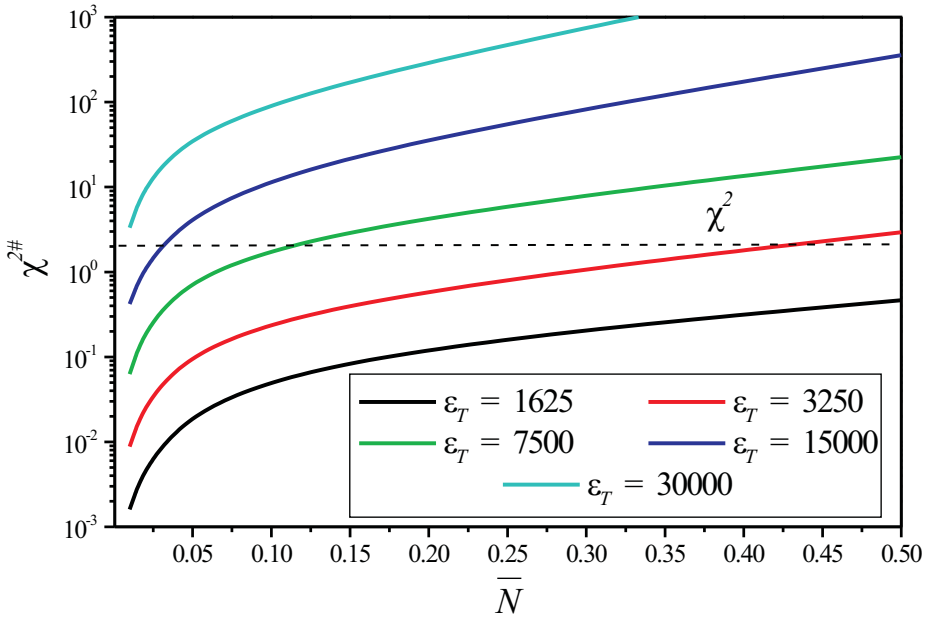

Fig. 4-4: The dependence of the $\chi^{2\#}$-parameter on the mean number $\overline{N}$ of molecules present in the excitation volume calculated for different values of the molecular brightness ϵ_T. Parameters employed in the simulation: $T = 100$ μs, $M = 10^6$.

However, since biological investigations should be carried out at low mean laser powers $\overline{P}$ in order to avoid photodamage at the sample and since the molecular brightness quadratically scales with $\overline{P}$, relevant experiments are possible only for ϵ_T up to a maximal value determined by the maximal non-invasive mean laser power. On the other side the concentration of the fluorescing species (directly proportional to $\overline{N}$) in the single-molecule detection regime is very large for low values of ϵ_T. A too large concentration of fluorescing species constitutes a sig-

nificant disadvantage in biological studies, e.g. in labelling experiments, since it may lead to modifications of the natural environment and, thus, to false results.

The quantitative determination of the single-molecule detection regime by means of PCH analysis is generally valid for all fluorescence fluctuation techniques. However, the SM regime is influenced by experiment typical factors like the experimental uncertainty and, thus, may slightly vary for different set-ups.

4.7 Conclusions

We presented a novel method based on the photon counting histogram (PCH) analysis, which enables the accurate design of fluorescence fluctuation experiments in single-molecule detection regime, since it restores the average number of molecules within the observation volume on the single-molecule detection level.

In the single-molecule detection regime the maximal number N_{max} of molecules simultaneously fluorescing in the observation volume is equal to one. Thus, under the same conditions the photon counting histogram of the fluctuating fluorescence signal mathematically described by the function $\Pi\left(k;\overline{N},\epsilon,N_{max}\right)$, i.e. a convergent series in N_{max}, already converges to its limit for $N_{max}=1$. The upper limit of the single-molecule detection level is practically reached if the deviation, i.e. the $\chi^{2\#}$-parameter, between $\Pi\left(k;\overline{N},\epsilon,N_{max}=1\right)$ and $\Pi\left(k;\overline{N},\epsilon,N_{max}=2\right)$ is equal to the experimental uncertainty given by the χ^2-parameter. The lower limit of the single-molecule detection level is reached if the deviation between the photon counting distribution $Poi\left(\bar{(}k),k\right)$ of the background signal and $\Pi(k;\overline{N},\epsilon,$ $N_{max}=1)$, i.e. $\chi^{2\star}$-parameter, equals the experimental uncertainty χ^2.

In the case of coumarin 153 excited at $\lambda=800$ nm and $\overline{P}=22$ mW ($\epsilon_T=$ 12100 cpms) the lower detection limit characterised by $\chi^{2\star}=\chi^2$ is reached at $\overline{N}=$ 0.0057 molecules while the upper single-molecule detection limit characterised by $\chi^{2\#}=\chi^2$ is reached at $\overline{N}=0.048$ molecules. $\overline{N}$ is the average number of molecules present in the excitation volume. Consequently, in single molecule FFS experiments, in which the observation volume V_0 is 0.74 fL and the molecular brightness ϵ_T amounts to 12100 cpms, the concentration c of the chromophore must be in the range 13 to 110 pmol L^{-1}.

Furthermore, we have investigated the influence of the molecular brightness ϵ_T, i.e. molecular and experimental parameters, on both the upper single-molecule detection and the lower detection limit and, thus, on the single-molecule detection regime. Theoretically, single-molecule experiments can be performed

at any values of the molecular brightness ϵ_T, i.e. under arbitrary experimental conditions. Only requirements specific for the investigated samples restrict the range of ϵ_T-values suitable for single-molecule detection experiments.

In order to determine the experimental uncertainty χ^2 and to verify the reliability of the PCH analysis on the single-molecule detection level, we have approximated experimental photon counting histograms of the fluorescence signal originating from low concentration solutions of coumarin 153 with theoretically calculated super-Poissonian distributions $\Pi\left(k; \overline{N}, \epsilon, N_{max}\right)$. In this way, we have obtained the mean number $\overline{N}$ of molecules present in the observation volume and the molecular brightness ϵ_T of coumarin 153 under the given experimental conditions. The parameter obtained by means of PCH analysis agrees with that determined from the bulk concentration c of the chromophore and by means of fluorescence correlation spectroscopy.

Appendix

The recurrence pattern used for the numerical evaluation of the alternative incomplete gamma function $\gamma(k,a) = \int_0^a t^k\, e^{-t}\, dt$ is given by:

$$\gamma(k,a) = -a^{k-1}\, e^{-a} + (k-1)\cdot\gamma(k-1,a) \qquad \text{for} \qquad k \geqslant 2\,. \tag{4.15}$$

For $k = 1$ the alternative gamma function is:

$$\gamma(1,a) = 1 - e^{-a}\,. \tag{4.16}$$

The parameter a is given by the ratio: $\dfrac{4\,\epsilon}{\pi^2\,\left(1+x^2\right)^2}$.

References

[1] P. Schwille, *Cell Biochem. Biophys.* **2001**, 34, 383-400

[2] R. Rigler, E.S. Elson, *Fluorescence Correlation Spectroscopy - Theory and Applications*, Springer, Berlin, p. 305-330, p. 411-437, p. 438-458, **2001**

[3] S. Nie, R.N. Zare, *Annu. Rev. Biophys. Biomol. Struct.* **1997**, 26, 567-596

[4] G. Chirico, S. Bettati, A. Mozzarelli, Y. Chen, J.D. Müller, E. Gratton, *Biophys. J.* **2001**, 80, 1973-1985

[5] Y. Chen, J.D. Müller, Q. Ruan, E. Gratton, *Biophys. J.* **2002**, 82, 133-144

[6] Y. Chen, L. Wie, J.D. Müller, *PNAS* **2003**, 100(26), 15492-15497

[7] A.A. Deniz, T.A. Laurence, M. Dahan, D.S. Chelma, P.G. Schultz, S. Weiss, *Annu. Rev. Phys. Chem. A* **2001**, 52, 233-253

[8] Y. Jung, E. Barkai, R.J. Silbey, *J. Chem Phys.* **2002**, 117, 10980-10995

[9] R. Rigler, M. Orrit, T. Basche, Single Molecule Spectroscopy - Nobel Conference Lectures, Springer, Berlin, p. 130-144, p. 227-256, p. 257-276 **2001**

[10] T. Schmidt, G.J. Schütz, W. Baumgartner, H.J. Gruber, H. Schindler, *J. Phys. Chem.* **1999**, 99, 17662-17668

[11] G.S. Harms, L. Cognet, P.H.M. Lommerse, G.A. Blab, H. Kahr, R. Gamsjger, H.P. Spaink, N.M. Soldatov, C. Romanin, T. Schmidt, *Biophys. J.* **2001** 81, 2639-2646

[12] W.P. Ambrose, P.M. Goodwin, J.H. Jett, A. van Orden, J.H. Werner, R.A. Keller, *Chem. Rev.* **1999**, 99, 2929-2956

[13] R. Rigler, L. Edman, Z. Földes-Papp, S. Wennmalm, Single Molecule Spectroscopy - Nobel Conference Lectures, R. Rigler, M. Orrit, T. Basche, Springer, Berlin, p. 177-195 **2001**

[14] M. Orrit, *Single Mol.* **2002**, 3, 255-265

[15] W. Denk, J.H. Strickler, W.W. Webb, *Science* **1990**, 248, 73-76

[16] J. Mertz, C. Xu, W.W. Webb, *Opt. Lett.* **1995**, 20, 2532-2534

[17] P. Schwille, U. Haupts, S. Maiti, W.W. Webb, *Biophys. J.* **1999**, 77, 2251-2256

[18] S.R. Aragon, R. Pecora, *J. Chem. Phys.* **1976**, 64, 1791-1803

[19] J. Widengren, R. Rigler, *Bioimaging* **1996**, 4, 149-157

[20] C. Eggeling, J. Widengren, R. Rigler, C.A.M. Seidel, *Anal. Chem.* **1998**, 70, 2651-2659

[21] K.G. Heinze, A. Koltermann, P. Schwille, *PNAS* **2000**, 97, 10377-10382

[22] H. Qian, E.L. Elson, *PNAS* **1990**, 87, 5479-5483

[23] Y. Chen, J.D. Müller, J.S. Eid, E. Gratton, New Trends in Fluorescence spectroscopy - Applications to Chemical and Life Sciences, (Springer, Berlin), Valeur, B.; Brochon, J.-C., p. 292-295, **2001**

[24] Y. Chen, J.D. Müller, P.T.C. So, E. Gratton, *Biophys. J.* **1999**, 77, 553-567

[25] J.D. Müller, Y. Chen, E. Gratton, *Biophys. J.* **2000**, 78, 474-486

[26] T.D. Perroud, B. Huang, M.I. Wallance, R.N. Zare, *ChemPhysChem* **2003**, 4, 1121-1123

[27] L.N. Hillesheim, J.D. Müller, *Biophys. J.* **2003**, 85, 1948-1958

[28] P. Kask, K. Palo, D. Ullmann, K. Gall, *PNAS* **1999**, 96(24), 13756-13761

[29] R. Niesner, W. Roth, K.-H. Gericke, *Chem.Phys.Chem.* **2004**, 5, 678-687

[30] A. Schönle, M. Glatz, S.W. Hell, *Appl. Opt.* **2000**, 39, 6306-6311

Chapter 5

3D-Resolved Investigation of the pH Gradient in Artificial Skin Constructs by means of Fluorescence Lifetime Imaging

5.1 Abstract

The development of substitutes for the human skin, e.g. artificial skin constructs (ASC), is of particular importance for the pharamceutical and dermatological research, since they represent economical test-samples for the validation of new medicines. In this regard, it is essential for the skin substitutes to be reliable models of the genuine skin, i.e. to have a similar morphology and functionality. Particularly important is the barrier function, i.e. the selective permeability of the skin, which is strongly related to the epidermal acidic mantle, i.e. the pH gradient of the superior skin layer.

Using 3D fluorescence lifetime imaging (FLIM) combined with two-photon scanning microscopy (TPM), we were able to measure the three dimensional pH gradient in the epidermis of BCECF-stained ASC with submicron resolution. Thereby, we found out that, similarly to the genuine skin, the surface of the artificial epidermis has an acidic character ($pH = 5.9$), while in the deeper layers the pH increases up to 7.0. Moreover, the pH gradient differs in the cell interior (up to 7.15) and in the intercellular matrix (up to 6.6). Apart from the similitude in the pH distribution, the genuine and the artificial skin proved to have also a similar morphology and to be characterised by similar distributions of the refractive index.

5.2 Introduction

Testing the effects of new drugs directly on skin samples represents an essential phase in the dermatological and pharamceutical research. Since the resources of genuine skin are limited, the development of economically convenient substitutes for the expensive human skin, which reliably mirror the behaviour under the influence of the investigated medicine, is of particular significance. Therefore, the skin models must have the same properties (morphology and functionality) as the human skin. Very promising skin models are the three-dimensional artificial skin constructs (ASC), which similarly to the genuine skin consist of an epidermis of differentiated keratinocytes and of a dermis.

In the following we will focus our attention on the barrier function of the skin, i.e. its selective permeability. It is known that an important role to the barrier function is played by the epidermal acidic mantle, i.e. the pH gradient in the epidermis.[1,2] Thus, in order to demonstrate the reliability of the artificial skin constructs as models of the genuine human skin in permeability studies, it is necessary to compare their acidic mantle, i.e. the pH gradient, with that of genuine skin.

Since for investigating the epidermal acidic mantle, the 3D spatial distribution of the pH is needed, bulk pH-experiments, which allow only the measurement of an average pH value at the skin surface, are evidently not appropriate. An alternative technique, which allows the measurement of the pH as a function of epidermal depth using a flat electrode, is based on tape stripping.[1] The main drawbacks of this procedure are the fact that it is intrinsically destructive and, thus, the natural function of the tissue is disturbed. Furthermore, it has a prone lateral resolution (in cm range), so that no subcellular measurement of the pH is possible within a depth layer.[1]

In order to visualise the skin with high 3D resolution and without damaging it, different microscopy techniques have been developed, e.g. tandem scanning microscopy,[3] confocal scanning microscopy and two-photon scanning microscopy.[4–7] Due to its advantages, i.e. non-invasive technique, excellent intrinsic 3D resolution, large penetration depth, low photodamage in the out-of-focus region and simple experimental set-up, the two-photon scanning microscopy (TPM) has proven to be the optimal method in the 3D resolved imaging of thick biological samples including skin and ASC.[8–10]

In standard TPM experiments, the fluorescence intensity emitted by the sam-

ple is registered. If the skin samples are stained with an appropriate indicator, for which the fluorescence spectrum varies with the pH, the spatial distribution of the pH in the epidermis can be determined. However, since the fluorescence intensity of the sample is strongly affected by experimental factors, e.g. modifications of the laser power and wavelength or variations of the chromophore concentration, and not only by the pH, such fluorimetry experiments lead to inaccurate results.

The fluorescence lifetime imaging (FLIM) is a versatile alternative to the fluorimetry techniques due to its remarkable instrumental stability. In this case, the parameter, which depends on the pH, is the fluorescence lifetime of the staining chromophore and not its fluorescence wavelength. This time-dependent parameter of the fluorescence signal is scarcely perturbed by experimental factors but for certain substances, e.g. BCECF, SNARF or SNAFL, it is very sensitive to the pH value.[11] FLIM experiments have been performed to monitor the pH gradient in stratum corneum of mouse skin.[1,2]

Moreover, FLIM found large application in the investigation of other cellular parameters, e.g. ions and oxygen concentration, viscosity,[12–15] as well as in the elucidation of vital processes like cell metabolism, photosythesis of green plants or FRET.[12,13,16–19] To the principal methods of measuring the fluorescence decay time in an image belong frequency-domain techniques[1,11,20–22] and time-domain techniques, e.g. time correlated single photon counting (TCSPC)[13,23] and time-gated procedures.[17–19]

Concluding, FLIM combined with two-photon scanning microscopy is the optimal technique to monitor the pH gradient in the artificial epidermis with a subcellular 3D resolution and without damaging the samples. Although very important in the characterisation of the barrier function of the ASC, to our knowledge, no such investigation of the artificial skin has been performed yet.

We employed time-domain FLIM combined with two-photon scanning microscopy in order to obtain the three-dimensional distribution of the pH in the epidermis of the ASC stained with BCECF. Thereby, the samples were neither photodamaged nor mechanically damaged.

In order to assure a high accuracy in the determination of the pH, we took into consideration that the fluorescence lifetime of BCECF may also be influenced by other factors than the pH such as refractive index n, viscosity η or ions concentration. While the influence of viscosity and ions concentration on the fluorescence lifetime of BCECF is negligible, n^2 is inversely proportional to the

fluorescence lifetime. Therefore, a correction of the fluorescence lifetime images of the BCECF-stained ASC for the refractive index n is necessary, and thus, it is essential to determine the n gradient in the heterogeneous artificial epidermis. In FLIM experiments on ASC stained with coumarin 314, we determined the local refractive index of the artificial epidermis with a high 3D resolution. This local refractive index was used to correct the fluorescence lifetime images of BCECF-stained samples before converting them into pH-images. To our knowledge, it is the first time that an epidermal n-gradient is obtained by means of FLIM and that the fluorescence lifetime images of BCECF-stained samples are corrected for a local, i.e. not averaged,[1] refractive index before converting them into pH-images.

The 3D representation of the pH in the artificial epidermis revealed that the pH at the surface is acid (5.9) and it increases with increasing depth. At the junction between stratum corneum and stratum granulosum, a neutral pH was measured. Furthermore, we observed that the pH gradient in the cell interior and in the intercellular matrix, respectively, differ significantly.

By comparing the pH distribution, the n distribution and the morphology of the artificial skin constructs with data obtained for the genuine human skin, we can conclude that the ASC are very reliable yet simplified skin models.

5.3 Materials and Methods

5.3.1 Artificial Skin Constructs

The artificial skin constructs (ASC) consist of a collagen matrix with incorporated human dermal fibroblasts (HDF), i.e. the artificial dermis, covered by an epidermis equivalent of differentiated HaCaT (Human adult at low Calcium concentration and elevated Temperature) keratinocytes.[24] They were cultivated as described by Mueller-Goymann et al.[24]

For imaging experiments, the ASC were stained with 50 μmol L^{-1} buffer solutions ($pH = 7.15$) of coumarin 314 (C314) and *2',7'-bis(2-carboxyethyl)-5/6-carboxyfluorescein* (BCECF), respectively. Thereby, 2 mL of fluorophore solution were mixed in the growing medium of the skin constructs. Rapid staining of the ASC was attained by supplementary addition of about 5 μL DMSO. The staining process typically lasted approx. 30 minutes. During this period a sufficient concentration of chromophore was assimilated by the samples. In order to avoid

damages of the ASC, all experiments were performed within 2 h after removing them from the incubator.

Coumarin 314 (Lambda Physik), BCECF (Fluka), DMSO p.a. and buffer solutions of different pH (Merk) were used without further purification. Neither coumarin 314 nor BCECF had a noxious effect on the artificial skin constructs.

5.3.2 Methods

The two-photon scanning microscopy is a non-invasive imaging technique very suitable for the 3D-resolved investigation of the morphology of thick highly-scattering samples, e.g. the artificial skin constructs.[4,5,9] By combining this technique with fluorescence lifetime imaging, new insight in the functionality of the samples can be obtained, i.e. environmental parameters, e.g. pH, refractive index n, viscosity η or ions concentration, as well as vital cellular processes can accurately be monitored with high 3D-resolution.[12−15]

Two-photon scanning microscopy

In typical two-photon excitation microscopy (TPM) experiments, a pulsed laser beam is focused by a high-aperture microscope objective into the sample. At the sample, the fluorophore molecules, which dwell in a 3D-confined region around the focus (in the excitation volume), are simultaneously excited by two near-infrared (NIR, $700 - 1000$ nm) laser photons and consequently fluoresce, i.e. spontaneously emit a visible photon. The emitted fluorescence is registered in order to obtain information about the morphology of the studied sample.

The expansion of the excitation volume has a particular significance, since it specifies the spatial resolution of the method. The excitation volume is defined as the region around the focus, in which the excitation probability k is larger than k_0/e, whereby k_0 is the maximal excitation probability at the focal point.[8,25] Since the excitation probability k scales quadratically with the photon flux ϕ of the laser beam

$$k = \delta \cdot \phi^2 \tag{5.1}$$

the spatial dependence $k(r, z)$ can be deduced from the point-spread function $PSF(r, z)$, i.e. the unitless photon flux distribution of the focused laser beam.[8,25] In Eq. 5.1 δ represents the molecular two-photon absorption cross-section.

The diffraction-limited point spread function is well approximated in the case

of two-photon excitation by a 2D-Gaussian-Lorentzian distribution:[26]

$$PSF(r,z) = \frac{4\,\omega_0^2}{\pi^2\,\omega^2(z)} \cdot e^{-\left[4\,r^2/\omega^2(z)\right]} \qquad \text{with} \qquad \omega^2(z) = \omega_0^2 \left[1 + \left(\frac{z}{z_R}\right)^2\right]. \tag{5.2}$$

In Eq. 5.2 ω_0 is the secondary axis and z_R the principal axis of the elliptical excitation volume V_0 as defined by Mertz et al, while z and r are cylindrical coordinates.[26] The dimensions ω_0 and z_R of the excitation volume define the spatial resolution in the x-y plane perpendicular on the optical axis and in z direction, i.e. on the optical axis, respectively.

In standard confocal experiments on thick biological samples the diffraction-limited photon flux distribution $PSF(r,z)$ is broaden due to Rayleigh scattering.[25,27] Thus, the spatial resolution and the signal-to-background ratio (SBR) are deteriorated and both photodamage and photobleaching increase in the out-of-focus regions. In contrast to standard confocal experiments, in TPM experiments the excitation succeeds almost exclusively with ballistic photons, i.e. no scattered photons.[27] Thus, the diffraction-limited resolution and an excellent SBR are maintained down to $\approx$ 200 μm depth in tissue and neither photodamage nor photobleaching of the sample occur outside the focal plane.

Moreover, since the NIR light typically used in the two-photon microscopy is less absorbed by biological tissues than the UV light employed in standard confocal experiments, TPM allows a larger penetration depth into the samples and assures reduced photodamage and photobleaching.[8,25,27] A further reason for the reduced photodamage in the two-photon microscopy is the pulsed laser illumination, which implies a reduced average energy at the sample despite the large photon flux.

Hitherto, we considered single-point TPM measurements, in which only a volume V_0 (one excitation volume) at the sample is observed. In order to rapidly achieve information about the heterogeneity of the system, such single-point measurements are repeated at different positions in the sample, i.e. the sample is scanned.

Concluding, the two-photon scanning microscopy allows fast optical sectioning in thick highly-scattering tissues with a large 3D resolution and without any mechanical injury of the sample.

Fluorescence lifetime imaging

The fluorescence signal of molecules is characterised not only by intensity and wavelength, but also by time-dependent properties, e.g. fluorescence lifetime τ. The fluorescence lifetime of both exogenous and endogenous chromophores is a valuable parameter for biological investigations, since it is scarcely affected by experimental factors like chromophore concentration or fluctuations of the laser power but it is very sensitive to environmental parameters like pH, refractive index n, viscosity η or ions concentration.[12]

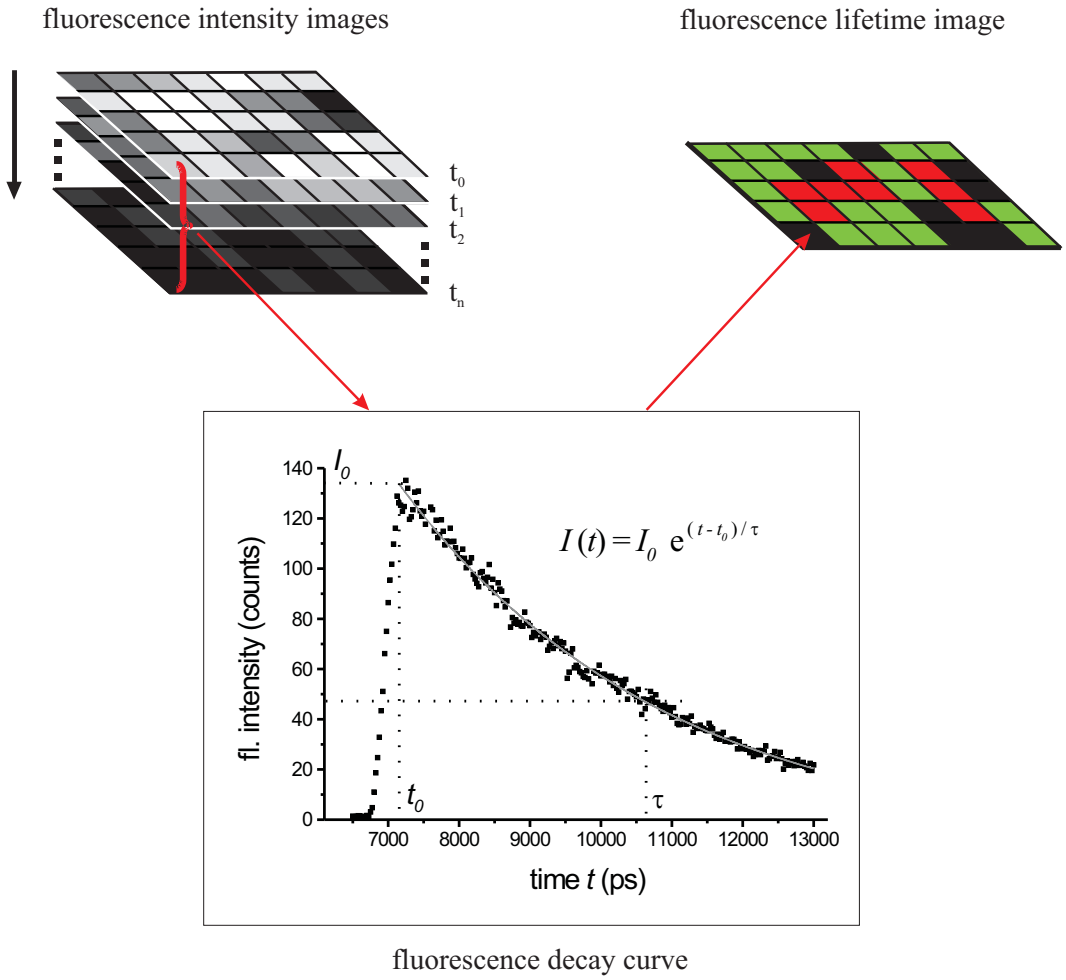

Fig. 5-1: Functional principle of FLIM in time-domain. A fluorescence lifetime image (τ-map) is generated from a series of fluorescence intensity images registered at subsequent moments t after the laser pulse t_0. The fluorescence lifetimes are calculated from the corresponding decay curves in each pixel of the image.

The fluorescence lifetime τ can be determined either in frequency domain or in time domain experiments.[14] In frequency domain, the parameter τ is calculated

from the phase difference between the laser beam and the fluorescence signal. The time domain techniques represent more direct methods to determine the fluorescence lifetime.[13] Thereby, the fluorescence intensity is registered at subsequent moments τ after an arbitrary initial time t_0, in our case after the laser pulse. Thus, a fluorescence decay curve is generated. In the simplest case, i.e. if only one chromophore fluoresces at the sample, the fluorescence decay curve can be approximated by a monoexponential function:

$$I(t) = I_0 \cdot e^{-(t - t_0)/\tau} . \tag{5.3}$$

The fluorescence lifetime τ is defined as the period until the time-dependent fluorescence intensity $I(t)$ decreases to I_0/e, whereby I_0 is the maximal fluorescence intensity immediately after the laser pulse.

In bulk τ-measurements only the average value of the fluorescence lifetime, and thus, of the environmental parameter of interest is determined. By combining the fluorescence lifetime measurement with imaging techniques, a highly-resolved spatial distribution of the fluorescence lifetime is obtained, and thus, the heterogeneous distribution of the corresponding environmental parameter in the sample can be monitored. This spatially-resolved t-measurement is referred to as fluorescence lifetime imaging (FLIM).

Analogous to standard τ-measurements, FLIM experiments can be performed either in frequency domain or in time domain. Due to its advantages, i.e. instrumental stability, rapid registration of the data and uncomplicated evaluation,[17–19] we employed in our experiments time-domain FLIM based on a time-gated technique.

In the following, the functional principle of time-domain FLIM is briefly presented. A series of fluorescence intensity images is registered at subsequent moments t after the laser pulse and, thus, in each pixel of the image a fluorescence decay curve is recorded. Since from each decay curve, a fluorescence lifetime can be determined, a fluorescence lifetime image (τ-map) of the same dimensions as the initial fluorescence intensity images is generated (see Fig. 5-1). This procedure can be repeated for different z-positions in the sample, and thus, a 3D-resolved representation of the fluorescence lifetime and of the corresponding environmental parameter can be obtained.

Experimental set-up

The basic set-up of the two-photon microscope used in our experiments is similar to set-ups previously described.[9] The characteristics of the pulsed laser beam of the Ti:Sa laser (Mira 900, Coherent) are 200 fs pulse width, 76 MHz repetition rate and 169 nJ pulse energy. The laser beam is driven by two galvanometric mirrors (GSI Lumonics) in order to scan the sample in the x-y plane. In z-direction the sample is driven by a piezoelectric stage (Physics Instruments) with a precision of 8.42 nm. A microscope objective Achroplan (63×, $NA = 0.95$, water-immersion) of the company Carl Zeiss is used to focus the tenfold extended laser beam into the sample. The dimensions of the effective two-photon excitation volume, i.e. the resolution of the microscope, are for a wavelength $\lambda = 830$ nm, $\omega_0 = 0.32$ μm in the x-y plane and $z_R = 1.35$ μm on the optical axis. The calibration was performed by means of fluorescent latex microbeads for the x-y resolution and of fluorescein-isothiocyanide-monolayers for the z-resolution.[28] The fluorescence of the sample is collected by the same microscope objective and filtered by a dichroic mirror and by a band pass filter (BG39, Schott).

As detection unit we use a time-gated system (LaVision) including a high repetition rate intensifier (HRI) with an adjustable gate ($200-1000$ ps) combined with a CCD camera (480×640 pixel). The jitter of the detection system is less than 10 ps ($8-9$ ps measured in almost noise-free FLIM experiments) at a gate width of 200 ps. A pixel on the CCD chip corresponds to 0.145 ± 0.05 μm at the sample. The dwell time of the laser beam per pixel during one scan is 0.95 μs. The size of the scanned field was 49×54 μm^2 and 50×51 μm^2, respectively. 21 fluorescence intensity images (3 s/frame) were registered at subsequent delays after the pulse in steps of 200 ps to generate the τ-images.

The mean laser power at the sample was less than 3 mW, which assures that neither functional nor morphological modifications of the tissue occur under NIR photostress.[9,18] Under these experimental conditions the autofluorescence background of the ASC amounts to less than 0.1% of the registered signal.

5.4 Results and Discussion

5.4.1 Two-photon Scanning Microscopy in ASC

In this section, the advantages of TPM, i.e. reduced photodamage and no mechanical injury of the sample coupled with a high 3D-resolution and a large penetration depth, are demonstrated on the example of artificial skin constructs. Moreover, by comparing the morphology of the ASC with that of human skin, the suitability of artificial skin as a model for genuine human skin is verified.

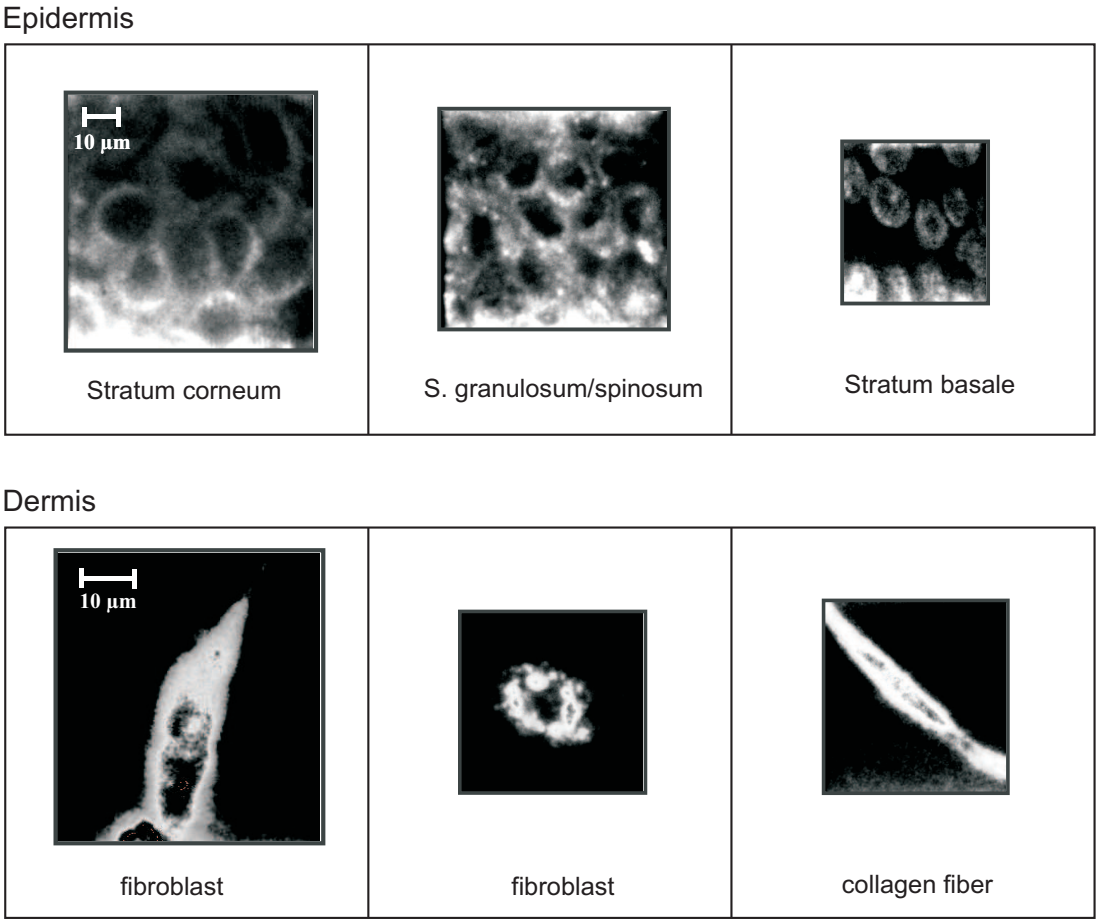

Fig. 5-2: TPM fluorescence intensity images of different layers in the artificial skin constructs stained with coumarin 314 or rhodamin B. The images of the epidermal layers were taken in 7, 14 and 30 μm depth, while dermal structures were visualised in $50 - 70$ μm depth.

We succeed in imaging the main segments of the ASC, i.e. epidermis and dermis, by employing two-photon scanning microscopy. The maximal penetration

depth, i.e. the depth in the intact ASC, at which fluorescing structures can still be visualised, was about 170 μm.

In the artificial epidermis, three layers of differentiated keratinocytes could be identified. Starting from the surface, they correspond to stratum corneum (thickness $8-10$ μm), stratum granulosum/spinosum (thickness $15-20$ μm) and stratum basale (thickness $5-8$ μm). The dimension of the keratinocytes is $5-7$ μm in stratum basale, $8-10$ μm in stratum granulosum/spinosum and $12-15$ μm in stratum corneum (see Fig. 5-2). In the human skin, the dimension of the keratinocytes amounts to $25-30$ μm in stratum corneum, $10-15$ μm in stratum granulosum/spinosum and ≈ 7 μm in stratum basale (abdominal region, female 45). The thickness of the human epidermis varies between 50 μm on the eyelids and 1.5 mm on the palms and soles.[5] Thus, the artificial and the human epidermis have similar morphologies, but the epidermal strata in the ASC are less developed as compared to those of human skin.

The artificial dermis consists of a matrix of collagen fibers with incorporated human dermal fibroblasts (see Fig. 5-2). The collagen fibers are $3-5$ μm thick while the fibroblasts are $25-30$ μm long and have a maximal cross section of 15 μm. Although the morphology of the human dermis is more complex than that of the artificial dermis,[3,5–7] the main dermal structures are met both in the artificial and in the human skin.

Concluding, as far as the morphology is concerned, the artificial skin constructs are simplified yet reliable models of the genuine human skin.

5.4.2 Fluorescence Lifetime Imaging in ASC

The two-photon scanning microscopy enabled a detailed study of the morphology of the ASC. However, no information about the acidic mantle (pH gradient) of the artificial epidermis, and thus, about its barrier function could be achieved.

TPM-FLIM experiments on skin constructs stained with BCECF first allowed the investigation of the pH gradient of the artificial epidermis with subcellular resolution and without damaging the samples. BCECF was selected as pH indicator in the FLIM experiments because its fluorescence lifetime strongly depends on the pH. At aicidic pH ($pH \approx 2$) BCECF is protonated (HBCECF), while at basic pH ($pH \approx 12$) it is unprotonated ($BCECF^-$). The fluorescence lifetimes of the protonated and unprotonated species differ significantly.[11] At pH values between these two extremes, both HBCECF and $BCBCF^-$ are present in solution, contribute to the fluorescence signal and, thus, influence the fluorescence lifetime.

Especially for biological investigations, BCECF is the ideal pH indicator because its p_{Ka} amounts to 7.0 and it is not noxious for tissues.

We measured the dependence of the fluorescence lifetime of eight BCECF buffer solutions of pH between 1.83 and 12.44 in order to generate a calibration curve which will be later used to convert the τ-images of the epidermal layers into pH-images (see Fig. 5-3). At $pH = 1.83$, at which only HBCECF is present in the solution, τ amounts to 2491 ± 20 ps, while at $pH = 12.44$, at which BCECF is completely unprotonated (only $BCECF^-$), τ amounts to 3621 ± 17 ps. In the pH-range of interest, i.e. between $pH = 4$ and $pH = 8$, the fluorescence lifetime of BCECF varies between 2524 ± 22 ps and 3521 ± 15 ps (1000 ps dynamic range). The fluorescence lifetimes were determined in monoexponential FLIM experiments on buffer solutions of BCECF. The standard deviation of about 20 ps in the determination of the fluorescence lifetime corresponds to an accuracy of the pH determination of less than 0.05%.

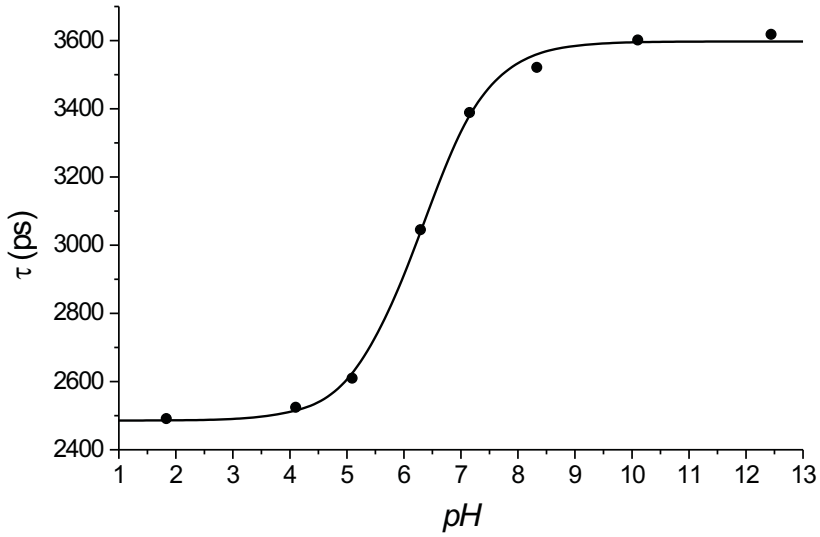

Fig. 5-3: Dependence of the fluorescence lifetime τ of BCECF (pH indicator) on the pH. The calibration was performed with aqueous buffer solutions of BCECF (refractive index $n = 1.33$).

The calibration curve $\tau(pH)$ (Fig. 5-3) alone does not allow an accurate conversion of the τ-images of the epidermal layers into pH-images, because the fluorescence lifetime of BCECF may also be influenced by other factors, i.e. refractive index, viscosity and ions concentration, which are expected to be different in aqueous solution and in the artificial skin samples. We observed that the flu-

orescence lifetime of BCECF depends neither on the viscosity nor on the ions concentration (data not shown). As far as the dependence of the fluorescence lifetime τ on the refractive index n is concerned, it has been demonstrated that Eq. 5.4 is valid for all substances including BCECF.[29]

$$\tau^{-1} = 2.88 \cdot 10^{-9} \cdot n^2 \int \varepsilon \frac{(2\nu_0 - \nu)^2}{\nu} d\nu \,. \tag{5.4}$$

Hereby, ε is the extinction coefficient at the frequency ν and ν_0 is equivalent to the frequency of the ground-state to the first singlet-state transition.

In order to accurately convert τ-images into pH-images by means of the calibration curve $\tau(pH)$, the τ-images must be first corrected for the corresponding refractive index. Thus, the determination of the n gradient in the artificial epidermis is essential. For this purpose, FLIM experiments in ASC stained with coumarin 314 were performed. Coumarin 314 is an adequate n-indicator because its fluorescence lifetime is influenced only by the refractive index (data not shown). The fluorescence lifetime of C314 in aqueous solution ($n = 1.33$) was determined to be 3453 ± 15 ps.

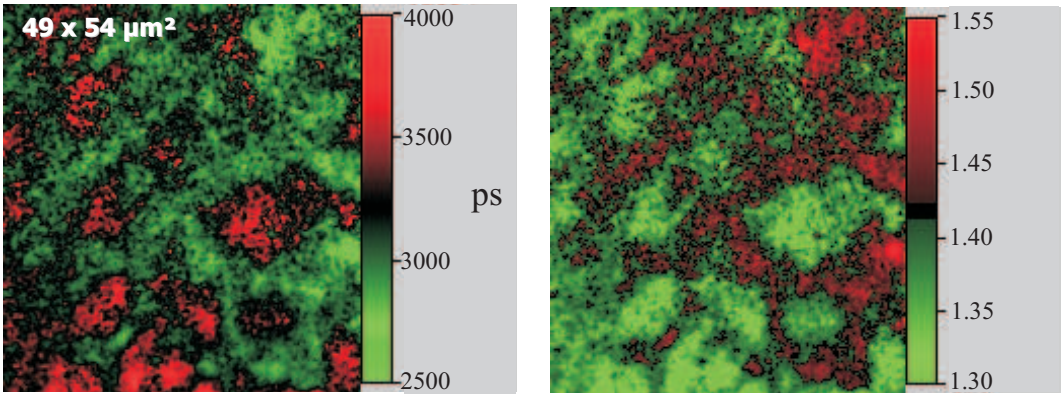

Fig. 5-4: Fluorescence lifetime image (τ-map) and corresponding refractive index image (n-map) of an epidermal layer ($depth = 3.7$ µm) in stratum corneum. The refractive index in the cell interior ($n = 1.34$) is significantly smaller than in the intercellular matrix ($n = 1.47$) due to a larger lipid content of the latter. The artificial skin sample was stained with an aqueous solution of coumarin 314 (50 µmol L^{-1}).

As it results from Eq. 5.4, the fluorescence lifetime τ scales inversely proportional to the square of the refractive index n. Using this relation, τ-images of the artificial epidermis stained with coumarin 314 were converted into n-images

as exemplified in Fig. 5-4. In this way, the three-dimensional gradient of the refractive index n in the artificial epidermis was ascertained.

The τ-images of the artificial epidermis stained with BCECF can be now corrected for the corresponding refractive index and directly converted into pH-images using the calibration curve $\tau(pH)$ (Fig. 5-3) as exemplified in Fig. 5-5. Thus, the exact 3D-distribution of the pH in the artificial epidermis is obtained.

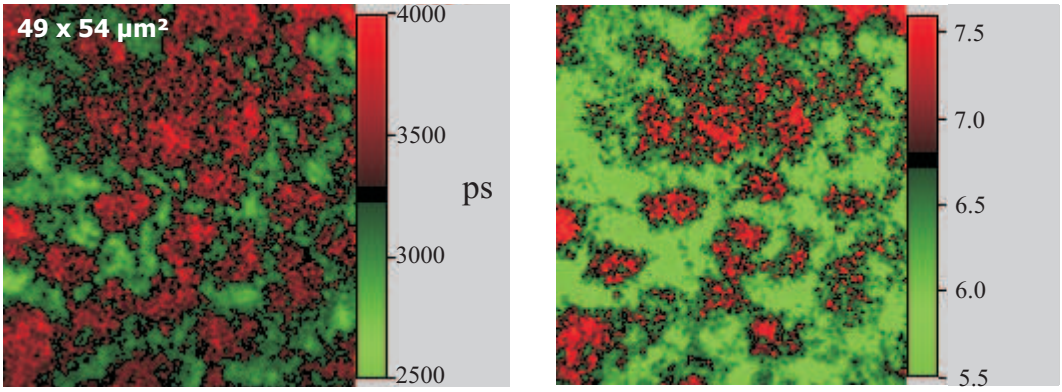

Fig. 5-5: Fluorescence lifetime image (τ-map) corrected for n and corresponding pH-image (pH-map) of an epidermal layer ($depth = 13.48$ μm) in stratum granulosum/spinosum. The pH in the cell interior ($pH = 7.2 \pm 0.1$) is significantly larger than in the intercellular matrix (pH = 6.3 0.2). The artificial skin sample was stained with a 50 mol L-1 buffer solution (pH = 7.15) of BCECF.

The correction of τ-images of samples stained with BCECF for the refractive index n has already been applied by other scientists to convert the τ-images into pH-images.[1,2] However, this correction was not accurately performed since a refractive index averaged over the whole sample was employed. To our knowledge, we determined for the first time a 3D n-gradient by means of FLIM and corrected the τ-images with the corresponding refractive index in order to accurately convert τ-images into pH-images.

n-Imaging

Fluorescence lifetime images (τ-maps) of 13 equidistant epidermal layers were generated down to 40 μm depth in the epidermis of artificial skin samples stained with C314. These τ-maps were converted into n-images using Eq. 5.4 as described in the previous section.

In the upper layers ($0 - 10$ μm), i.e. stratum corneum, the refractive index of the cells is clearly smaller ($n = 1.34 \pm 0.01$) than that of the intercellular matrix (n between 1.48 and 1.38) due to the higher lipid content of the latter (Fig. 5-4). At the surface ($z = 0$ μm) the lipid matrix dominates also the cell interior and this results in an uniform distribution of the refractive index ($n = 1.48 \pm 0.01$). In the deeper layers, i.e. beyond the junction between stratum corneum and stratum granulosum, there are no noticeable differences between the cell interior and the intercellular matrix as far as the refractive index is concerned ($n = 1.35 \pm 0.01$), because both the cell interior and the intercellular matrix consist mostly of water.

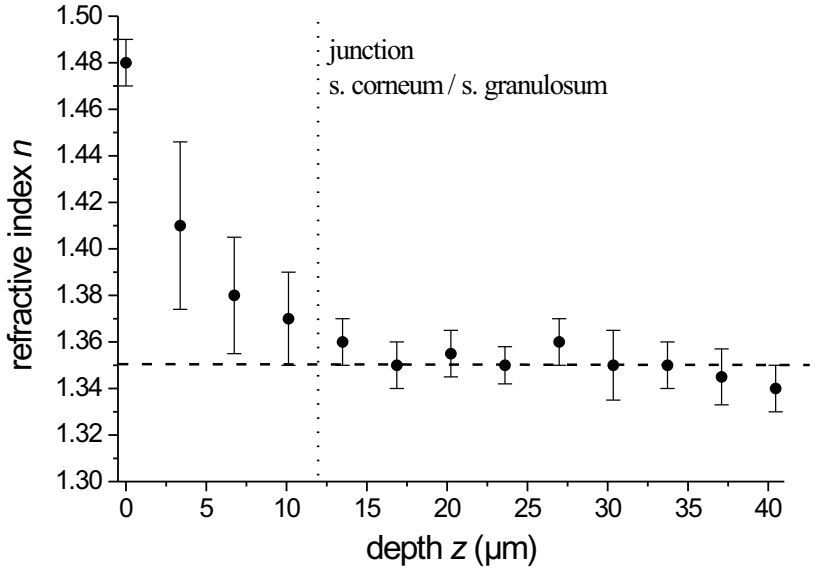

Fig. 5-6: Dependence of the refractive index n on the z-position of the epidermal layer in ASC stained with C314. The refractive index was integrated over a 49×54 μm^2 n-image. The error bars represent the variation of the refractive index within an image. They are very large in stratum corneum because the differences between n in the cell interior and in the intercellular matrix, respectively, are also very large. As expected, the error bars are small beyond the junction between stratum corneum and stratum granulosum (below 12 μm).

Fig. 5-6 provides an overview of the dependence of the refractive index n on the z-position of the epidermal layer, whereby the refractive index was averaged over the 49×54 μm^2 n-image. In stratum corneum ($0 - 10$ μm) the decreasing lipid content induces a decrease of the averaged refractive index from 1.48 ± 0.01 to 1.37 ± 0.02. In the deeper layers (below 12 μm) the averaged refractive index reaches a constant value of 1.35 ± 0.01, which is slightly larger than that of water

($n = 1.33$).

Different methods, e.g. confocal Raman microspectroscopy or bifocal optical coherence refractometry, have been employed to determine the refractive index distribution in the epidermis of human skin.[30–32] In stratum corneum the refractive index n varies between 1.6 and 1.37 depending on body site and sex and it is maximal at the surface and minimal at the junction between stratum corneum and granulosum.[30–32] In the deeper strata the refractive index n is a constant slightly larger than that of water.[30–32] Concluding, as far as the refractive index is concerned, the ASC are very similar to the genuine human skin.

In the following, the results obtained in the FLIM experiments in ASC stained with C314 will be used to correctly convert the fluorescence lifetime images of the artificial epidermis stained with BCECF into pH-images.

pH-Imaging

Since the barrier function of the artificial epidermis is closely connected to its acidic mantle, the investigation of the 3D pH gradient in the epidermal strata is essential to demonstrate the applicability of the ASC as models of the genuine human skin in permeability studies. Therefore, in FLIM experiments on artificial skin samples stained with BCECF, τ-images of 14 epidermal layers were generated down to 30 μm depth. These τ-images were first corrected for corresponding refractive index n and then converted into pH-images by means of the calibration curve $\tau(pH)$ (Fig. 5-3) as previously described.

Differences between the pH of the cell interior (between 6.0 and 7.2) and of the intercellular matrix (between 5.8 and 6.6) are observed all through the artificial epidermis. As exemplified in Fig. 5-5, the pH of the cell interior in 13.48 μm depth amounts to 7.2 ± 0.1 (averaged over 6 cells), while the pH of the intercellular matrix is 6.3 ± 0.2 (averaged over 7 regions). Only at the surface ($z = 0$ μm), both the cells and the intercellular matrix are characterised by the same acidic pH of 5.9 ± 0.1.

In Fig. 5-7 the dependence of the pH on the z-position of the epidermal layer is schematically plotted. The pH of the cell interior rapidly increases in stratum corneum (0 to 10 μm) from 6.0 to 7.2 and remains constant ($pH = 7.2$) in the deeper layers beyond the junction between stratum corneum and granulosum (below 12 μm). An increasing tendency shows also the pH of the intercellular matrix. However, in this case the pH increases all through the epidermis (depth z between 0 and 30 μm) and does not exceed a value of 6.6 ± 0.1. Qualitatively,

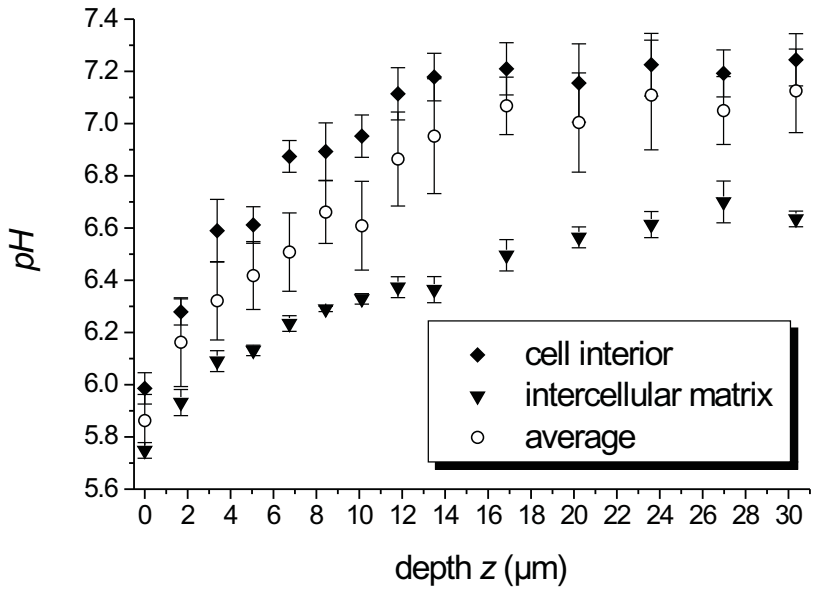

Fig. 5-7: Dependence of the pH on the z-position of the epidermal layer in ASC stained with BCECF. The error bars represent the variation of the pH in the cell interior, the intercellular matrix and within the 49×54 μm^2 pH-image, respectively. In all the cases, the pH increases with increasing depth z.

the profile of the pH averaged over a pH-image is similar to the pH-gradients in the cell interior and in the intercellular matrix, respectively (Fig. 5-7).

Fig. 5-8 shows fluorescence lifetime maps of epidermal layers in the BCECF-stained ASC in 10 different depths z. Since the fluorescence lifetime of BCECF increases with increasing pH, these images are the 3D -visualisation of the epidermal pH, i.e. the acidic mantle.

Previous pH-measurements revealed that the stratum corneum of genuine human skin has an acidic pH, which is minimal at the surface and increases with the depth.[1,2] The pH at the surface of stratum corneum ranges between 4.5 and 6.0 depending upon body site, sex and species.[1] Furthermore, it was shown that the pH of the viable epidermis is neutral (7.0), while that of the viable cells amounts to ≈ 7.2.[1,2] Considering these results, we can conclude that the ASC have a similar acidic mantle as the genuine human skin, supporting the usefulness of ASC in permeability studies. A 3D pH gradient in the human epidermis, which would allow an accurate comparison of the acidic mantles, has not been measured yet.

pH-measurements similar to ours have been performed by means of FLIM on

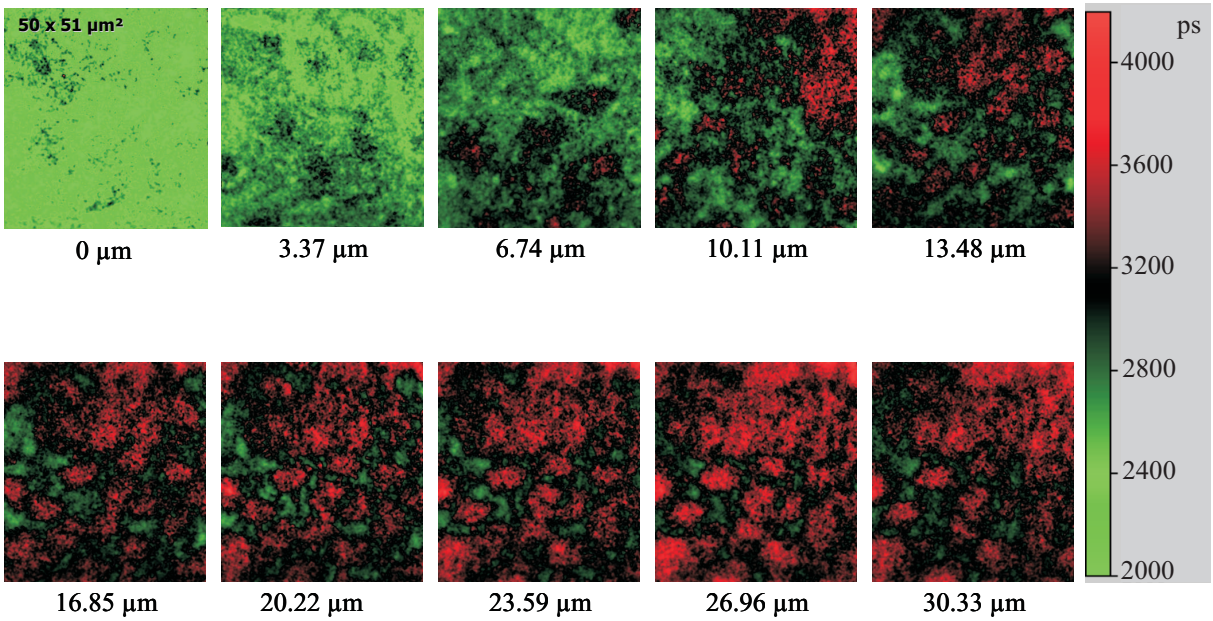

Fig. 5-8: Dependence of the fluorescence lifetime τ of BCECF on the z-position of the epidermal layer. Since the fluorescence lifetime of BCECF increases with increasing pH, this series of images emphasises once more the 3D pH gradient in the artificial epidermis. The z-position is denoted under each image.

mouse skin samples. However, these experiments are not reliable since in the evaluation of the pH-images, the value of the refractive index was considered to be 1.38 all over the epidermis, i.e. the differences in refractive index between cell interior and intercellular matrix and between the different depth positions of the epidermal layers, respectively, were completely neglected.

5.5 Conclusions

We studied for the first time in detail the acidic mantle, i.e. the pH gradient, of the epidermis of artificial skin constructs by means of fluorescence lifetime imaging combined with two-photon scanning microscopy. Such an investigation is of particular significance because the epidermal acidic mantle plays a central role to the barrier function, i.e. selective permeability, of the skin. Thus, by comparing the pH distribution of the artificial and genuine epidermis, respectively, assertions about the reliability of the ASC as human skin models in permeability studies can be made.

In FLIM experiments on ASC stained with BCECF, a 3D representation of the

epidermal pH was obtained, which revealed that, similarly to the genuine skin, the surface of the artificial epidermis has an acidic character ($pH = 5.9$). Moreover, the pH rapidly increases in stratum corneum up to neutral pH (7.0) and remains constant in the deeper epidermal layers. We have also observed that the pH increase in the stratum corneum is more pronounced in the cell interior than in the intercellular matrix. Beyond the junction between stratum corneum and granulosum, the pH of the cell interior remains constant ($pH = 7.2$), while the pH of the intercellular matrix continues to increase but does not exceed a value of 6.6. These results lead to the conclusion that, as far as the acidic mantle is concerned, the ASC and the genuine human skin are similar yet not identical, and thus, the ASC are reliable skin models for permeability experiments. Furthermore, the results of experiments, in which the morphology and the refractive index gradient of the artificial epidermis was studied, validate the eligibility of the ASC as skin models.

References

[1] K.M. Hanson, M.J. Behne, N.P. Barry, T.M. Mauro, E. Gratton, R.M. Clegg, *Biophys. J.* **2002**, 83, 1682-1690

[2] M.J. Behne, J.W. Meyer, K.M. Hanson, N.P. Barry, S. Murata, D. Crumrine, R.W. Clegg, E. Gratton, W.M. Holleran, P.M. Elias, T.M. Mauro, *J. Biol. Chem.* **2002**, 277, 47399-47406

[3] P. Corcuff, J.-L. Leveque, *Dermatology* **1993**, 186, 50-54

[4] B.R. Masters, P.T.C. So, E. Gratton, *Ann. N.Y. Acad. Sci.* **1998**, 838, 58-67

[5] B.R. Masters, P.T.C. So, E. Gratton, *Biophys. J.* **1998**, 72, 2405-2412

[6] K. König, U. Wollina, I. Riemann, C. Peuckert, K.-J. Halbhuber, H. Konrad, P. Fischer, V. Fünfstück, T. Fischer, P. Elsner, *SPIE* **2002**, 4620, 191-201

[7] P.T.C. So, H. Kim, I.E. Kochevar, *Opt. Exp.* **1998**, 3, 339-350

[8] W. Denk, J.H. Strickler, W.W. Webb, *Science* **1990**, 248, 73-76

[9] K. König, *J. Microscopy* **2000**, 200, 83-104

[10] E. Gratton, N.P. Barry, S. Beretta, A. Celli, *Methods 00* **2001**, 103-110

[11] H. Szmacinski, J.R. Lakowicz, *Anal. Chem.* **1993**, 65, 1668-1674

[12] J.R. Lakowicz, K. Berndt, *Rev. Sci. Instrum.* **1991**, 62, 1727-1734

[13] W. Becker, A. Bergmann, www.becker-hickl.de/pdf/tcvgbhl.pdf **2003**

[14] A. Draaijer, R. Sanders, H.C. Gerritsen, Handbook of biological confocal microscopy, J. Pawley, Plenum Press, New York, p. 491-505, **1995**

[15] J.R. Lakowicz, H. Szmacinski, M.L. Johnson, *J. Fluorescence* **1992**, 2, 47-62

[16] S. Murata, P. Herman, J.R. Lakowicz, *Cytometry* **2001**, 43, 94-100

[17] D. Elson, S. Webb, J. Siegel, K. Suhling, D. Davis, J. Lever, D. Phillips, A. Wallance, P. French, *Opt. Photon. News* **2002**, 27-32

[18] R. Niesner, B. Peker, P. Schlüsche, K.-H. Gericke, *Chem. Phys. Chem* **2004**, 8, 1141-1149

[19] V. Barzda, C.J. Grauw, J. Vroom, F.J. Kleima, R. van Grondelle, H. van Amerongen, H.C. Gerritsen, *Biophys. J.* **2001**, 81, 538-546

[20] A. Squire, P.J. Verveer, P.I.H. Bastiaens, *J. Microscopy* **2000**, 197, 136-149

[21] P.J. Verveer, A. Squire, P.I.H. Bastiaens, *Biophys. J.* **2000**, 78, 2127-2137

[22] E. Gratton, S. Breusegem, J. Sutin, Q. Ruan, N. Barry, *J. Biomed. Opt.* **2003**, 8, 381-390

[23] W. Becker, A. Bergmann, C. Biskup, T. Zimmer, N. Klcker, K. Benndorf, Proc. *SPIE* **2002**, 4620

[24] A. Winkler, C.C. Müller-Goymann, *Eur. J. Pharm. Biopharm.* **2002**, 53, 281-287

[25] X. Deng, X. Gan, M. Gu, *J. Appl. Phys.* **2002**, 91, 4659-4665

[26] J. Mertz, C. Xu, W.W. Webb, *Opt. Lett.* **1995**, 20, 2532-2534

[27] H. Szmacinski, I. Gryczynski, J.R. Lakowicz, *Biospectroscopy* **1998**, 4, 303-310

[28] A. Schönle, M. Glatz, S.W. Hell, *Appl. Opt.* **2000**, 39, 6306-6311

[29] S.J. Strickler, R.A. Berg, *J. Chem. Phys.* **1962**, 37, 814-822

[30] P.J. Caspers, G.W. Lucassen, E.A. Carter, H.A. Bruining, G.J. Puppels, *J. Invest. Derm.* **2001**, 116, 434-442

[31] A.V. Zvyagin, K.K.M.B. Dilusha Silva, S.A. Alexandrov, T.R. Hillman, J.J. Armstrong, *Opt. Exp.* **2003**, 25, 3503-3517

[32] S.A. Alexandrov, A.V. Zvyagin, K.K.M.B. Dilusha Silva, D.D. Sampson, *Opt. Exp.* **2003**, 2, 117-119

Chapter 6

Non-iterative Biexponential Fluorescence Lifetime Imaging in the Investigation of Cellular Metabolism by means of NAD(P)H Autofluorescence

6.1 Abstract

The cofactors NADH and NADPH, hereafter NAD(P)H, belong to the principal endogenous indicators of the energetical cellular metabolism. Since the metabolic activity of cells is given by the ratio between the concentrations of free and protein-bound NAD(P)H, the development of autofluorescence techniques, which accurately restore the modifications of this ratio is particularly significant. Hitherto, the methods applied in the monitoring of cellular metabolism provided either imprecise results due to interferences of the NAD(P)H signal with perturbing factors or necessitate a complicated internal calibration. We employ biexponential fluorescence lifetime imaging (FLIM) in order to discriminate between the free and protein-bound NAD(P)H without any previous calibration. Thus, we obtain directly for the first time a high-resolution map of the cellular metabolism, i.e. the image of the contribution of the protein-bound NAD(P)H to the cumulative NAD(P)H fluorescence signal. Moreover, we demonstrate that the protein-NAD(P)H complexes characterised by different fluorescence lifetimes are not uniformly distributed all over the cell, as assumed until now, but concentrated in certain cellular regions. The different fluorescence lifetimes indicate either different protein-NAD(P)H complexes or different strengths of the bond between NAD(P)H and protein in these complexes.

Since an important aspect in biological applications is to monitor the dynamics of the relevant processes like the cellular metabolism, rapid dynamical techniques, i.e. rapid biexponential fluorescence lifetime imaging, are needed. In this frame, a necessary step is to reduce as much as possible the evaluation effort. Most of the evaluation techniques in multiexponential FLIM are time-expensive iterative methods. The few exceptions are connected with loss on information, e.g. global analysis, or loss on accuracy, e.g. the rapid evaluation technique (RLD). We implement for the first time in FLIM the non-iterative non-restrictive method originally developed by Prony for approximations of multiexponential decays. The accuracy of this method is verified in biexponential FLIM experiments in time-domain on mixtures of two chromophores both in homogenous and in heterogeneous media. The resulting fluorescence lifetimes agree within the error margins with the lifetimes of the pure substances determined in monoexponential FLIM experiments. The rapidity of our evaluation method as compared to iterative pixel-by-pixel methods is evidenced by a reduction of the evaluation time by more than one order of magnitude. Furthermore, the applicability of this method for the biosciences is demonstrated in the investigation of the cellular metabolism by means of NAD(P)H endogenous fluorescence.

6.2 Introduction

Since a central aim of the biosciences is to simulate the real environmental conditions of biological systems in order to gain a true image of the processes of interest, the development of techniques which apply tissue autofluorescence, i.e. non-labelling techniques, is particularly important.[1−9] Endogenous chromophores which contribute to tissue intrinsic fluorescence are haemoglobin, reduced nicotinamide adenine dinucleotides (NADH and NADPH), oxidised flavoproteins, serotonin, collagen, elastin etc.[1−9] As indicators of the energetical metabolism the cofactors NADH and NADPH, hereafter NAD(P)H, belong to the principal topics of many research works.[1,4,5,7−11]

Despite the low two-photon absorption cross-section of most chromophores, two-photon microscopy (TPM) is adequate for studies which necessitate submicron three-dimensional (3D) resolution, large penetration depth in highly scattering media and low photodamage of the sample outside the focal plane, i.e. studies of biological systems.[7,8,12] In the investigations of cellular NAD(P)H-fluorescence TPM proved to have an additional advantage over the common confocal one-

photon microscopy due to the reduced out-of-focus photobleaching effect.[8]

If the cofactors NADH and NADPH are employed as signal mediators, the cellular metabolic redox state is directly indicated by the ratio between the relative concentration of free NAD(P)H and of NAD(P)H involved in metabolic processes.[4,5,7,10,11] Consequently, the development of techniques, which accurately restore the variations of this ratio, i.e. the modifications of the cellular metabolism, is particularly important.

To the first and most common methods employed in the investigation of cellular metabolism belongs the redox fluorimetry, in which the cumulative autofluorescence steady state signal of NAD(P)H (both free and protein-bound NAD(P)H) is registered.[4,5,8] Basing on the different absorption resp. emission spectra of the two NAD(P)H states, the variations of the cumulative NAD(P)H signal are attributed to modifications of the concentration of free resp. protein-bound NAD(P)H and, thus, to modifications of the cellular redox state.[4,5] However, the registered signal is influenced not only by changes of NAD(P)H concentration but also by other factors like light scattering, instrumental instability, sample movement or non-specific background fluorescence originating from other biomolecules.[8] Thus, employing redox fluorimetry only qualitative imprecise assertions about the metabolic cellular state can be made.[8] Contrary to standard redox fluorimetry, in the ratiometric redox fluorimetry the fluorescence signal of each species, i.e. of both free and protein-bound NAD(P)H, can separately be registered and analysed and, thus, an accurate assertion about the metabolic state can be made.[8] However, due to the complicated internal calibration of the set-up[8] and to the ill-defined spectra[13] of the protein-bound NAD(P)H, the ratiometric redox fluorimetry has never been used in the investigation of cellular metabolism by means of endogenous NAD(P)H fluorescence.

A versatile alternative to the fluorimetrical techniques represents the fluorescence lifetime imaging (FLIM), a method which is based on the time-resolved registration of the fluorescence signal.[13–15] The advantages of this method have been demonstrated both in labelling[16–20] as well as in non-labelling experiments.[21–28] Employing FLIM a very good contrast between the two NAD(P)H states can easily be obtained since the fluorescence lifetimes of the free NAD(P)H ($\approx$ 400 ps) resp. protein-bound NAD(P)H ($\approx$ 2000 ps) differ significantly.[7,10,11]

In most FLIM experiments based on NAD(P)H autofluorescence the registered cumulative fluorescence decay is approximated by a monoexponential function.[9–11] Thereby, a decrease of the resulting fluorescence lifetime indicates

an increase of the free NAD(P)H concentration and, thus, a slower metabolic activity of the cells. However, this method has two major drawbacks. First, the cumulative NAD(P)H fluorescence decay deviates considerably from the monoexponential behaviour as we observed in our experiments, and, thus, a monoexponential approximation is inappropriate. Secondly, the changes in the fluorescence decay are caused not only by variations of free resp. protein-bound NAD(P)H concentrations but also by laser power fluctuations, light scattering and background noise.

The approximation of the cumulative NAD(P)H fluorescence decay with a stretched exponential function solves only the first problem.[29] Employing biexponential FLIM both disadvantages of monoexponential FLIM are counteracted: the cumulative NAD(P)H fluorescence decay is correctly approximated and the two NAD(P)H states are resolved so that the effect of interest, i.e. modifications of the free resp. protein-bound NAD(P)H concentrations, is separated from the effects of other perturbing factors. Although suggested by other authors,[9,10] to our knowledge biexponential NAD(P)H autofluorescence lifetime imaging has not been performed until now.

We performed biexponential FLIM combined with two-photon scanning microscopy in artificial skin constructs in order to study the cellular metabolism of dermal fibroblasts by means of NAD(P)H endogenous fluorescence. A typical result of such an experiment includes three images: the τ_1-map, i.e. the fluorescence lifetime image of the free NAD(P)H, the τ_2-map, i.e. the fluorescence lifetime image of the protein-bound NAD(P)H and the ratio-map which mirrors the contribution of protein-bound NAD(P)H to the cumulative NAD(P)H fluorescence signal. While the τ_1-map is a verification of the correctness of the experiment (the lifetime values should be ≈ 400 ps), the other two images reveal novel insight into the cellular metabolism. As will be demonstrated later, the τ_2-map shows that different NAD(P)H-protein complexes characterised by different fluorescence lifetimes are not uniformly distributed all over the cell as assumed until now[9] but concentrated in certain cellular regions. The ratio-map allows a direct and accurate monitoring of the modifications of free resp. protein-bound NAD(P)H content and, thus, of the cellular energetical state as we verify in experiments in which the metabolic activity of fibroblasts under NIR photostress is probed.

An important aspect in the study of biological systems is to monitor the dynamics of the processes of interest, e.g. cellular metabolism. However, due to

the extreme evaluation effort, the performance of fast dynamical multiexponential FLIM experiments has failed until now.

To the principal methods of measuring the fluorescence decay time in an image belong the frequency-domain techniques and the time-domain techniques, e.g. time correlated single photon counting (TCSPC) and time-gated procedures.[13,30] In the frequency domain the multiple-frequency FLIM (mfFLIM) associated with time-expensive iterative pixel-by-pixel Levenberg-Marquadt approximations was one of the first procedures employed to perform multiexponential FLIM.[23] A reduction of the evaluation effort was attained by means of global analysis techniques[24] combined with both mfFLIM and sfFLIM (single frequency FLIM),[31] however, with the limitation of an invariant fluorescence lifetime all over the τ-image.

The evaluation in the multiexponential FLIM in time-domain is typically performed by means of time-expensive iterative methods, e.g. non-linear Marquadt methods.[25,26,29,32] An alternative non-iterative rapid evaluation technique (RLD) for mono- and biexponential decays was developed by Ashworth.[33–35] However, this method is restricted to a reduced number of data points (4 for biexponential approximations),[33] which leads to imprecise results.[36] We performed biexponential FLIM experiments on homogenous mixtures of two dyes and determined their fluorescence lifetimes by means of RLD. The resulting lifetimes deviated constantly by more than 50% from the fluorescence lifetimes of the pure dyes measured in monoexponential FLIM experiments. Thus, RLD is not adequate as an evaluation method for biexponential FLIM and cannot be applied to multiexponential FLIM.

In order to achieve a rapid and accurate evaluation we implemented for the first time in FLIM the numerical method originally developed by Prony for multiexponential non-iterative approximations.[37,38] The accuracy of this method was verified in biexponential FLIM experiments in the time domain on mixtures of two substances both in homogenous as well as in heterogeneous media. The resulting fluorescence lifetimes generally deviate by less than 5% from the lifetimes of the pure substances determined in monoexponential FLIM experiments. The rapidity of our evaluation method as compared to iterative pixel-by-pixel methods is evidenced by a reduction of the evaluation time by more than one order of magnitude.

Multiexponential non-iterative approximation techniques[39,40,41] similar to the Prony method have already been employed in the evaluation of fluorescence decays in non-imaging experiments.

6.3 Non-iterative Multiexponential FLIM Evaluation

The fluorescence intensity decay often deviates from the monoexponential behaviour, e.g. the cumulative cellular NAD(P)H fluorescence decay. Thus, in order to resolve the components in a mixture by means of FLIM, it is favourable to approximate the time-dependent fluorescence intensity $F'(t)$ in each pixel by a multiexponential function, i.e. with a sum of n exponential decays:

$$F'(t) = b + \sum_{i=1}^{n} a_i \cdot e^{-(t-t_{in})/\tau_i} + \varepsilon(t) \tag{6.1}$$

with the baseline b, the prefactors a_i of the exponential decays, the corresponding lifetimes τ_i, the zero-point of the multiexponential decay t_{in} and noise of experimental method $\varepsilon(t)$. Since under ceratin circumstances the baseline b can be determined before the evaluation, the fluorescence signal becomes:

$$F(t) = \sum_{i=1}^{n} a_i \cdot e^{-(t-t_{in})/\tau_i} + \varepsilon(t)\,. \tag{6.2}$$

In our experiments the averaged baseline b is measured by registering the signal of the sample immediately before the laser pulse.

A rapid and accurate modality to approximate the function $F(t)$ and, thus, to determine the fluorescence lifetimes τ_i and the corresponding prefactors a_i in the time domain is given by the method originally developed by Prony in order to distinguish between a biexponential and a triexponential function, which are almost identical in a small interval.[37,38] This method requires the data points $(t_0\,, F_0)\,, (t_1\,, F_1)\,, \ldots\,, (t_m\,, F_m)$ to be equidistant, whereby the time interval between two consecutive points is Δt.[37] Considering that $t_k = k \cdot \Delta t$, we can write:

$$F_k = \sum_{i=1}^{n} \left(a_i \cdot e^{t_{in}/\tau_i}\right) \left(e^{-\Delta t/\tau_i}\right)^k = \sum_{i=1}^{n} c_i \cdot v_i^k \tag{6.3}$$

for $k = 0\,, 1\,, \ldots\,, m$. Thus, for a n-exponential decay we obtain a non-linear set of m equations with $2n$ unknown variables, c_i and v_i.[37]

In order to determine the variables v_i, a n^{th} rank polynomial with the roots v_i is used as intermediate step:[37]

$$\prod_{i=1}^{n} (v - v_i) = s_n + \sum_{i=1}^{n} s_{n-i} \cdot v_i = \varphi(v) \tag{6.4}$$

with s_i the unknown prefactors of the n^{th} rank polynomial and $s_0 = 1$.

If multiplying all $\varphi(v_i)$ with the corresponding c_i and adding the resulting expressions, we obtain:

$$\sum_{i=1}^{n} c_i \cdot \varphi(v_i) = F_n + \sum_{i=1}^{n} s_i \cdot F_{n-i} = 0\,. \tag{6.5}$$

This multiplication can be repeated with $c_i \cdot v_i$, $c_i \cdot v_i^2$, ..., $c_i \cdot v_i^{m-n}$ and yields a set of $m - n + 1$ equations with n unknown variables, s_i:[37]

$$\sum_{i=1}^{n} s_i \cdot F_{n+j-i} = -F_{n+j} \tag{6.6}$$

with $j = 0\,, 1\,, \ldots\,, m - n$.

In this step the unknown variables v_i are transformed in the new variables s_i. If the condition $m - n + 1 > n$ is satisfied, the upper set of equations is over-determined and the unknown values s_i can be obtained by means of the linear least-squares method. By solving the polynomial equation $\varphi(v) = 0$ the values v_i are determined. The equation $\varphi(v) = 0$ can be solved analytically up to the 4^{th} order. Consequently, this method can be employed in all exponential evaluations but has a significant computational advantage over the usual iterative methods primarily in bi-, tri- and tetraexponential approximations.

Using the values v_i the lifetimes τ_i are given by:

$$\tau_i = \frac{-\Delta t}{\ln(v_i)} \tag{6.7}$$

and Eq. 6.3 becomes a linear set of m equations with only n unknown variables, c_i. By means of the linear least-squares method Eq. 6.3 can be resolved and the values c_i calculated. Thus, the prefactors a_i are given by:

$$a_i = c_i \cdot e^{-t_{in}/\tau_i}\,. \tag{6.8}$$

The product $\tau_i \cdot a_i$ represents the integrated fluorescence signal of the individual species i:

$$\tau_i \cdot a_i = \int_0^\infty a_i \cdot e^{-t/\tau_i}\, dt \tag{6.9}$$

and it depends on the concentrations C_i, on the active one- or multiphoton absorption cross section $\phi_i\,\sigma_i$, on the efficiencies η_i of the detection unit, on an experimental calibration constant K and on the excitation power P. Thereby, ϕ_i is the fluorescence quantum yield and σ_i is the absolute one- or multiphoton absorption cross section. Presuming that the detection efficiency η_i does not dramatically vary for different chromophores, the ratio $\tau_i \cdot a_i / \sum(\tau_i \cdot a_i)$, i.e. the

relative contribution of the component i to the cumulative fluorescence signal, is influenced by both the concentration C_i and by the active absorption cross section $\phi_i \sigma_i$. Consequently, it is necessary to know the photophysical properties of the fluorescing species in order to calculate their relative concentration from the ratio $\tau_i \cdot a_i / \sum(\tau_i \cdot a_i)$.

A rather frequently signalised deficiency of the Prony method is the significant sensitivity to the experimental noise.[38] Therefore, Zhang et al. suggested an optimisation of the Prony method employed in the biexponential evaluation of single fluorescence decays (over 200 data points) by varying the aquisition time-window and by selecting different j in set 6.6 of equations.[38] We tested in our experiments the Prony method both in the genuine form and in the optimised form developed by Zhang. The results of the biexponential FLIM evaluation of 24 fluorescence intensity images registered at successive delays after the pulse in steps of 200 ps are the same within the error margins by means of both methods and with the same computational effort. Moreover, the results agree with the fluorescence lifetimes of the components separately measured in monoexponential FLIM. Consequently, we choose for the evaluation in our FLIM experiments the genuine Prony method.

6.4 Experiment

The basic set-up of the two-photon microscope used in our experiments is similar to that described by Koenig et al.[10] The characteristics of the pulsed laser beam of the Ti:Sa-laser (Mira 900, Coherent) are 200 fs pulse width, 76 MHz repetition rate and 169 nJ pulse energy. The laser beam is driven by two galvanometric mirrors (GSI Lumonics) in order to scan the sample in the x-y plane perpendicular to the optical axis. In z-direction (on the optical axis) the sample is driven by a piezoelectric stage (Physics Instruments) with a precision of 8.42 nm. A microscope objective Achroplan (63×, $NA = 0.95$, water-immersion) of the company Carl Zeiss is used to focus the 10 fold extended laser beam into the sample. The dimensions of the effective two-photon excitation volume are for a wavelength λ of 800 nm $\omega_0 = 0.32$ μm in the x-y plane and $z_e = 1.35$ μm on the optical axis. The calibration was performed by means of fluorescent latex micro-beads for the x-y resolution and of fluorescein-isothiocyanide-monolayers for the z-resolution.[25] As detection unit in the FLIM experiments we use a time-gated system (LaVision) including a high repetition rate intensifier (HRI) with

an adjustable gate ($200 - 1000$ ps) combined with a water-cooled CCD camera (480×640 pixel). The jitter of the detection system is less than 10 ps ($8 - 9$ ps measured in almost noise-free FLIM experiments) at a gate width of 200 ps. A pixel on the CCD chip corresponds to 0.145 ± 0.05 μm at the sample. The dwell time of the laser beam per pixel during one scan is 0.95 μs. The excitation energy per pixel E_{pix} during one scan was varied between 0.015 pJ/pixel and 0.285 pJ/pixel. The size of the scanned field was varied between 25×25 μm^2 and 50×50 μm^2. 15 to 51 fluorescence intensity images were registered at subsequent delays after the pulse in steps of 100 or 200 ps to generate the τ-images.

In the FLIM experiments we used Rhodamin B, β-NADPH, β-NADH, DASPI, i.e. *trans-4-[4-(dimethylamino)-styryl]-1-methylpyridinium iodide*, (Fluka, Germany), DBT 22, i.e. *3,7-bis(diarylamino)-dibenzothiophen-S,S-dioxide*, (synthesised by Kroener, TU Braunschweig), ethanol and DMSO p.a. without further purification.

The artificial skin constructs (ASC) were kindly provided by Prof. Dr. C.C. Mueller-Goymann, TU Braunschweig. The ASC consist of a collagen matrix with incorporated human dermal fibroblasts (HDF), the dermis equivalent, covered by an epidermis equivalent of HaCaT (Human adult at low Calcium concentration and elevated Temperature) keratinocytes.[42] The autofluorescence experiments were performed $1 - 2$ h after the constructs were removed from the incubator. For the labelling experiments the ASC were stained with an aqueous mixture ($pH = 7.15$) of DASPI (83 μmol L^{-1}) and rhodamin B (17 μmol L^{-1}). Thereby, 2 mL of this solution was mixed in the growing medium of the skin constructs. In order to achieve a rapid staining, 5 μL DMSO were also added. The experiments were performed within 2 h after removing the samples from the incubator. During this period a sufficient concentration of the chromophores was assimilated by the samples.

6.5 Results and Discussion

6.5.1 Validation of the Prony Method in Biexponential FLIM

In the following the rapidity and the accuracy of the Prony method as an evaluation technique in the multiexponential fluorescence lifetime imaging is verified.

The evaluation of 24 consecutive fluorescence images (each $1.225 \cdot 10^5$ pixel) by means of the Prony method on a 1.7 GHz Celeron PC takes in our experiments ≈ 20 s, while the evaluation of $\approx 10^5$ pixels by means of iterative methods takes several minutes on a Sun workstation (pixel-by-pixel FLIM-evaluation in frequency domain).[31] This comparison evidences the rapidity of our non-iterative method, which performs one loop per pixel, contrary to iterative methods, which necessitate 8 to 25 iterations per pixel (pixel-by-pixel FLIM-evaluation in time domain).[29] We also tested the accuracy of the Prony method in biexponential FLIM experiments on mixtures of two dyes both in homogenous as well as in heterogeneous media. The resulting fluorescence lifetimes are compared to the fluorescence lifetimes of the components separately measured in monoexponential FLIM experiments. Our results are in good agreement with the results of other authors, who verified the Prony method in non-imaging fluorescence experiments.[38]

A first accuracy test in a homogenous medium was made on a mixture of DBT 22 (45 μmol L^{-1}) and rhodamin B (5 μmol L^{-1}) in ethanol. Since the two-photon absorption cross section $\phi\,\delta$, which reflects the fluorescing properties after two-photon excitation, is lower for DBT 22 ($1.22 \cdot 10^{-49}$ cm^4·s) than for rhodamin B ($\approx 10^{-48}$ cm^4·s), a mixture with a higher content on DBT 22 was used in the experiment, in order to avoid that the signal of the less fluorescing component, i.e. DBT 22, is masked by the background. The fluorescence lifetimes of the components, DBT 22 and rhodamin B, separately measured in monoexponential FLIM experiments amount to 495 ps ($FWHM = 60$ ps) resp. to 2587 ps ($FWHM = 100$ ps). For the ratio of their fluorescence lifetimes ($\tau_2/\tau_1 = 5.23$) the separation of the components by means of the Prony method can be performed optimally.[38] The full-width at half-maximum ($FWHM$) of the fluorescence lifetime distribution is influenced by the jitter of the detection unit, by fluctuations of the laser power and of other experimental factors. However, the centre of this distribution can be determined with a precision of less than 1 ps.

In biexponential FLIM experiments on the aforementioned mixture we determined by means of the Prony method a fluorescence lifetime of 472 ps ($FWHM$ = 74 ps) for DBT 22 (τ_1) and of 2608 ps ($FWHM$ = 112 ps) for rhodamin B (τ_2) (Fig. 6-1). These values agree within the error margins with the fluorescence lifetimes measured in monoexponential FLIM experiments. The separation between DBT 22 and rhodamin B succeeded in 99.9% of the pixels. In the remaining 0.1% of the pixels the fluorescence intensity was so low that the biexponential fluorescence decay was significantly disturbed by the experimental noise and the resulting fluorescence lifetimes corresponded neither to DBT 22 nor to rhodamin B. The relative contribution ($\tau_2\, a_2/(\tau_1\, a_1 + \tau_2\, a_2)$) of rhodamin B to the cumulative fluorescence signal amounts to 70.7%. The remaining 29.3% represents the relative contribution of DBT 22. These results qualitatively agree with the expected ratio ($\tau_2\, a_2/(\tau_1\, a_1 + \tau_2\, a_2)$).

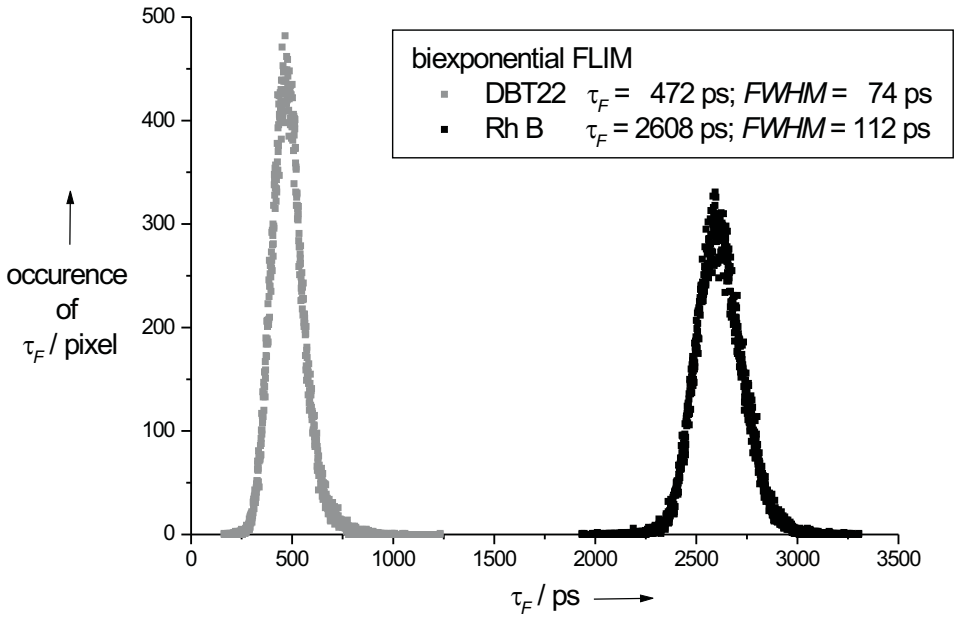

Fig. 6-1: Distribution of the fluorescence lifetime values of DBT 22 resp. rhodamin B after the evaluation of the fluorescence decay images (biexponential FLIM) of a mixture of DBT 22 (45 μmol L^{-1}) and rhodamin B (5 μmol L^{-1}) in ethanol by means of the genuine Prony method.

The parameters employed in this experiment are a scanned surface of 25×25 μm^2, a laser energy E_{pix} at the sample of 0.076 pJ/pixel, an excitation wavelength of 780 nm and an aqusition time of 3 s/frame. 24 fluorescence intensity images were depicted at subsequent delays after the laser pulse in steps of 200 ps.

The fluorescence lifetimes of β-NADPH and rhodamin B in water measured in monoexponential FLIM experiments amount to 412 ps ($FWHM = 15$ ps) resp. to 1530 ps ($FWHM = 47$ ps). The evaluation of the cumulative fluorescence decay of a mixture of β-NADPH (45 μmol L^{-1}) and rhodamin B (5 μmol L^{-1}) in distilled water registered in a biexponential FLIM experiment yielded a lifetime of 399 ps ($FWHM = 175$ ps) attributed to β-NADPH and one of 1504 ps ($FWHM = 147$ ps) attributed to rhodamin B. The contribution of rhodamin B to the cumulative fluorescence signal amounts to 98.1% and that of β-NADPH is 1.9%. The experimental conditions were similar to those described above. This experiment evidences that by means of the Prony method two fluorescing components can be accurately resolved even if the lifetimes ratio τ_2/τ_1 is rather low (3.7)[38] and the contribution of one component to the cumulative fluorescence signal is very large (98%).

The good separation of two chromophores from homogenous mixtures demonstrates that the Prony method is able to correctly approximate biexponential fluorescence intensity decays and creates a solid base for multiexponential FLIM in highly scattering heterogeneous media, e.g. artificial skin constructs. In heterogeneous media the experimental noise is amplified by the scattered light, which makes the separation of the components in a mixture by means of multiexponential FLIM difficult.

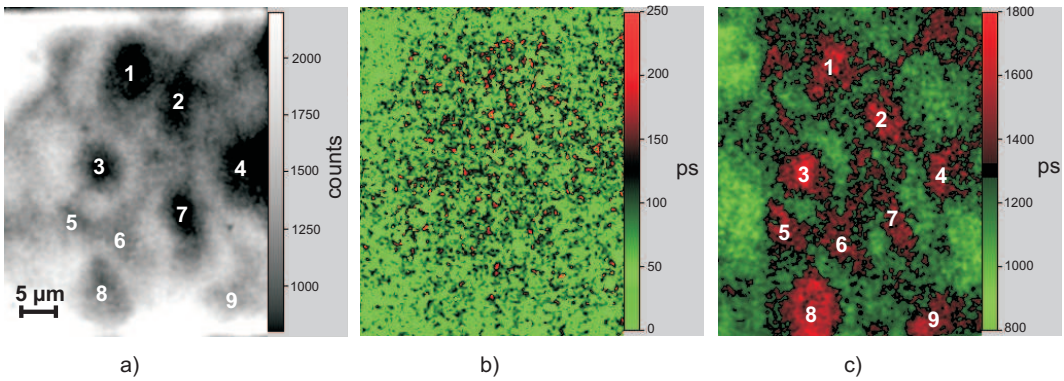

Fig. 6-2: a) intensity image of the artificial epidermis stained with a mixture of rhodamin B and DASPI in ≈ 7 μm depth; b) τ_1-map corresponding to DASPI; c) τ_2-map corresponding to rhodamin B. The numbers in the images a) and c) indicate nine different keratinocytes.

In order to demonstrate that the Prony method is able to correctly approximate the cumulative fluorescence decay measured in biexponential FLIM experiments even under extreme conditions, we resolved DASPI and rhodamin B, two

substances with very different fluorescing properties, in the double-stained epidermis (≈ 7 μm depth) of ASC (Fig. 6-2). While Fig. 6-2 a) shows the steady-state intensity image of a region containing 9 keratinocytes in the artificial epidermis, Fig. 6-2 b) and c) represent the fluorescence lifetime maps of DASPI resp. rhodamin B of the same region. The resulting fluorescence lifetimes for DASPI and rhodamin B are 68 ps ($FWHM = 40$ ps) and 1377 ps ($FWHM = 216$ ps) respectively, which roughly correspond to the values of their lifetimes in water measured in monoexponential FLIM experiments (DASPI: 61 ps ($FWHM = 9$ ps) and rhodamin B: 1530 ps ($FWHM = 92$ ps)). The differences between the fluorescence lifetimes measured in water and those determined in the ASC are ascribed to environmental factors, e.g. refractive index or viscosity.

	monoexp. FLIM	biexp. FLIM
DBT22 (ethanol)	495 ps	472 ps
Rh B (ethanol)	2587 ps	2608 ps
β-NADPH (dest. aq.)	412 ps	399 ps
Rh B (dest. aq.)	1530 ps	1504 ps
DASPI (ASC)	61 ps	68 ps
Rh B (ASC)	1530 ps	[a]1377 ps; [b]1468 ps; [c]1502 ps

Tab. 6-1: Comparison of the fluorescence lifetimes measured in monoexponential and biexponential FLIM, respectively. [a]Fluorescence lifetime of rhodamin B averaged over the whole τ-map uncorrected for the refractive index n. [b]Fluorescence lifetime of rhodamin B in the intercellular matrix averaged over 7 regions corrected for n. [c]Fluorescence lifetime of rhodamin B in the cell interior averaged over 6 cells corrected for n.

In the τ_1-map attributed to DASPI no structural differences between the cell interior and the lipid-like intercellular matrix are discernable (Fig. 6-2 b)). An explanation for this lack of structures is given by the opposite effects of the viscosity[43] and of the refraction index n ($\tau_F = C/n^2$)[44] on the fluorescence lifetime of DASPI. The intercellular matrix is more viscous than the cytosol inside the cells so that the fluorescence lifetime of DASPI in the intercellular regions should be significantly larger.[43] However, a larger refractive index of the intercellular matrix ($n = 1.43$) than of the cell interior ($n = 1.34$) leads to a reduction

of τ_F in the intercellular regions and, thus, to a homogenisation of the fluorescence lifetime all over the image. The refractive index of the artificial epidermis has been determined by means of monoexponential FLIM in ASC stained with coumarin 314 (data not shown). Since the fluorescence lifetime of coumarin 314 is not influenced by pH, viscosity or ion concentration, this dye is adequate as an indicator of the refractive index (data not shown). The τ_2-map of rhodamin B (Fig. 6-2 c)) shows clear differences between the cell interior and the intercellular matrix. The fluorescence lifetime inside the cells (1480 ± 50 ps averaged over 6 cells) is larger than that in the intercellular matrix (1270 ± 70 ps averaged over 7 regions) because the refractive index of the lipid-like membranes ($n = 1.43$) is considerably larger than that of the cytosol ($n = 1.34$). The values of the fluorescence lifetime of rhodamin B corrected for the refractive index are 1468 ± 83 ps in the intercellular regions and 1502 ± 51 ps in the cytosol. Thus, both in the cell interior and in the intercellular matrix the fluorescence lifetime of rhodamin B corrected for n corresponds within the error margins to the lifetime measured in water. The effect of viscosity on the fluorescence lifetime of rhodamin B is negligible (data not shown).

The contribution $\tau_2\, a_2/(\tau_1\, a_1 + \tau_2\, a_2)$ of rhodamin B to the cumulative fluorescence signal amounts to 98% while the rest of 2% represents the contribution of DASPI. The ratio-map, which shows the spatial distribution of $\tau_2\, a_2/(\tau_1\, a_1 + \tau_2\, a_2)$, does not reveal any differences between cell interior and intercellular matrix.

The experimental conditions were a scanned surface of 36×45 μm^2, a laser energy of 0.015 pJ/pixel, an excitation wavelength of 830 nm and an acquisition time of 9 s/image. Under these conditions the sample did not suffer any photodamage. The contribution of cell-autofluorescence to the fluorescence signal was less than 0.05%. In the FLIM experiments we have recorded 51 images at different delays in 100 ps steps. The good separation of DASPI and Rh B in the artificial skin constructs shows that even in highly scattering media, which imply a high experimental noise, our analysis provides an accurate evaluation for multiexponential FLIM.

6.5.2 Endogenous NAD(P)H Fluorescence of Fibroblasts in ASC

We intend to demonstrate the applicability of biexponential FLIM combined with the Prony method in the investigation of the metabolic state of human dermal fibroblasts in artificial skin constructs by means of NAD(P)H endogenous fluorescence.

The fluorescence of the artificial dermis in 40 - 100 μm depth after illumination at 765 nm was observed. Under these conditions, only the fibroblasts show endogenous fluorescence. The collagen matrix and the growing medium do not fluoresce, as verified in autofluorescence experiments of pure collagen solution and of growing medium. The scanned regions were 50×50 μm^2 and the laser energy E_{pix} was varied between 0.015 and 0.15 pJ/pixel.

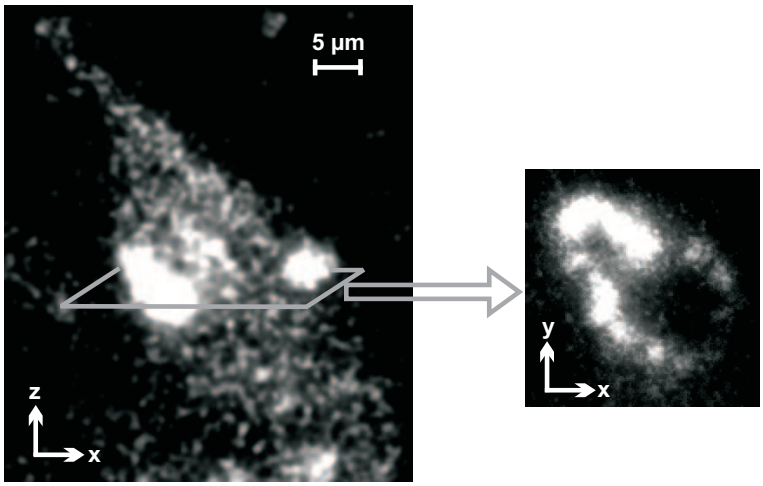

Fig. 6-3: Autofluorescence images of dermal fibroblasts in ASC; longitudinal (left) resp. transverse (right) optical section. The organelle around the non-fluorescing nucleus, the mitochondria, are the brightest due to their high content on NAD(P)H. Employed experimental parameters: $\lambda = 765$ nm, $E_{pix} = 0.039$ pJ/pixel, $depth = 60$ μm.

It was shown that at an excitation wavelength of ≈ 750 nm the main contributors to the cellular endogenous fluorescence are the coenzymes NAD(P)H free or involved in metabolic processes.[1,2,7,8,10,11] The assumption that the intrinsic fluorescence of the fibroblasts observed at $\lambda = 765$ nm originates from NAD(P)H is supported by the fact that the exposure of the skin equivalents to sodium cyanide (NaCN) results in an increase of the fluorescence signal of up to 200%.[8] Moreover, the fluorescence in the cells stems from small granules in the cytosol, mostly organised around the non-fluorescing cell nucleus (Fig. 6-3).

These granules are primarily ascribed to mitochondria, i.e. organelle with a high content on NAD(P)H due to their metabolic function.[10]

The steady state fluorescence images (Fig. 6-3 and Fig. 6-4 a)) mirror the distribution of the cumulative concentration of both free and protein-bound NAD(P)H but do not give any information about the ratio between their concentrations and, thus, about the cellular metabolic state. Since the fluorescence lifetime of the free ($\approx$ 400 ps) resp. protein-bound ($\approx$ 2000 ps) NAD(P)H differ significantly,[10] the biexponential FLIM combined with the Prony method is optimal to rapidly obtain this information contained in the cumulative NAD(P)H fluorescence signal. Moreover, the biexponential approximation is in this case the appropriate approach due to the fact that the cumulative NAD(P)H fluorescence decay deviates considerably from the monoexponential behaviour (data not shown).

In monoexponential FLIM experiments we determined the fluorescence lifetime of the free NADH resp. NADPH to be 444 ± 16 ps and 412 ± 15 ps, respectively. These values agree with the results published by other authors.[10]

A typical result of a biexponential FLIM experiment includes the τ_1-map attributed to the free NAD(P)H (Fig. 6-4 c)), the τ_2-map attributed to the NAD(P)H involved in metabolic processes (Fig. 6-4 d)) and an image, which mirrors the contribution $\tau_2\, a_2 / (\tau_2\, a_2 + \tau_1\, a_1)$ of the protein-bound NAD(P)H to the cumulative fluorescence signal (Fig. 6-4 b)).

The averaged fluorescence lifetime in a τ_1-map amounts to 430 ± 20 ps (averaged over 12 τ_1-maps) and corresponds within the error margins to the fluorescence lifetimes of the free NADH resp. free NADPH measured in monoexponential FLIM experiments. Consequently, the correctness of the performed experiments is warranted. Since the free NADH and NADPH cannot be resolved in FLIM experiments, the resulting fluorescence lifetime of NAD(P)H, i.e. a weighted average of the lifetimes of NADH resp. NADPH, slightly differs from the values measured for the pure components. Further deviations of the lifetime τ_1 from the fluorescence lifetimes of the pure NADH and NADPH, respectively, are attributed to different environmental parameters, e.g. viscosity, refractive index or pH, in the mono- resp. biexponential FLIM experiments. The presence of two species (free NADH and free NADPH) and the effect of the environmental parameters in the cell interior are mirrored in the histogram (Fig. 6-5), which displays the relative occurrence of the lifetimes τ_1. Since the FWHM (150 ± 50 ps) of this distribution is comparable to the width of distributions determined in

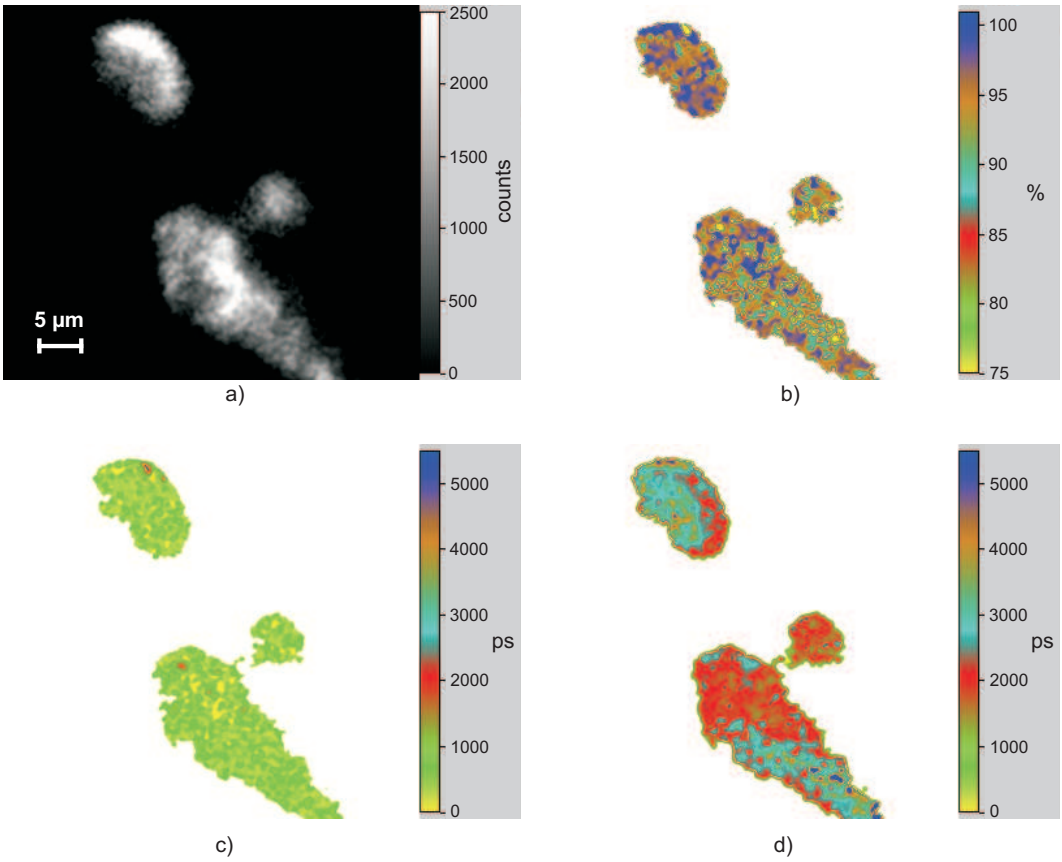

Fig. 6-4: Free and protein-bound NAD(P)H autofluorescence in three fibroblasts in 73 μm depth: a) steady state intensity image; b) ratio-map, i.e. contribution of the protein-bound NAD(P)H to the cumulative fluorescence signal; c) τ_1-map corresponding to the free NAD(P)H; d) τ_2-map corresponding to the NAD(P)H involved in metabolic processes. $E_{pix} = 0.055$ pJ/pixel

biexponential FLIM experiments in homogenous medium, the effect of the factors mentioned above is of minor importance.

The average of the fluorescence lifetimes of the protein bound NAD(P)H in a τ_2-map amounts to $\approx$ 2000 ps (2250 $\pm$ 200 ps averaged over 12 τ_2-maps) as expected.[10] However, the protein-NAD(P)H complexes characterised by different fluorescence lifetimes (between 1000 and 4000 ps) are not uniformly distributed all over the cell interior as assumed until now but concentrated in certain cellular regions (Fig. 6-4 d)). Consequently, we have demonstrated that employing biexponential FLIM it will be possible to simultaneously monitor different metabolic processes in different regions of the cell and, thus, to get a deeper insight into the mechanisms of the cellular metabolism. The large variety of binding possibilities of NAD(P)H as a cofactor is also mirrored in the width (1050 $\pm$ 100 ps) of the histogram (Fig. 6-5), which shows the relative occurrence of the lifetimes τ_2.

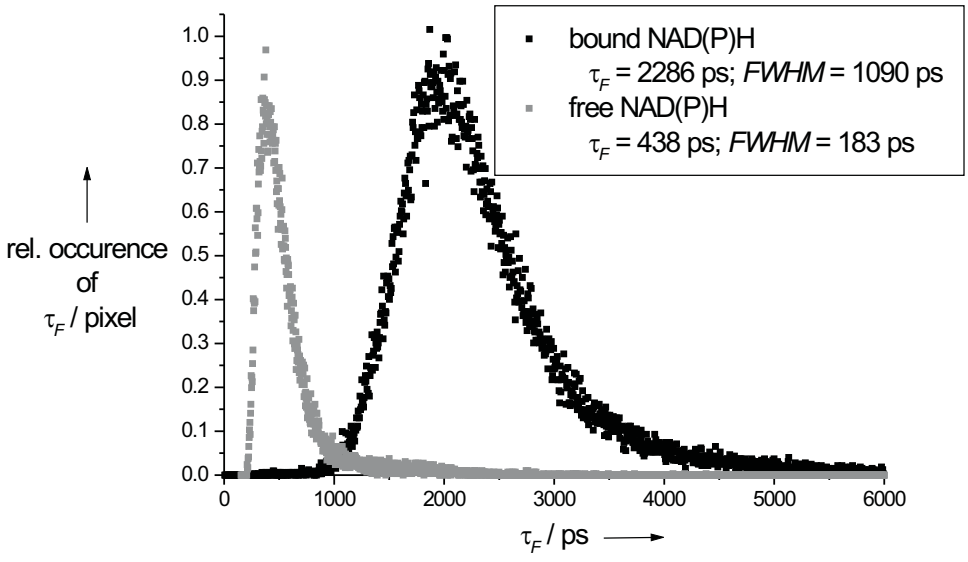

Fig. 6-5: Relative occurrence of the fluorescence lifetimes of free resp. protein-bound NAD(P)H in the fibroblasts pictured in Fig. 6-4 on the page before.

The ratio-maps, which show the relation between the contents of the free resp. protein-bound NAD(P)H, provide the most important information, i.e the cellular metabolic activity in each pixel of the image at a certain point in time. Variations of the ratio $\tau_2\, a_2 / (\tau_2\, a_2 + \tau_1\, a_1)$ within the cell indicate a slower resp. a faster metabolic activity in different organelle. For instance, in Fig. 6-4 b) small granules with a high content ($\approx 100\%$) of protein-bound NAD(P)H which are characterised by a high metabolic activity, are surrounded by the cytosol characterised by a lower $\tau_2\, a_2 / (\tau_2\, a_2 + \tau_1\, a_1)$ ratio.

In order to demonstrate the applicability of the presented biexponential FLIM technique in monitoring the cellular metabolic activity under the influence of external factors we performed FLIM experiments on fibroblasts in ASC under NIR-photostress at 7 different energies E_{pix} (0.015, 0.02, 0.039, 0.055, 0.078, 0.118, 0.152 pJ/pixel). In this way the dependence of the cellular reaction on the illumination energy indicated by the metabolic state could easily be quantified (Fig. 6-6). As anticipated by König et al,[10] the contribution of the protein-bound NAD(P)H to the cumulative autofluorescence signal and, consequently, also the relative concentration of the protein-bound NAD(P)H decreases with increasing laser energy E_{pix} and, thus, the metabolic activity is slower for a more intense NIR photostress.

While at low laser energies E_{pix} the cell merely exhibits a slower metabolism,

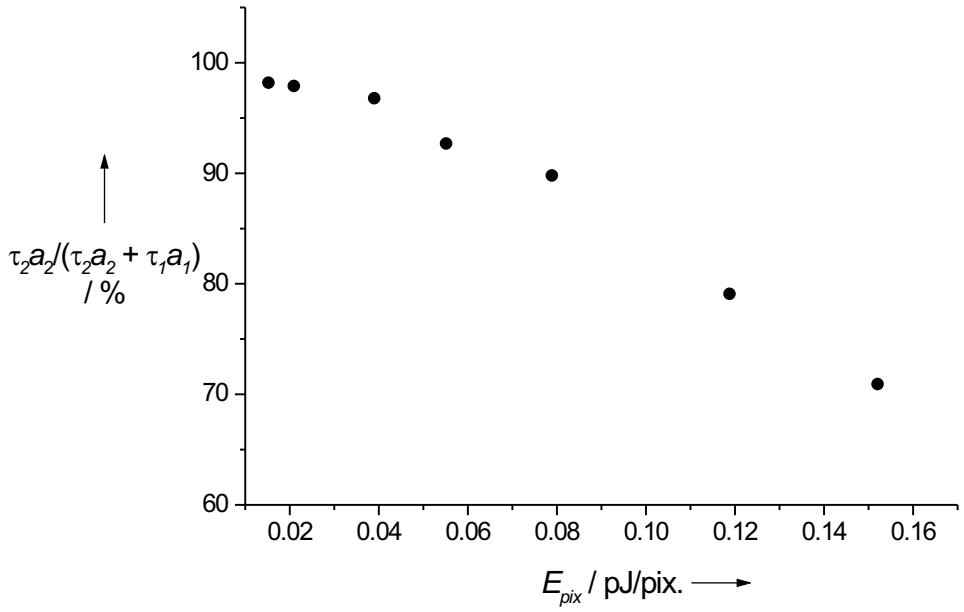

Fig. 6-6: Dependence of the ratio $\tau_2\, a_2/\,(\tau_2\, a_2 + \tau_1\, a_1)$, the contribution of the protein-bound NAD(P)H to the cumulative autofluorescence signal, on the laser energy E_{pix}.

at higher energies morphological changes, plasma formation and finally intracellular optical breakdown occur.[7] In our experiments such phenomena occurred only after an exposure time of $\approx$ 1 h and at laser energies larger than 0.285 pJ/pixel. For the FLIM experiments we have registered 15 to 20 intensity images at consecutive delays in 200 ps steps. The exposure time was 11 s/image.

6.6 Conclusions

We implemented for the first time in FLIM a non-iterative evaluation method generally applicable for multiexponential approximations and verified its accuracy by comparing the fluorescence lifetimes obtained in biexponential FLIM experiments in both homogenous and heterogeneous media with those determined in monoexponential FLIM experiments. In order to probe the limits of the evaluation method, extreme parameters were selected for these experiments: large intensity ratios $\tau_2\, a_2/\tau_1\, a_1$, i.e. the signal of one component is almost masked by the background, and relatively low lifetime ratios τ_2/τ_1 (3.7), for which a separation of the fluorescence lifetimes of the components is difficult. The fluorescence lifetimes determined in biexponential FLIM experiments deviated from those determined

in monoexponential FLIM experiments by less than 5%.

The rapidity and the high accuracy of our method will allow performing dynamical 2D- and 3D- multiexponential FLIM in real time.

We also demonstrated the applicability of the biexponential FLIM combined with the presented non-iterative evaluation technique in the investigation of the cellular metabolism of dermal fibroblasts from ASC by means of endogenous NAD(P)H fluorescence. Thereby, we showed for the first time that the protein-NAD(P)H complexes involved in metabolic processes are not uniformly distributed all over the cell but concentrated in certain cellular regions. Employing the presented method, changes in the metabolic activity of the dermal fibroblasts could directly be visualised in the ratio-maps as we verified in experiments, in which the metabolic activity of the cells under NIR photostress was probed.

References

[1] B.R. Masters, P.T.C. So., E. Gratton, *Biophys. J.* **1997**, 72, 2405-2412

[2] D.W. Piston, B.R. Masters; W.W. Webb, *J. Microscopy* **1995**, 178, 20-27

[3] K. König, U. Wollina, I. Riemann, C. Peuckert, K.-J. Halbhuber, H. Konrad, P. Fischer, V. Fünfstück, T.W. Fischer, P. Elsner, *Proc. SPIE* **2002**, 4620, 191-201

[4] G.H. Patterson, S.M. Knobel, P. Arkhammar, O. Thastrup, D.W. Piston, *Proc. Natl. Acad. Sci.* **2000**, 97, 5203-5207

[5] D.W. Piston, S.M. Knobel, *Trends Endo. Metab.* **1999**, 10, 413-416

[6] S. Maiti, J.B. Shear, R.M. Williams, W.R. Zipfel, W.W. Webb, *Science* **1997**, 275, 530-532

[7] K. Knig, *J. Microscopy* **2000**, 200, 83-104

[8] S. Huang, A.A. Heikal, W.W. Webb, *Biophys. J.* **2002**, 82, 2811-2825 (and the comprised references)

[9] Q. Zhang, D.W. Piston, R.H. Goodman, *Science* **2002**, 295, 1895-1898

[10] K. König, P.T.C. So, W.W. Mantulin, B.J. Tromberg, E. Gratton, *J. Microscopy* **1996**, 183, 197-204

[11] K. König, P.T.C. So, W.W. Mantulin, E. Gratton, *Opt. Lett.* **1997**, 22, 135-136

[12] W. Denk, J.H. Strickler, W.W. Webb, *Science* **1997**, 248, 73-76

[13] W. Becker, A. Bergmann, www.becker.de/pdf/tcvgbh1.pdf, Feb. **2003**

[14] J.R. Lakowicz, K. Berndt, *Rev. Sci. Instrum.* **1991**, 62, 1727-1734

[15] A. Draaijer, R. Sanders, H.C. Gerritsen, p. 491-505, Handbook of biological confocal microscopy, J. Pawley, Plenum Press, New York, **1995**

[16] K.M. Hanson, M.J. Behne, N.P. Barry, T.M. Mauro, E. Gratton, R.M. Clegg, *Biophys. J.* **2002**, 83 (3), 1682-1690

[17] J.R. Lakowicz, H. Szmacinski, M.L. Johnson, *J. Fluorescence* **1992**, 2, 47-62

[18] J. Digel, T. Kobayashi, Z. Gryczynski, J.R. Lakowicz, J.H. Collins, *Arch. Biochem. Biophys.* **2001**, 387(2), 243-249

[19] H. Szmacinski, J.R. Lakowicz, *Anal. Biochem.* **1997**, 250, 131-138

[20] H.C. Gerritsen, R. Sanders, A. Draaijer, Y.K. Levine, *J. Fluorescence* **1997**, 7, 11-16

[21] S. Murata, P. Herman, J.R. Lakowicz, *Cytometry* **2001**, 43, 94-100

[22] W. Becker, A. Bergmann, C. Biskup, T. Zimmer, N. Klöcker, K. Benndorf, *Proc. SPIE* **2002**, 4620

[23] A. Squire, P.J. Verveer, P.I.H. Bastiaens, *J. Microscopy* **2000**, 197, 136-149

[24] P.J. Verveer, A. Squire, P.I.H. Bastiaens, *Biophys. J.* **2000**, 78, 2127-2137

[25] A. Schönle, M. Glatz, S.W. Hell, *Appl. Opt.* **2000**, 39, 6306-6311

[26] V. Barzda, C.J. Grauw, J. Vroom, F.J. Kleima, R. van Grondelle, H. van Amerongen, H.C. Gerritsen, *Biophys. J.* **2001**, 81, 538-546

[27] P.T.C. So, H. Kim, *Opt. Exp.* **1998**, 3, 339-350

[28] B.R. Masters, P.T.C. So, E. Gratton, *Ann. N.Y. Acad. Sci.* **1998**, 838, 58-67

[29] K.C. Benny Lee, J. Siegel, S.E.D. Webb, S. Lvque-Fort, M.J. Cole, R. Jones, K. Dowling, M.J. Lever, P.M.W. French, *Biophys. J.* **2001**, 81, 1265-1274

[30] E. Gratton, S. Breusegem, J. Sutin, Q. Ruan, N. Barry, *J. Biomed. Opt.* **2003**, 8, 381-390

[31] P.J. Verveer, P.I.H. Bastiaens, *J. Microscopy* **2003**, 209, 1-7

[32] A.D. Scully, R.B. Ostler, D. Phillips, P. O'Neill, K.M.S. Townsend, A.W. Parker, A.J. MacRobert, *Bioimaging* **1997**, 5, 9-18

[33] R.J. Woods, S. Scypinski, L.J. Cline Love, H. Ashworth, *Anal. Chem.* **1984**, 56, 1395-1400

[34] R.M. Ballew, J.N. Demas, *Anal. Chem.* **1989**, 61, 30-33

[35] K.K. Sharman, A. Periasamy, H. Ashworth, J.N. Demas, N.H. Snow, *Anal. Chem.* **1999**, 71, 947-952

[36] C. Stehing, G. Holst, *Proc. SPIE*, 4578, issue 31, **2001**

[37] C.-E. Fröberg, p. 257-258, Numerical Mathematics - Theory and Computer Applications, The Benjamin / Cummings Publishing Company, Inc., Menlo Park, California, **1985**

[38] Z.Y. Zhang, T. Sun, K.T.V. Grattan, A.W. Palmer, *Proc. SPIE* **1997**, 2980, 90-95

[39] V.V. Apanasovich, E.G. Novikov, *Opt. Comm.* **1990**, 78, 279-282

[40] K. Sasaki, H. Masuhara, *Appl. Opt.* **1991**, 30, 977-980

[41] J. Enderlein, R. Erdmann, *Opt. Comm.* **1997**, 134, 371-378

[42] A. Winkler, C.C. Müller-Goymann, *Eur. J. Pharm. Biopharm.* **2002**, 53, 281-287

[43] D.S. Elson, J. Siegel, S.E.D. Webb, S. Leveque-Fort, M.J. Lever, P.M.W. French, K. Lauritsen, M. Wahl, R. Erdmann, *Opt. Lett.* **2002**, 27, 1409-1411

[44] S.J. Strickler, R.A. Berg, *J. Chem. Phys.* **1962**, 37, 814-822

Chapter 7

Summary and Outlook

The development of fluorescence microscopy techniques, which reproduce the real environmental conditions of biological systems without perturbing the natural phenomena therein, is of major significance for the biosciences, since in this way a comprehensive view of the effects and processes of interest can be obtained. To the most powerful bioscientific tools belong fluorescence fluctuation microscopy (FFM) techniques, e.g. fluorescence correlation spectroscopy (FCS) or photon counting histogram (PCH) analysis, and fluorescence imaging techniques, e.g. fluorescence lifetime imaging (FLIM). Given the large interest for these methods, the topic of this work is focused on the design of novel FLIM applications of particular relevance for the pharmaceutical and medical research and on the development of theoretical approaches, which contribute to the improvement of fluorescence fluctuation techniques.

The accurate simulation of the real biological environment implies that highly-resolved investigations are possible also deep within thick samples, i.e. in intact cells and tissues. The fluorescence far-field microscopy based on two-photon excitation (TPE) represents the most adequate method for studies in intact biological samples because it provides a high intrinsic 3D spatial resolution and a large penetration depth due to the use of NIR excitation light, for which the tissues are mostly transparent. The experiments described in chapter 5, in which artificial skin equivalents (thickness $\approx$ 5 mm) were investigated down to 200 μm depth with submicron resolution, demonstrate once more the huge advantages of TPE microscopy for the modern biosciences.

Although the importance of the two-photon excitation microscopy in FCS investigations on biological systems is undisputed, there are no appropriate theoretical models to simulate fluorescence autocorrelation functions registered in

TPE experiments. Most of the available FCS models consider that the molecules present in the observation volume are illuminated with cw laser light. However, in TPE applications pulsed illumination is typically employed. Thus, by means of these models, parameters characteristic for illumination-dependent photoprocesses cannot be correctly assessed from TPE experimental data. The very few FCS approaches based on pulsed illumination are also inadequate because they consider the effect of pulsed illumination only on excitation but not on other photoprocesses like photobleaching or induced emission. In chapter 3 of this work, a new theoretical FCS model is presented, which simulates fluorescence autocorrelation functions registered in TPE experiments considering the effect of pulsed illumination on all illumination-dependent photoprocesses. Thus, this model counteracts the deficits of the former FCS approaches and allows for the first time an accurate determination of photodynamic parameters from TPE experimental data.

The theoretical FCS models describe the most probable behaviour of an individual molecule and, thus, they restore the statistics of single molecules. If the system under investigation is ergodic, the results of these models can be compared without concern to data obtained both in experiments on single molecules and in experiments on ensembles of molecules. In non-ergodic systems, the statistics of single molecules differ from the statistics of ensembles of molecules and, thus, the theoretical approaches correctly reproduce only the data registered in experiments on individual molecules. In order to avoid the hypothetical assumption that the behaviour of an individual molecule is identical to the behaviour of a group of molecules, the new developed FCS model was validated in TPE experiments on single coumarin 153 and coumarin 314 molecules.

Fluorescence fluctuation experiments in single-molecule detection regime are particularly relevant for the biosciences, since they provide an unique image of the heterogeneity in non-ergodic biological systems, which cannot be obtained in experiments on ensembles of molecules. However, the quantification of the single-molecule detection regime was mostly neglected until now. In chapter 4 of this work, a method based on the PCH analysis is presented, which allow the quantitative determination of the single-molecule detection regime and, consequently, the accurate design of specific single-molecule FFM experiments necessary in bioscientific investigations. The reliability of this method was verified in fluorescence fluctuation experiments on diluted glycol solutions of coumarin 153.

The artificial skin constructs (ASC) as economical test-samples employed in

the validation of new medicines are of major interest for the dermatological and pharmaceutical research. In this frame, it is essential for the artificial skin to have a similar morphology and functionality like the human skin. Particularly important is the barrier function, i.e. the selective permeability of the skin, which is strongly related to the epidermal acidic mantle, i.e. the epidermal pH-gradient. Chapter 5 of this work describes monoexponential FLIM experiments on intact ASC stained with exogenous chromophores, namely BCECF as pH indicator and coumarin 314 as indicator of the refractive index. These experiments enabled for the first time the accurate 3D visualisation of the pH-gradient and of the distribution of refractive indices in the artificial epidermis. The morphology of the artificial skin was also investigated in fluorescence imaging experiments on intact samples. Hence, the suitability of ASC as reliable skin models is verified and the position of FLIM as a versatile bioscientific tool is consolidated.

The design of non-labelling techniques is of major relevance for the biosciences, since they provide a maximum amount on information but minimally modify the system under study. In chapter 6 of this work, biexponential FLIM experiments on intact ASC are presented, in which the redox metabolism of dermal fibroblasts is visualised basing on the fluorescence of the endogenous chromophores NADH and NADPH, hereafter NAD(P)H. The typical result of such an experiment consists of three images: two fluorescence lifetime images corresponding to free NAD(P)H and protein-bound NAD(P)H, respectively, and a ratio image, which mirrors the contribution of the protein-bound NAD(P)H to the cumulative fluorescence signal. The ratio image represents the highly-resolved map of the cellular redox metabolism. The biexponential FLIM approximation was performed using a fast non-iterative method, i.e. the Prony method, which reduce the evaluation time up to 98%. This new FLIM application is particularly suitable to investigate the dynamics of biological processes, since it allows a rapid non-invasive monitoring of the cellular metabolism in thick samples with subcellular resolution.

An immediate application of the biexponetial FLIM based on NAD(P)H autofluorescence will be the investigation of the mechanisms of insulin secretion, an essential pre-stage in the development of new medicines against type II diabetes. Thereby, the redox metabolism of β-cells is monitored in real time in intact pancreatic islets under the influence of stimulating or inhibiting factors, e.g. glucose or antidiabetic agents. Since the insulin secretion strongly depends on the metabolic state of the insulin producing β-cells, the FLIM experiments will

provide detailed insight in the process of insulin production and release. Further applications of this method are planned in the immunological research.

As previously discussed, biexponential FLIM allows the separation of free NAD(P)H from NAD(P)H involved in metabolic processes, i.e. protein-bound NAD(P)H. The fluorescence lifetime image of protein-bound NAD(P)H typically shows a heterogeneous distribution, which indicates a large diversity of protein-NAD(P)H complexes, i.e. different metabolic processes. However, FLIM cannot provide precise information about the individual protein-NAD(P)H complexes due to cross effects of environmental factors, e.g. pH, refractive index, ions concentration, on the fluorescence lifetime of these complexes. A fluorescence imaging technique, which counteracts this deficit of FLIM, is the rotational correlation time imaging by anisotropic fluorescence (RIMAF). In RIMAF experiments, the rotational correlation time of molecules is determined from the fluorescence anisotropy decay in each pixel of the image. Since the rotational time is influenced only by factors like viscosity and strength of the chemical bounds, perturbing cross effects of other environmental factors are eliminated. By performing both RIMAF and FLIM experiments, we expect that a more detailed image of the environmental parameters and of the vital cellular processes will be achieved.

The current TPE microscopy, in which the molecules are simultaneously excited with two identical NIR photons, allows the monitoring of a wide spectrum of exogenous and endogenous chromophores. Typical exceptions thereof are the endogenous chromophores and biomolecules, which absorb in the UV domain. A technique, which would enable us to observe these biomolecules, is based on the simultaneously excitation of the molecules with two photons of different wavelength, for instance, a 400 nm photon and a 800 nm photon. This technique has the same advantages as the standard TPE microscopy, but allows non-labelling investigations on vital biomolecules like DNA, adenosine diphosphate (ADP) or adenosine triphosphate (ATP), which are currently not possible. Moreover, experiments, in which non-labelled samples are simultaneously illuminated with monochromatic laser light and white light, would allow an ultrafast *in situ* registration of two-photon absorption spectra with a high 3D resolution. Such applications can revolutionise the analysis techniques in intact biological systems.

Most of the optical bioscientific techniques are based on the fluorescence of molecules due to advantages like high sensitivity, instrumental stability and relatively simple experimental set-up. However, many biomolecules, which play a

central role in vital cellular processes, fluoresce very weakly or do not fluoresce at all. Therefore, alternative microscopy techniques based on Raman scattering have been developed, e.g. Raman imaging (RI). Analogous to OPE fluorescence experiments, in RI experiments the signal of interest can be hardly separated from the excitation light due to the similar wavelengths. Hence, an imaging procedure based on the observation of hyper-Raman scattering, in which the wavelength of the excitation beam is two times larger than that of the hyper-Raman signal, appears to be a more reliable and simple technique. In order to increase the probability of the Raman process and, thus, to register a sufficiently large signal, resonant hyper-Raman scattering should be employed in the imaging experiments, i.e. resonant hyper-Raman imaging (RHRI). RHRI non-labelling experiments would allow us to accurately visualise a part of the non-fluorescing 90% of the cellular content. The practical realisation of RHRI as a reliable investigation tool for the biosciences would represent a consolidation of the still new field of non-fluorescence optical microscopy.

Appendix A

Simulation of PCH

The simulation of photon counting histograms (PCH) of fluorescence signals registered in FFM experiments is performed by means of an ANSI C code. The PCH of the fluorescence signal of a molecule, which dwells all the measurement time in the observation volume, is assessed using the main program `weinst.c`. In its subroutines, `gamma.c` and `quadratur.c`, the alternative incomplete gamma function is determined. The terms of the alternative incomplete gamma function are calculated in `gamma.c` as specified in chapter 4 (appendix). In `quadratur.c`, the numerical integration of these terms is performed. Using the output of `weinst.c` as input for `convolutionN.c`, the photon counting histograms of the fluorescence signal of two, three, up to N_{max} molecules are determined and the weighted sum of all these PCH and of the background distribution is built. The output of `convolutionN.c` corresponds to the real photon counting histogram of the experimental fluorescence signal. In the following, the source codes of `weints.c`, `gamma.c`, `quadratur.c` and `convolutionN.c` are provided.

A.1 PCH of One Molecule

A.1.1 `weinst.c`

```
1   #include ⟨stdio.h⟩
2   #include ⟨math.h⟩
3
4   #define pi 3.1459265358979
5   #define e 2.71828182
6
7   double* gamma (double, double, int);
8   double* quadratur (double, double, int);
```

```
 9
10   int main (void)
11   {
12      FILE *pdatei;
13      double hell, ge, ze, V, omega, lambda, fakult, sum;
14      int n, i;
15      double *Q;
16      double p1[40];
17
18      hell = 1.21;
19      omega = 0.349;/*μm*/
20      lambda = 0.8;/*μm*/
21      ze = pi*omega*omega*(sqrtl(e) - 1)/lambda;/*μm*/
22      ge = 15.0
23      V = 2*pi*omega*omega*ze*(1.333333333 + e + 2*sqrtl(e));/*μm^3*/
24      n = 20;
25
26      Q = quadratur(hell, ge, n);
27
28      fakult = 1.0;
29      sum = 0.0;
30      for (i = 0; i < n + 1; i++)
31      {
32         fakult *= (i + 1);
33         Q[i] = (Q[i]*pow(pi, 2)*pow(omega, 4))/(4*fakult*V*lambda);
34      }
35      p1[0] = sum;
36      for (i = 0; i < n + 1; i++)
37      {
38         p[i] = Q[i-1];
39      }
40
41      pdatei = fopen("weinsP22.dat","w");
42
43      if (pdatei == NULL)
44         printf("Datei schreibgeschützt.\n");
45      else
46      {
47         fprintf(pdatei, "%d\n", n + 1);
48         for (i = 0; i < n + 1; i++)
49         {
50            fprintf(pdatei, "%e\n", p1[i]);
51         }
52         printf("O.K.\n");
53         fclose(pdatei);
54      }
55   }
```

A.1.2 gamma.c

```
 1   #include ⟨math.h⟩
 2   #define pi 3.1459265358979
 3
 4   double f (double t)
 5   {
 6      return exp(-t);
 7   }
 8
 9   double* gamma (double b, double c, int m)
10   {
11      double v1[50], v2[50], v[50];
```

```
12       double a;
13       int k;
14
15       a = 4*b/(pow(pi, 2)*pow(1+c*c, 2));
16
17       v1[0] = -1.0;
18       v2[0] = -f(a);
19       v [0] = 1.0 - f(a);
20
21       for (k = 0; k < m; k++)
22       {
23          v1[k] = k*v1[k-1];
24          v2[k] = -f(a)*pow(a, k) + k*v2[k-1];
25          v [k] = v2[k] - v1[k];
26       }
27       return v;
28    }
```

A.1.3 quadratur.c

```
 1    #include ⟨math.h⟩
 2
 3    double h (double r)
 4    {
 5       return 1 + r*r;
 6    }
 7    double* gamma (double, double, int);
 8
 9    double* quadratur (double hellig, double ge, int n);
10    {
11       int j, i;
12       double Q[50], x[3], w[3];
13       double *I1, *I2, *I3, *I4, *I5;
14
15       x[0] = -0.906179845938664;
16       x[1] = -0.538469310105683;
17       x[2] = 0.0;
18
19       w[0] = 0.236926885056189;
20       w[1] = 0.478628670499366;
21       w[2] = 0.568888888888889;
22
23       for (i = 0; i < 3; i++)
24       {
25            x[i] = ge*x[i];
26       }
27
28       I1 = gamma (hellig, x[0], n);
29       I2 = gamma (hellig, x[1], n);
30       I3 = gamma (hellig, x[2], n);
31       I4 = gamma (hellig, -x[1], n);
32       I5 = gamma (hellig, -x[0], n);
33
34       for (j = 0; i < n; j++)
35       {
36          Q[j] = ge*(h(x[0])*w[0]*(I1[j]+I5[j]) + h(x[1])*w[1]*(I2[j]+I4[j]) +
                       + I3[j]*h(x[2])*w[2]);
37       }
38       return Q;
39    }
```

A.2 Real PCH

A.2.1 convolutionN.c

```
#include ⟨stdio.h⟩
#include ⟨math.h⟩

#define Nmittel 0.48
#define pi 3.1459265358979
#define e 2.71828182

int g (int y)
{
   int fak, i;
   fak = 1;
   if (y > 0)
   {
     for (i = 1; i < y + 1; i++)
     {
       fak *= i;
     }
   }
   else
     fak = 1;
  return fak;
}

int main (void)
{
   FILE *pdatei;
   double v1[80], v2[30000], konv[30000], p[30000];
   int i, j, n, m, k, N, r, q;

   pdatei = fopen ("weinsP22.dat.dat", "r");
   if (pdatei == NULL)
     printf("Datei existiert nicht.\n");
   else
   {
     fscanf(pdatei, "%d", &n);
     for (i = 0; i < n; i++)
     {
       fscanf(pdatei, "%lf", &v1[i]);
     }
   }
   fclose(pdatei);

   N = 1;
   m = n;

   for (i = 0; i < m; i++)
   {
     v2[i] = v1[i];
   }

   p[0] = exp(-Nmittel);

   for (i = 0; i < 200; i++)
   {
     p[i] = 0;
   }

   k = 0.2;
   do
   {
```

```
61      if (m >= n)
62      {
63        for (j = 0; j < n; j++)
64        {
65          konv[j] = 0;
66          for (i = 0; i < j + 1; i++)
67          {
68            konv[j] += v1[i]*v2[j - i];
69          }
70        }
71
72        for (j = n; j < m; j++)
73        {
74          konv[j] = 0;
75          for (i = 0; i < n; i++)
76          {
77            konv[j] += v1[i]*v2[j - i];
78          }
79        }
80
81        for (j = m; j < m + n - 1; j++)
82        {
83          konv[j] = 0;
84          for (i = j - m + 1; i < n; i++)
85          {
86            konv[j] += v1[i]*v2[j - i];
87          }
88        }
89      }
90      else
91      {
92        for (j = 0; j < n; j++)
93        {
94          konv[j] = 0;
95          for (i = 0; i < j + 1; i++)
96          {
97            konv[j] += v2[i]*v1[j - i];
98          }
99        }
100
101       for (j = n; j < m; j++)
102       {
103         konv[j] = 0;
104         for (i = 0; i < n; i++)
105         {
106           konv[j] += v2[i]*v1[j - i];
107         }
108       }
109
110       for (j = m; j < m + n - 1; j++)
111       {
112         konv[j] = 0;
113         for (i = j - m + 1; i < n; i++)
114         {
115           konv[j] += v2[i]*v1[j - i];
116         }
117       }
118     }
119
120     m = m + n - 1;
121
122     for (i = 0; i < m; i++)
123     {
124       v2[i] = konv[i];
125       if (k <= 9)
126       {
```

```
127           p[i] += v2[i]*exp(-Nmittel)*exp(k*log(Nmittel) - log(g(k)));
128         }
129         else
130         {
131           p[i] += v2[i]*exp(-Nmittel)*exp(k*log(Nmittel) -
                    - (k + 0.5)*log(k) + k - 0.5*log(2*pi));
132         }
133       }
134
135       k++;
136       }
137       while (k < N);
138
139       r = 50;
140
141       for (i = 0; i < r; i++)
142       {
143         v1[i] = p[i]
144       }
145
146       q = 50;
147
148       for (j = 0; j < q; j++)
149       {
150         if (j < 10)
151         {
152           v2[j] = exp(-1)*pow(1, j)/g(j);
153         }
154         else
155         {
156           v2[j] = exp(-1+j*log(1)-(j+0.5)*log(j)+j-0.5*log(2*pi));
157         }
158       }
159
160       if (q >= r)
161       {
162         for (j = 0; j < r; j++)
163         {
164           p[j] = 0;
165           for (i = 0; i < j + 1; i++)
166           {
167           p[j] += v1[i]*v2[j - i];
168           }
169         }
170
171         for (j = r; j < q; j++)
172         {
173           p[j] = 0;
174           for (i = 0; i < r; i++)
175           {
176           p[j] += v1[i]*v2[j - i];
177           }
178         }
179
180         for (j = q; j < r + q - 1; j++)
181         {
182           p[j] = 0;
183           for (i = j - q + 1; i < r; i++)
184           {
185           p[j] += v1[i]*v2[j - i];
186           }
187         }
188       }
189       else
190       {
```

```
191         for (j = 0; j < r; j++)
192         {
193           p[j] = 0;
194           for (i = 0; i < j + 1; i++)
195           {
196           p[j] += v2[i]*v1[j - i];
197           }
198         }
199
200         for (j = r; j < q; j++)
201         {
202           p[j] = 0;
203           for (i = 0; i < r; i++)
204           {
205           p[j] += v2[i]*v1[j - i];
206           }
207         }
208
209         for (j = q; j < r + q - 1; j++)
210         {
211           p[j] = 0;
212           for (i = j - q + 1; i < r; i++)
213           {
214           p[j] += v2[i]*v1[j - i];
215           }
216         }
217       }
218
219       pdatei = fopen ("C153P22N50.dat", "w");
220
221       if (pdatei == NULL)
222       {
223         printf("Datei schreigeschützt.\n");
224       }
225       else
226       {
227         for (j = 0; j < r + q - 1; j++)
228         {
229         fprintf(pdatei, "%e\n", p[j]);
230         }
231         printf("O.K.\n")
232         fclose(pdatei)
233       }
234     }
```

Appendix B

Biexponential FLIM Evaluation

The biexponential FLIM evaluation is based on a fast non-iterative method, i.e. the Prony method (see chapter 6), and performed using a Python code, i.e. `PronyFLIM.py`. Fluorescence intensity images read in as arrays constitute the input of `PronyFLIM.py`. The intensity images are previously registered at successive time-points after the laser pulse. The output of `PronyFLIM.py` consists of two fluorescence lifetime images and a ratio image, which restores the contribution of the chromophore characterised by the longer lifetime to the cumulative fluorescence signal.

B.1 `PronyFLIM.py`

```
 1   import Numeric
 2   import TableIO
 3   import math
 4   import os
 5
 6   threshold = 50.0 #counts
 7
 8   t = [] #ps
 9   dt = 100.0 #ps
10   nmatrix = 10.0
11   tinitial = 7300.0 #ps
12   thelp = (tinitial - 7000.0)/dt
13   for i in range(nmatrix):
14        t.append(tinitial + i*dt)
15
16   data1 = TableIO.readTableAsArray('RhBDBT01.txt','#')
17   data2 = TableIO.readTableAsArray('RhBDBT02.txt','#')
18   data3 = TableIO.readTableAsArray('RhBDBT03.txt','#')
19   data4 = TableIO.readTableAsArray('RhBDBT04.txt','#')
20   data5 = TableIO.readTableAsArray('RhBDBT05.txt','#')
21   data6 = TableIO.readTableAsArray('RhBDBT06.txt','#')
22   data7 = TableIO.readTableAsArray('RhBDBT07.txt','#')
23   data8 = TableIO.readTableAsArray('RhBDBT08.txt','#')
24   data9 = TableIO.readTableAsArray('RhBDBT09.txt','#')
```

```
25    data10 = TableIO.readTableAsArray('RhBDBT10.txt','#')
26
27    tauf1 = TableIO.readTableAsArray('RhBDBT01.txt','#')
28    tauf2 = TableIO.readTableAsArray('RhBDBT01.txt','#')
29    ampli = TableIO.readTableAsArray('RhBDBT01.txt','#')
30
31    for i in range(len(data1)):
32       for j in range(len(data1[0])):
33         datalist = [data1[i][j], data2[i][j], data3[i][j], data4[i][j],
34                     data5[i][j], data6[i][j], data7[i][j], data8[i][j]]
35                     data9[i][j], data10[i][j]]
36         if datalist[0] > threshold:
37           summ1v = 0.0
38           summ2v = 0.0
39           summ3v = 0.0
40           summ4v = 0.0
41           summ5v = 0.0
42           summ6v = 0.0
43           #
44           deltaN = 1
45           l = 0
46           #
47           for k in range(len(datalist)-2):
48             summ1v += datalist[k + deltaN]*datalist[k + deltaN + 1]
49             summ2v += datalist[k + deltaN + 1]*datalist[k]
50             summ3v += datalist[k + deltaN]*datalist[k + 1]
51             summ4v += datalist[k + 1]*datalist[k]
52             summ5v -= datalist[k + 2*deltaN]*datalist[k + deltaN + 1]
53             summ6v -= datalist[k + 2*deltaN]*datalist[k + 1]
54           #
55           detv = summ4v*summ1v - summ2v*summ3v
56           if detv != 0.0:
57             s1 = (summ4v*summ5v - summ2v*summ6v)/detv
58             s2 = (summ1v*summ6v - summ3v*summ5v)/detv
59             #
60             delta = s1*s1 - 4*s2
61             if delta > 0.0:
62               v1 = (-s1 - math.sqrt(delta))/2
63               v2 = (-s1 + math.sqrt(delta))/2
64               #
65               x = []
66               y = []
67               summ1c = 0.0
68               summ2c = 0.0
69               summ3c = 0.0
70               summ4c = 0.0
71               summ5c = 0.0
72               for k in range(len(datalist)):
73                 x.append(math.pow(v1,k))
74                 y.append(math.pow(v2,k))
75                 summ1c += x[k]*x[k]
76                 summ2c += x[k]*y[k]
77                 summ3c += y[k]*y[k]
78                 summ4c += datalist[k]*x[k]
79                 summ5c += datalist[k]*y[k]
80               #
81               detc = summ3c*summ1c - summ2c*summ2c
82               if detc != 0.0:
83                 c1 = (sum4c*summ3c - summ2c*summ5c)/detc
84                 c2 = (sum1c*summ5c - summ2c*summ4c)/detc
85               else:
86                 c1 = 0.0
87                 c2 = 0.0
88               #
89               if c1 > 0.0 and v1 != 1.0:
90                 tau1 = -dt/math.log(math.fabs(v1))
91                 a1 = math.fabs(c1)/math.pow(math.fabs(v1),thelp)
92               else:
93                 tau1 = 0.0
94                 a1 = 0.0
```

```
 95              #
 96              if c2 > 0.0 and v2 != 1.0:
 97                tau2 = -dt/math.log(math.fabs(v2))
 98                a2 = math.fabs(c2)/math.pow(math.fabs(v2),thelp)
 99              else:
100                tau2 = 0.0
101                a2 = 0.0
102              #
103              if tau1 > tau2:
104                tauf1[i][j] = tau2
105                tauf2[i][j] = tau1
106                if a1 != 0.0:
107                  ampli[i][j] = a1*tauf1[i][j]/
108                    /(a1*tauf1[i][j] + a2*tauf2[i][j])
109                else:
110                  ampli[i][j] = 0.0
111              else:
112                tauf1[i][j] = tau1
113                tauf2[i][j] = tau2
114                if a2 != 0.0:
115                  ampli[i][j] = a2*tauf2[i][j]/
116                    /(a1*tauf1[i][j] + a2*tauf2[i][j])
117                else:
118                  ampli[i][j] = 0.0
119            #
120            elif delta == 0.0:
121              v2 = -s1/2
122              v1 = 0.0
123              if v2 != 0.0 and v2 != 1.0:
124                tauf2[i][j] = -dt/math.log(math.fabs(v2))
125                tauf1[i][j] = 0.0
126                ampli[i][j] = 100.0
127              else:
128                tauf2[i][j] = 0.0
129                tauf1[i][j] = 0.0
130                ampli[i][j] = 0.0
131            else:
132              v1 = 0.0
133              v2 = 0.0
134              tauf1[i][j] = 0.0
135              tauf2[i][j] = 0.0
136              ampli[i][j] = 0.0
137          else:
138            v1 = 0.0
139            v2 = 0.0
140            tauf1[i][j] = 0.0
141            tauf2[i][j] = 0.0
142            ampli[i][j] = 0.0
143        else:
144          v1 = 0.0
145          v2 = 0.0
146          tauf1[i][j] = 0.0
147          tauf2[i][j] = 0.0
148          ampli[i][j] = 0.0
149    #
150    for i in range(len(data1)):
151       for j in range(len(data1[0])):
152         if tauf1[i][j] < 10 or tauf1[i][j] > 10000:
153           tauf1[i][j] = 0.0
154         if tauf2[i][j] < 10 or tauf2[i][j] > 10000:
155           tauf2[i][j] = 0.0
156    #
157    TableIO.writeArray('tau1.txt',tauf1)
158    TableIO.writeArray('tau2.txt',tauf2)
159    TableIO.writeArray('ratio.txt',ampli)
```

Danksagung

Die vorliegende Arbeit entstand während meiner Tätigkeit als wissenschaftliche Mitarbeiterin am Institut für Physikalische und Theoretische Chemie der Technischen Universität Braunschweig unter der Leitung von Herrn Prof. Dr. Karl-Heinz Gericke.

Meinem Mentor, Herrn Prof. Dr. Karl-Heinz Gericke, möchte ich besonders herzlich danken für seine wissenschaftliche Betreuung und seine jederzeit gewährte Unterstützung.

Für die Übernahme des Koreferats und das gezeigte Interesse an der Arbeit gilt mein Dank Herrn Prof. Dr. Peter Jomo Walla.

Weiterhin möchte ich mich bei Dr. Wolfgang Roth, Dr. Christof Maul, Bülent Peker und Peter Schlüsche für ihre Bereitschaft zu Diskussion und ihre Unterstützung im Labor bedanken. Der ganzen Arbeitsgruppe möchte ich ebenfalls danken für eine überaus freundliche Atmosphäre.

Mein Dank gilt auch Herrn Peter Ahrens für komplizierte Sonderanfertigungen von Teilen des Zweiphotonenmikroskops.

Für die zur Verfügung gestellten künstlichen Hautkonstrukte möchte ich mich bei Frau Prof. Dr. Christel C. Müller-Goymann vom Institut für Pharmazeutische Technologie bedanken.